UNIVERSITÀ DEGLI STUDI DI PADOVA

Dipartimento di Fisica e Astronomia "Galileo Galilei"

Master Degree in Astrophysics and Cosmology

Final Dissertation

Numerical construction of precise distribution functions for self-gravitating disks of given surface density profile

Thesis supervisor

Prof. Christos Efthymiopoulos

Candidate

Giulia Manconi

Academic Year 2024/2025

Contents

Abstract

This thesis presents an algorithm to numerically produce distribution function (DF) models which represent exact collisionless equilibria for a thin and truncated self-gravitating disk with a fixed-in-advance surface density profile $\Sigma_D(\rho)$. Firstly a Shu-type DF is modified in such a way that the self-consistency condition leads to an integral equation for an unknown function $S(\rho)$ whose specification completes the determination of the DF. Then a discretized form of the integral equation is solved to obtain numerically $S(\rho)$, the algorithm implemented to derive its expression is described in chapter 2. Families of different DFs yielding the same initial density profile $\Sigma_D(\rho)$ can be produced by choosing different input radial velocity dispersion profiles $\sigma_\rho(\rho)$. The algorithm leads to DFs which, while constrained in principle only to exactly reproduce the imposed surface density profile $\Sigma_D(\rho)$, in practice reproduce also to a good accuracy the imposed velocity dispersion profiles $\sigma_\rho(\rho)$, hence allowing to have control on the kinematic properties (e.g. the Q-profile) of the disk. Several properties of the obtained DFs are discussed and compared to the predictions of epicyclic and post-epicyclic theory for a disk with Schwarzchild's DF. The constancy in time and stability properties of the N-body system whose initial conditions are obtained through the computed DFs are tested via N-body simulations.

Chapter 1

Introduction

1.1 General

Our knowledge of galactic dynamics is largely based on the results obtained through N-body simulations. In this context it is crucial to properly generate the initial conditions, i.e. the particles' initial positions and velocities, which lead to simulations with particular characteristics. The question of the proper generation of initial conditions for N-body simulations is considerably complex, especially when considering multiple galactic components that interact with each other.

When modelling galactic systems it is more convenient to consider the overall motion of the bodies rather than their individual orbits. Therefore, distribution function (DF) models are used to specify the distribution of particles in phase-space, i.e. the space of orbital positions and velocities.

In this thesis, we build a distribution function corresponding to a galactic disk in equilibrium, that exactly reproduces a pre-selected imposed surface density profile. The new model of the DF stems from a model proposed decades ago by Shu (Shu 1969). The algorithm implemented to derive its expression is described in Chapter 2. Chapter 3 presents an example of galactic disk obtained with this distribution function. The galactic system consists in a thin, axisymmetric disk interacting with two spherical components: a dark matter halo and a bulge. Using our computed DF, the initial conditions of the bodies are derived and the stability of the system is tested using N-body simulations.

In the following paragraphs we give some basic definitions and a summary of notions and formulas used in the rest of the thesis.

1.2 Distribution functions

We consider a collisionless stellar system in which the constituent particles (stars or elements of dark matter) move under the influence of the gravitational field generated by a smooth mass distribution. The distribution function (DF) is the number density of stars in phase-space

$$f(\vec{x},\vec{v},t)=\frac{dN}{d^3\vec{x}\,d^3\vec{v}}. \tag{1.1}$$

Assuming all particles identical, the DF can be interpreted through a probabilistic approach: given a region of phase-space $\mathcal{D}$, the integral of f over positions and velocities inside $\mathcal{D}$

$$\mathcal{P}(\mathcal{D})=\int_{\mathcal{D}} f(\vec{x},\vec{v},t)\,d^3\vec{x}\,d^3\vec{v} \tag{1.2}$$

yields the probability $\mathcal{P}(\mathcal{D})$ of having a body at time t with phase-space coordinates inside the chosen region (Binney and Tremaine 2008). In this appoach f is normalized as

$$\int f(\vec{x},\vec{v},t)\,d^3\vec{x}\,d^3\vec{v}=1. \tag{1.3}$$

Once the expression of the distribution function is known we can define the number density of the system at point $\vec{x}$ in configuration space as:

$$n(\vec{x},t) = \int f(\vec{x},\vec{v},t)\, d^3\vec{v}. \tag{1.4}$$

The i-th component of the mean velocity, with $i = 1,2,3$ corresponding to the x, y and z directions in Cartesian coordinates is given by:

$$\overline{v_i}(\vec{x},t) = \frac{1}{n(\vec{x},t)} \int v_i\, f(\vec{x},\vec{v},t)\, d^3\vec{v}. \tag{1.5}$$

While the velocity dispersion in ith direction is given by

$$\sigma_i^2(\vec{x},t) = \frac{1}{n(\vec{x},t)} \int v_i^2\, f(\vec{x},\vec{v},t)\, d^3\vec{v} - \overline{v_i}^2(\vec{x},t). \tag{1.6}$$

1.3 Collisionless Boltzmann equation

For evolving N-body systems, we need to study the space-time evolution of the distribution function. To this end, consider first a fluid flow in ordinary space. In this case, mass conservation is expressed by the continuity equation:

$$\frac{\partial\tilde{\rho}}{\partial t} + \frac{\partial(\tilde{\rho}\dot{\vec{x}})}{\partial\vec{x}} = 0 \tag{1.7}$$

where $\tilde{\rho}(\vec{x},t)$ is the mass density. The analogous expression in phase-space is called the Liouville equation, and it takes the form

$$\frac{\partial f}{\partial t} + \frac{\partial(f\dot{\vec{w}})}{\partial\vec{w}} = 0 \tag{1.8}$$

where f is the phase-space volume density and $\vec{w}$ a set of canonical phase-space coordinates. Writing $\vec{w} = (\vec{q},\vec{p})$ ($\vec{q}$ = canonical positions, $\vec{p}$ = canonical momenta), from equation (1.8) we obtain

$$\begin{aligned} &\frac{\partial f}{\partial t} + \frac{\partial(f\dot{\vec{q}})}{\partial\vec{q}} + \frac{\partial(f\dot{\vec{p}})}{\partial\vec{p}} = 0 \\ &\frac{\partial f}{\partial t} + f\frac{\partial\dot{\vec{q}}}{\partial\vec{q}} + \dot{\vec{q}}\frac{\partial f}{\partial\vec{q}} + f\frac{\partial\dot{\vec{p}}}{\partial\vec{p}} + \dot{\vec{p}}\frac{\partial f}{\partial\vec{p}} = 0. \end{aligned} \tag{1.9}$$

Using Hamilton equations

$$\dot{\vec{q}} = \frac{\partial H}{\partial\vec{p}}, \qquad \dot{\vec{p}} = -\frac{\partial H}{\partial\vec{q}}. \tag{1.10}$$

where $H(\vec{q},\vec{p},t)$ is the Hamiltonian function yielding the motions of the particles under their self-consistent potential, equation (1.9) reads

$$\frac{\partial f}{\partial t} + f\frac{\partial}{\partial\vec{q}}\left(\frac{\partial H}{\partial\vec{p}}\right) + \frac{\partial H}{\partial\vec{p}}\frac{\partial f}{\partial\vec{q}} + f\frac{\partial}{\partial\vec{p}}\left(-\frac{\partial H}{\partial\vec{q}}\right) - \frac{\partial H}{\partial\vec{q}}\frac{\partial f}{\partial\vec{p}} = 0. \tag{1.11}$$

Assuming continuity of the partial derivatives of H, we have $\frac{\partial}{\partial\vec{q}}\left(\frac{\partial H}{\partial\vec{p}}\right) = \frac{\partial}{\partial\vec{p}}\left(\frac{\partial H}{\partial\vec{q}}\right)$, hence

$$\frac{\partial f}{\partial t} + \frac{\partial H}{\partial\vec{p}}\frac{\partial f}{\partial\vec{q}} - \frac{\partial H}{\partial\vec{q}}\frac{\partial f}{\partial\vec{p}} = 0 \tag{1.12}$$

leading to

$$\frac{\partial f}{\partial t} + \dot{\vec{q}}\frac{\partial f}{\partial\vec{q}} + \dot{\vec{p}}\frac{\partial f}{\partial\vec{p}} = 0. \tag{1.13}$$

Equation (1.13) is called the collisionless Boltzmann equation (CBE), and it is the fundamental equation of stellar dynamics.
For Cartesian coordinates $(\vec{q},\vec{p}) = (\vec{x},\vec{v})$ the expression of the Hamiltonian is:

$$H = \frac{1}{2}v^2 + \Phi(\vec{x},t) \tag{1.14}$$

where $\Phi(\vec{x},t)$ is the total potential generated by the particles and by external components of matter (if present). The CBE (equation 1.12) in Cartesian variables takes the form

$$\frac{\partial f}{\partial t}+\vec{v}\frac{\partial f}{\partial \vec{x}}-\frac{\partial \Phi}{\partial \vec{x}}\frac{\partial f}{\partial \vec{v}}=0. \tag{1.15}$$

The potential generated by a set of identical particles can be derived from the distribution function itself as:

$$\Phi(\vec{x},t)=-G\int\frac{dm}{|\vec{x}-\vec{x'}|}\,d^3\vec{x'}=-G\,m\int\frac{d^3\vec{x'}}{|\vec{x}-\vec{x'}|}\int f(\vec{x},\vec{v},t)\,d^3\vec{v} \tag{1.16}$$

where m is the mass of each particle and G is the gravitational constant $4.502\cdot10^{-6}$ kpc km^2 s^{-2} $M_\odot^{-1}$. When this expression is valid the system is said to be self-consistent since the distribution function determines the potential through the integral (1.16) and the potential determines the distribution function through the CBE (equation 1.12).
In cylindrical coordinates $(\vec{q},\vec{p})=(\rho,\varphi,z,p_\rho,p_\varphi,p_z)$ the Hamiltonian is:

$$H=\frac{1}{2}(p_\rho^2+\frac{p_\varphi^2}{\rho^2}+p_z^2)+\Phi(\rho,\varphi,z,t) \tag{1.17}$$

and the CBE takes the form

$$\frac{\partial f}{\partial t}+p_\rho\frac{\partial f}{\partial \rho}+\frac{p_\varphi}{\rho^2}\frac{\partial f}{\partial \varphi}+p_z\frac{\partial f}{\partial z}-\left(\frac{\partial \Phi}{\partial \rho}-\frac{p_\varphi^2}{\rho^3}\right)\frac{\partial f}{\partial p_\rho}-\frac{\partial \Phi}{\partial \varphi}\frac{\partial f}{\partial p_\varphi}-\frac{\partial \Phi}{\partial z}\frac{\partial f}{\partial p_z}=0. \tag{1.18}$$

1.4 Jeans theorem

A collisionless system is said to be in steady-state equilibrium if

$$\frac{\partial f}{\partial t}=0. \tag{1.19}$$

For a steady-state distribution function the collisionless Boltzmann equation takes the form

$$\dot{\vec{q}}\frac{\partial f}{\partial \vec{q}}+\dot{\vec{p}}\frac{\partial f}{\partial \vec{p}}=0. \tag{1.20}$$

We call integrals of motion all the functions of phase-space coordinates that retain constant values along the particle's phase-space trajectory

$$\begin{aligned}\frac{dI[q(\vec{t}),p(\vec{t})]}{dt}&=0\\ \frac{\partial I}{\partial \vec{q}}\dot{\vec{q}}+\frac{\partial I}{\partial \vec{p}}\dot{\vec{p}}&=0.\end{aligned} \tag{1.21}$$

Comparing the latter equation with the steady-state collisionless Boltzmann equation (1.12) we see that f is an integral of motion. This leads to the Jeans theorem, which states that any steady-state solution of the collisionless Boltzmann equation depends on phase-space coordinates only through integrals of motion under the corresponding potential. Conversely, any function of the integrals of motion yields a steady-state solution of the collisionless Boltzmann equation (Binney and Tremaine 2008).

1.5 Jeans equations

In principle the distribution function of a system in steady-state with given density $n(\vec{x})$ can be determined solving directly collisionless Boltzmann equation (1.15) with the potential (1.16). In practice, a direct solution of CBE is hardly tractable. Given a number density profile $n(\vec{x})$, a useful approximation to the DF can be obtained through Jeans equations, which allow to compute different

velocity momenta of the DF.
The first Jeans equation corresponds to the 0^{th} order moment of equation (1.15):

$$\int_{-\infty}^{+\infty} \left(\frac{\partial f}{\partial \vec{x}} \vec{v} - \frac{\partial f}{\partial \vec{v}} \frac{\partial \Phi}{\partial \vec{x}} \right) d^3\vec{v} = 0. \tag{1.22}$$

To solve this integral we separately integrate the addends

$$\int_{-\infty}^{+\infty} \frac{\partial f}{\partial \vec{x}} \vec{v}\, d^3\vec{v} = \frac{\partial}{\partial \vec{x}} \int_{-\infty}^{+\infty} f\, \vec{v}\, d^3\vec{v} = \frac{\partial (n\overline{\vec{v}})}{\partial \vec{x}} \tag{1.23}$$

$$\int_{-\infty}^{+\infty} \frac{\partial f}{\partial \vec{v}} \frac{\partial \Phi}{\partial \vec{x}}\, d^3\vec{v} = \frac{\partial \Phi}{\partial \vec{x}} \int_{-\infty}^{+\infty} \frac{\partial f}{\partial \vec{v}}\, d^3\vec{v} = 0 \tag{1.24}$$

where n and $\overline{\vec{v}}$ are defined in equations (1.4) and (1.5) respectively. The integral equation (1.24) vanishes because we assume that $f \to 0$ for $\vec{v} \to \infty$. This results in the continuity equation

$$\frac{\partial (n\overline{v_x})}{\partial x} + \frac{\partial (n\overline{v_y})}{\partial y} + \frac{\partial (n\overline{v_z})}{\partial z} = 0. \tag{1.25}$$

The second set of Jeans equations is calculated integrating the steady-state CBE multiplied by each one of the velocity components v_j with $j = 1, 2, 3$

$$\int_{-\infty}^{+\infty} \left(\frac{\partial f}{\partial \vec{x}} \vec{v} - \frac{\partial f}{\partial \vec{v}} \frac{\partial \Phi}{\partial \vec{x}} \right) v_j\, d^3\vec{v} = 0. \tag{1.26}$$

Working as before, this results in three different expressions, one for each component

$$\frac{\partial (n\overline{v_x^2})}{\partial x} + \frac{\partial (n\overline{v_x v_y})}{\partial y} + \frac{\partial (n\overline{v_x v_z})}{\partial z} + \frac{\partial \Phi}{\partial x}\, n = 0 \tag{1.27}$$

$$\frac{\partial (n\overline{v_x v_y})}{\partial x} + \frac{\partial (n\overline{v_y^2})}{\partial y} + \frac{\partial (n\overline{v_y v_z})}{\partial z} + \frac{\partial \Phi}{\partial y}\, n = 0 \tag{1.28}$$

$$\frac{\partial (n\overline{v_x v_z})}{\partial x} + \frac{\partial (n\overline{v_y v_z})}{\partial y} + \frac{\partial (n\overline{v_z^2})}{\partial z} + \frac{\partial \Phi}{\partial z}\, n = 0. \tag{1.29}$$

These equations can be rephrased considering the definition of velocity dispersion in the different directions

$$\begin{aligned} \sigma_{ij}^2 &= \frac{1}{n} \int f\, (v_i - \overline{v_i})\, (v_j - \overline{v_j})\, d^3v = \\ &= \frac{1}{n} \int f\, v_i\, v_j\, d^3v - \frac{\overline{v_i}}{n} \int f\, v_j\, d^3v - \frac{\overline{v_j}}{n} \int f\, v_i\, d^3v + \frac{\overline{v_i}\,\overline{v_j}}{n} \int f\, d^3v = \\ &= \overline{v_i v_j} - 2\overline{v_i}\,\overline{v_j} + \overline{v_i}\,\overline{v_j} = \overline{v_i v_j} - \overline{v_i}\,\overline{v_j}. \end{aligned} \tag{1.30}$$

For fixed j, we subtract to (1.29) the null term given by $\overline{v_j}$ multiplied by (1.25). In the x-direction, then, we find

$$\frac{\partial (n\overline{v_x^2})}{\partial x} + \frac{\partial (n\overline{v_x v_y})}{\partial y} + \frac{\partial (n\overline{v_x v_z})}{\partial z} + \frac{\partial \Phi}{\partial x}\, n - \overline{v_x} \left(\frac{\partial (n\overline{v_x})}{\partial x} + \frac{\partial (n\overline{v_y})}{\partial y} + \frac{\partial (n\overline{v_z})}{\partial z} \right) = 0 \tag{1.31}$$

$$\frac{\partial (n(\overline{v_x^2} - \overline{v_x}^2))}{\partial x} + \frac{\partial (n(\overline{v_y v_x} - \overline{v_y}\,\overline{v_x}))}{\partial y} + \frac{\partial (n(\overline{v_z v_x} - \overline{v_x}\,\overline{v_z}))}{\partial z} + \frac{\partial \Phi}{\partial x}\, n + n\overline{v_x} \frac{\partial\, \overline{v_x}}{\partial x} + n\overline{v_y} \frac{\partial\, \overline{v_x}}{\partial y} + n\overline{v_z} \frac{\partial\, \overline{v_x}}{\partial z} = 0. \tag{1.32}$$

Analogous results can be derived for the other directions.
Note that these terms can be interpreted as the different forces acting in the system, respectively they stand for: pressure, gravitation and viscosity. Combining this result with the definition of dispersion given by (1.30) we obtain

$$\frac{\partial (n\sigma_{xx}^2)}{\partial x} + \frac{\partial (n\sigma_{xy}^2)}{\partial y} + \frac{\partial (n\sigma_{xz}^2)}{\partial z} + \frac{\partial \Phi}{\partial x}\, n + n\overline{v_x} \frac{\partial \overline{v_x}}{\partial x} + n\overline{v_y} \frac{\partial \overline{v_x}}{\partial y} + n\overline{v_z} \frac{\partial \overline{v_x}}{\partial z} = 0. \tag{1.33}$$

The above system of four Jeans equations involves nine unknown functions($\overline{v_i}$, σ_{ij}), hence a unique solution of the system cannot be calculated. We could try to go on with higher order momenta of the collisionless Boltzmann equation in order to have more equations for the system, but this leads to more functions that are unknown, hence the problem persists. A more suitable approach is to make some assumptions and give as inputs some of these unknown functions. For example, we may assume an isotropic velocity distribution for which $\sigma_{xx} = \sigma_{yy} = \sigma_{zz}$ and $\sigma_{xy} = \sigma_{xz} = \sigma_{yz} = 0$.

1.6 Constants of motion

According to Jeans theorem, for a system in steady-state equilibrium the solutions of the collisionless Boltzmann equation depend on the integrals of motion $I(\vec{q}, \vec{p})$, i.e. on quantities constant along the trajectory of each body of the system.
In the present thesis we are particularly interested in axisymmetric systems such as galactic disks. In such systems there are two integrals of motion: the specific energy (ε) and the angular momentum along the symmetry axis, that can be chosen to be the z axis (l_z). Therefore the DF in general depends on these two integrals: $f(\varepsilon, l_z)$.
The constancy of the energy integral follows from

$$\dot{\varepsilon} = \frac{dH}{dt} = \frac{\partial H}{\partial \vec{q}}\,\dot{\vec{q}} + \frac{\partial H}{\partial \vec{p}}\,\dot{\vec{p}} = \frac{\partial H}{\partial \vec{q}}\,\frac{\partial H}{\partial \vec{p}} - \frac{\partial H}{\partial \vec{p}}\,\frac{\partial H}{\partial \vec{q}} = 0. \tag{1.34}$$

The constancy of the angular momentum integral follows from the definition of the canonical momentum $p_\varphi = \rho^2\dot{\varphi} = l_z$. Since the system is axisymmetric (no dependence on φ), we have

$$\dot{p}_\varphi = -\frac{\partial H}{\partial \varphi} = 0. \tag{1.35}$$

Besides, if the system is spherically symmetric, the modulus of the agular momentum is an additional integral of motion.

1.7 Asymmetric drift

The asymmetric drift is a phenomenon observed in disk galaxies, according to which stars move with mean rotational speed smaller than the local value of the circular velocity $v_c = (\rho\Phi'(\rho))^{1/2}$ corresponding to a given distance ρ from the center of the disk.

The asymmetric dirft is a direct consequence of Jeans equations. Adopting cilindrical coordinates, the CBE becomes

$$\begin{aligned}
&\dot{\rho}\,\frac{\partial f}{\partial \rho} + \dot{\varphi}\,\frac{\partial f}{\partial \varphi} + \dot{z}\,\frac{\partial f}{\partial z} + \dot{p_\rho}\,\frac{\partial f}{\partial p_\rho} + \dot{p_\varphi}\,\frac{\partial f}{p_\varphi} + \dot{p_z}\,\frac{\partial f}{\partial p_z} = 0 \\
&\dot{\rho}\,\frac{\partial f}{\partial \rho} + \dot{\varphi}\,\frac{\partial f}{\partial \varphi} + \dot{z}\,\frac{\partial f}{\partial z} - \left(\frac{\partial \Phi}{\partial \rho} - \frac{p_\varphi^2}{\rho^3}\right)\frac{\partial f}{\partial p_\rho} - \frac{\partial \Phi}{\partial \varphi}\,\frac{\partial f}{p_\varphi} - \frac{\partial \Phi}{\partial z}\,\frac{\partial f}{\partial p_z} = 0.
\end{aligned} \tag{1.36}$$

Multiplying this equation by p_ρ and integrating it over the momentum space we obtain the second Jeans equation in cylindrical coordinates

$$\frac{\partial(n\overline{v_\rho^2})}{\partial \rho} + \frac{\partial(n\overline{v_\rho v_z})}{\partial z} + n\left(\frac{\partial \Phi}{\partial \rho} + \frac{\partial \Phi}{\partial z} - \frac{\overline{v_\varphi^2}}{\rho}\right) = 0. \tag{1.37}$$

Given the definitions of the velocity dispersion $\sigma_\varphi^2 = \overline{v_\varphi^2} - \overline{v_\varphi}^2$ and circular velocity $v_c^2 = \rho\,\frac{\partial \Phi}{\partial \rho}$ and assuming $\overline{v_\rho} = 0$ the second Jeans equation can be rephrased as

$$\overline{v_\varphi}^2 - v_c^2 = \frac{\rho}{n}\frac{\partial(n\sigma_\rho^2)}{\partial \rho} + \sigma_\rho^2 - \sigma_\varphi^2 + \rho\frac{\partial \Phi}{\partial z} + \frac{\rho}{n}\frac{\partial(n\sigma_{\rho z}^2)}{\partial z}. \tag{1.38}$$

Equation (1.38) shows that the mean azimuthal velocity of the stellar population is generally lower than the local circular velocity. Altogether, the equation quantifies how the pressure support provided by stellar velocity dispersions reduces the mean streaming velocity compared to the circular velocity.

1.8 Distribution functions for galactic disks

To model galactic disks we determine the DF taking advantage of the fact that the disk can be approximated as axisymmetric. The axis of symmetry is chosen to correspond to the z axis.
The expressions of the distribution function known from literature can be understood starting with the easier case of a cold rotating disk with zero velocity dispersion. Assuming the potential to be symmetric with respect to the equatorial plane, all particles rotate with the circular velocity and the DF can be written as (Bovy 2026)

$$f(\varepsilon, l_z) = F(l_z)\,\delta(\varepsilon - \varepsilon_c(l_z)) \tag{1.39}$$

where $\varepsilon_c(l_z)$ is the energy of the circular orbit with angular momentum l_z. In a more realistic situation where we have a warm rotating disk, the bodies will not be strictly in circular motion, hence we replace the delta function with a function depending on the radial velocity dispersion profile. The choice of different expressions for this function leads to different models of the DF that determine the properties of the galactic disk. In this section we focus on flat disks, neglecting the disk's thickness as well as the particle's motions in direction vertical to the disk plane. In section 1.9 we explain how the DF can be modified to generate thick disks with bodies moving along the z axis.

Shu model of the Distribution Function

Shu proposed a phenomenological model for the distribution function of warm galactic disks (Shu 1969):

$$f_{Shu}(\varepsilon(\rho, v_\rho, v_\varphi), l_z) = \frac{2\Omega(\rho_c)}{\kappa(\rho_c)} \frac{\Sigma(\rho_c)}{2\pi\sigma_\rho^2(\rho_c)} e^{-\frac{\varepsilon - \varepsilon_c(\rho_c)}{\sigma_\rho^2(\rho_c)}}. \tag{1.40}$$

This DF is suitable for flat and rapidly rotating stellar disks with axisymmetric potentials and depends on the two integrals of motion ε and l_z. Specifically the dependence on l_z is expressed through the variable ρ_c that is the radius of the circular orbit with angular momentum l_z. The argument of the exponential

$$\varepsilon - \varepsilon_c \sim \frac{1}{2}v_\rho^2 + \frac{1}{2}v_\varphi^2 + \Phi(\rho) - \frac{1}{2}v_c^2 - \Phi(\rho_c) \tag{1.41}$$

represents the energy difference from the circular orbit for a ring of stars with angular momentum l_z rotating near the circular radius with radial velicity dispersion $\sigma_\rho(\rho_c)$. Two input functions are needed to define this DF model: the surface density profile $\Sigma(\rho)$ and the radial velocity dispersion $\sigma_\rho(\rho)$. Notice that integrating this distribution function over the momentum space we obtain a surface density profile instead of a number density. This is coherent with the definition of the distribution function given in 1.1 if stars have all the same mass, hence surface density is proportional to number density. However, the integrals (1.4, 1.6) do not reproduce exactly the imposed profiles of $\Sigma(\rho)$ and $\sigma_\rho(\rho)$, hence perfect self-consistency is not garantueed (see Sharma and Bland-Hawthorn 2013).

Schwarzschild model of the distribution function

The Schwarzschild's model of the DF (see Binney and Tremaine 2008) starts from the assumption that the stars move along nearly circular orbits, therefore the argument of the exponential in (1.40) can be simplified using epicyclic theory as

$$\varepsilon - \varepsilon_c(\rho_c) \simeq \frac{1}{2}v_\rho^2 + \frac{1}{2}\kappa^2(\rho_c)(\rho - \rho_c)^2 \simeq \frac{1}{2}v_\rho^2 + \frac{1}{2}\frac{4\Omega^2(\rho_c)}{k^2(\rho_c)}(v_\varphi - v_c(\rho))^2. \tag{1.42}$$

The resulting expression of the DF

$$f_{Schwarzschild}(\varepsilon(\rho, v_\rho, v_\varphi), l_z) = \frac{2\Omega(\rho_c)}{\kappa(\rho_c)} \frac{\Sigma(\rho_c)}{2\pi\sigma_\rho^2(\rho_c)} e^{-\frac{v_\rho^2}{2\sigma_\rho^2(\rho_c)} - \frac{4\Omega^2(\rho_c)}{k^2(\rho_c)}\frac{(v_\varphi - v_c)^2}{2\sigma_\rho^2(\rho_c)}} = \frac{\Sigma(\rho_c)}{2\pi\sigma_\rho(\rho_c)\sigma_\varphi(\rho_c)} e^{-\frac{v_\rho^2}{2\sigma_\rho^2(\rho_c)} - \frac{(v_\varphi - v_c)^2}{2\sigma_\varphi^2(\rho_c)}} \tag{1.43}$$

describes a bivariate Gaussian velocity distribution consistent with the epicyclic approximation, where the distribution of the radial velocities v_ρ is centred at zero with dispersion σ_ρ, and the distribution of the azimuthal velocities v_φ is centered at the local circular speed v_c with dispersion

$$\sigma_\varphi = \frac{\kappa\,\sigma_\rho}{2\Omega}. \tag{1.44}$$

Hernquist model of the distribution function

The Hernquist model for the distribution function (see Hernquist 1990)

$$f_{Hernquist} = \frac{1}{2\pi\sigma_\rho(\rho)\sigma_\varphi(\rho)} e^{-\frac{v_\rho^2}{2\sigma_\rho^2(\rho)} - \frac{(v_\varphi - \overline{v_\varphi})^2}{2\sigma_\varphi^2(\rho_c)}} \tag{1.45}$$

yields a bivariate Gaussian velocity distribution where the distribution of the radial velocities component v_ρ is centered at zero with radial dispersion σ_ρ, and the distribution of the azimuthal velocities v_φ is centered at the mean angular velocity $\overline{v_\varphi}$ derived from the asymmetric drift equation

$$\overline{v_\varphi}(\rho) = \sqrt{\frac{\rho}{\Sigma}\frac{\partial(\Sigma\sigma_\rho^2)}{\partial\rho} + \rho\frac{\partial\Phi}{\partial\rho} + \sigma_\rho^2 - \sigma_\varphi^2}. \tag{1.46}$$

1.9 Thickness of the disk

Up to this point we considered a completely flat disk with zero velocity component along the z axis. However in realistic galactic models we need to take into account the thickness of the disk. This can be achieved considering a third integral of motion, besides ε and l_z.
If the integrals of motion were only ε and l_z the velocity dispersion along the z-direction would be identical to the radial dispersion because the energy difference of the above models would be

$$\varepsilon - \varepsilon_c \sim \frac{1}{2}v_\rho^2 + \frac{1}{2}v_\varphi^2 + \frac{1}{2}v_z^2 + \Phi(\rho, z) - \frac{1}{2}v_c^2 - \Phi(\rho_c) \tag{1.47}$$

where the vertical velocity profile is a Gaussian distribution with σ_ρ dispersion. Observations of the Sun's neighbor show that $\sigma_z \sim \sigma_\rho/2$ (Hänninen and Flynn 2004) therefore we need to introduce a third integral (I_3) of motion for the DF in order to reproduce what happens in real scenarios.
Deriving analytical expressions of $f(\varepsilon, l_z, I_3)$ is challenging. A useful approximation is obtained as follows (see Contopoulos 1960): since the disk is thin and symmetric with respect to the equatiorial plane we can use the Taylor expansion of the potential to distinguish between the planar (H_{plane}) and vertical (H_z) contributions

$$H = \frac{1}{2}v_\rho^2 + \frac{1}{2}v_\varphi^2 + \frac{1}{2}v_z^2 + \Phi(\rho, z) \simeq \frac{1}{2}v_\rho^2 + \frac{1}{2}v_\varphi^2 + \Phi(\rho, z=0) + \frac{1}{2}v_z^2 + \frac{1}{2}\left.\frac{\partial^2\Phi}{\partial z^2}\right|_{z=0} z^2 = H_{plane} + H_z. \tag{1.48}$$

The Hamiltonian is time independent, hence we can consider as lowest order of approximation of the third integral of motion the constant value of vertical energy

$$\varepsilon_z = \frac{1}{2}v_z^2 + \frac{1}{2}\left.\frac{\partial^2\Phi}{\partial z^2}\right|_{z=0} z^2 = \frac{1}{2}v_z^2 + \frac{1}{2}\kappa_z^2(\rho)z^2. \tag{1.49}$$

Using (1.49), the distribution function of bodies in the vertical direction according to Jeans theorem is

$$f_z(\varepsilon_z) = \frac{1}{\sqrt{2\pi}\sigma_z} e^{-\frac{\varepsilon_z}{2\sigma_z^2}} = \frac{1}{\sqrt{2\pi}\sigma_z} e^{-\frac{k_z^2}{2\sigma_z^2}\left(\frac{v_z^2}{k_z^2} + z^2\right)}. \tag{1.50}$$

Multipling $f_z(\varepsilon_z)$ with the DF of the completely flat disk we can have an approximate 3D model for the full DF.

1.10 Spherical components

Considering components such as dark matter halos or bulges we are dealing with systems in spherical symmetry. An additional assumption that can be adopted is self-consistency, in this case the density determines the potential through Poisson's equation

$$\nabla^2\Phi = 4\pi G\tilde{\rho}(\vec{x}) \tag{1.51}$$

where $\tilde{\rho}$ is the mass density and Φ is the total potential. In the following computations we introduce two new variables in order to make the derivations easier: the namely relative potentiial $\Psi = -\Phi + \Phi_C$ and the relative energy $\epsilon = -\varepsilon + \Phi_C = \Psi - \frac{1}{2}v^2$ where Φ_C is a constant such that (1.52) is valid.

$$\begin{cases} f > 0 & \text{if } \epsilon > 0 \\ \\ f = 0 & \text{if } \epsilon \leq 0 \end{cases} \tag{1.52}$$

Substituting the new variables in equation (1.51) Poisson's equation becomes

$$\nabla^2\Psi = -4\pi G\rho(\vec{x}). \tag{1.53}$$

Under the assumption that the system is isotropic, and changing the variable of integration with the substitution $v = \sqrt{2(\Psi(\rho) - \epsilon)}$, the mass density can be written as

$$\tilde{\rho}(\rho) = 4\pi \int dv\, v^2 f(\Psi - \frac{1}{2}v^2) = 4\pi \int_0^{\Psi(\rho)} d\epsilon\, f(\epsilon)\sqrt{2(\Psi(\rho) - \epsilon)}. \tag{1.54}$$

This equation can be differentiated on both sides to obtain the Abel integral equation

$$\frac{1}{4\pi\sqrt{2}}\frac{d\rho}{d\Psi} = \int_0^{\Psi} \frac{f(\epsilon)}{2\sqrt{(\Psi - \epsilon)}}\, d\epsilon \tag{1.55}$$

whose solution is Eddington's formula

$$f(\epsilon) = \frac{1}{\sqrt{8}\pi^2}\frac{\mathrm{d}}{\mathrm{d}\epsilon}\int_0^{\epsilon}\frac{\mathrm{d}\tilde{\rho}}{\mathrm{d}\Psi}\frac{d\Psi}{\sqrt{\epsilon - \Psi}} = \frac{1}{\sqrt{8}\pi^2}\frac{\mathrm{d}}{\mathrm{d}\varepsilon}\int_{\varepsilon}^{\Phi(\rho_{max})}\frac{\mathrm{d}\tilde{\rho}}{\mathrm{d}\Phi}\frac{d\Phi}{\sqrt{\Phi - \varepsilon}}. \tag{1.56}$$

Therefore, once the density and potential profiles are chosen for a spherically isotropic component of the system, we can calculate the integral (1.56) and derive the corresponding isotropic distribution function $f(\varepsilon)$.

1.11 Domain of the DF

In this section we derive the formulas which allow to explicitly compute the domain $\mathcal{D}$ of the distribution function used in integrals of equations (1.4), (1.5), (1.6), in case of a flat truncated disk of finite extent ($\rho = \rho_{max}$).

The computation of $\mathcal{D}$ proceeds as follows, each orbiting body is characterized by two integrals of motion that are constant along its trajectory: the specific energy

$$\varepsilon = \frac{1}{2}(v_\rho^2 + v_\varphi^2) + \Phi_0(\rho) \tag{1.57}$$

and the angular momentum

$$p_\varphi = \rho v_\varphi. \tag{1.58}$$

The total potential, Φ_0, results from the sum of the contributions of all galactic components, in our case, halo, bulge, and disk

$$\Phi_0(\rho) = \Phi_D(\rho) + \Phi_h(\rho) + \Phi_b(\rho). \tag{1.59}$$

For circular orbits, the angular momentum is given by

$$p_c(\rho_c) = \sqrt{\rho_c^3 \frac{d\Phi_0}{d\rho}\Big|_{\rho_c}}. \tag{1.60}$$

Equation (1.60) can be inverted to determine the radius of a circular orbit corresponding to a given angular momentum, $\rho_c(p_c)$.

Consider now the particles in epicyclic orbits around the circular orbit of radius $\rho = \rho_c$. The angular and epicyclic frequencies are

$$\Omega(\rho_c) = \sqrt{\frac{1}{\rho_c}\frac{d\Phi_0}{d\rho}\Big|_{\rho=\rho_c}} \tag{1.61}$$

$$\kappa(\rho_c) = \sqrt{\frac{3}{\rho_c}\frac{d\Phi_0}{d\rho}\Big|_{\rho=\rho_c} + \frac{d^2\Phi_0}{d\rho^2}\Big|_{\rho=\rho_c}}. \tag{1.62}$$

If we consider a body orbiting with angular momentum p_φ and apocenter ρ_{max} its constant energy is

$$\varepsilon = \varepsilon_a(p_\varphi, \rho_a) = \frac{p_\varphi}{2\rho_a^2} + \Phi_0(\rho_a) \tag{1.63}$$

where p_φ can be expressed by equating the energy of the body at its pericetner and apocenter

$$p_\varphi(\rho_p, \rho_a) = \sqrt{2\frac{\Phi(\rho_a) - \Phi(\rho_p)}{1/\rho_p^2 - 1/\rho_a^2}}. \tag{1.64}$$

When the disk is truncated at the radius ρ_{max}, only bounded orbits within that radius are allowed, therefore the energy of each body has to be lower than its energy when the apocenter of the orbit is $\rho_{max} : \varepsilon < \varepsilon_a(p_\varphi, \rho_{max})$. Furthermore, the angular momentum of each star can be chosen to be positive in order to have a unique sense of rotation (that is the sense of rotation of the galaxy). The angular momentum has to be lower than the one of orbits with ρ_{max} as apocenter, this leads to the further condition: $0 < p_\varphi < p_\varphi(\rho, \rho_{max})$.

Using the above inequations we can express the domain of the distribution function for the truncated disk as

$$\begin{aligned} \mathcal{D}_v \quad = \Bigg\{ \quad & 0 < v_\varphi \leq \frac{p_\varphi(\rho, \rho_{max})}{\rho}, \\ & -\sqrt{2(\varepsilon_a(p_\varphi = \rho v_\varphi; \rho_{max}) - v_\varphi^2 - \Phi(\rho))} \leq v_\rho \leq \sqrt{2(\varepsilon_a(p_\varphi = \rho v_\varphi; \rho_{max}) - v_\varphi^2 - \Phi(\rho))} \Bigg\}. \end{aligned} \tag{1.65}$$

1.12 Inversion methods

Inversion methods are adopted to obtain models of distribution functions consistent with a given disk surface density profile $\Sigma_D(\rho)$. This technique consists in inverting the integral equation

$$\Sigma_D(\rho) = \iint_{\mathcal{D}_v} f(\rho, v_\rho, v_\varphi)\, dv_\rho\, dv_\varphi \tag{1.66}$$

and obtaining the corresponding expression of the distribution function. Several inversion strategies have been developed, in the following paragraphs we outline the three approaches adopted to solve this problem: exact inversions based on Abel transforms, iterative methods and approximate *ansatz*-based methods.

Exact inversion methods

The most rigorous approach is to perform an exact inversion of equation (1.66), thereby recovering a DF that exactly reproduces the input $\Sigma(\rho)$ (these procedures were performed in Kuijken and Merrifield 1993, Pichon and Thiebaut 1998 and Pichon and Lynden-Bell 1996). The procedure begins by integrating equation (1.66) over the velocity v_φ, yielding

$$F(\rho,\ v_\varphi) = \Sigma(\rho)\tilde{F}(\rho, v_\varphi) = \int_{\mathcal{D}_v} f(\rho, v_\rho, v_\varphi)\, dv_\rho. \tag{1.67}$$

Introducing a change of variables $v_\rho \ \rightarrow\ \frac{1}{2}\left(v_\rho^2 + v_\varphi^2\right) + \Phi(\rho)$, (1.67) is transformed into an Abel-type integral equation.

Abel integrals admit formal inversion either analytically or numerically. In practice, the inversion can be carried out using tabulated Abel kernels, numerical differentiation, or fitting procedures. The main advantage of this approach is that it guarantees dynamical self-consistency: the DF exactly matches the imposed $\Sigma_D(\rho)$ in the specified potential. However, there are notable drawbacks: (i) the radial velocity dispersion profile $\sigma_\rho(\rho)$ is not a free input but is determined by the inversion; (ii) Abel inversion operators are ill-conditioned, which may lead to numerical instabilities and amplification of noise in the recovered DF.

Iterative methods

An alternative method is to determine the DF through an iterative adjustment procedure (Bienayme and Sechaud 1997 and Dehnen 1999). Here, one starts by prescribing the desired $\Sigma(\rho)$ and an initial guess for the DF. The DF is then repeatedly modified until the integral equation (1.66) is satisfied to a chosen tolerance. This is the method adopted in this thesis, starting from a Shu DF as the initial guess we replace $\Sigma(\rho)$ with an auxiliary function $S(\rho)$ that is adjusted during the iteration. The goal is to construct $S(\rho)$ so that the integration of the DF exactly reproduces the target $\Sigma(\rho)$. We implement this procedure using a Generalized Minimal Residual (GMRES) iterative solver, which is well-suited for solving the linearized form of the problem. The iterative approach offers direct control over the velocity dispersion profile and allows the incorporation of additional constraints (e.g. kinematical data).

Approximate ansatz for the DF

The simplest approach is to assume a parametric form for the DF, with the velocity dispersion profiles specified as inputs. This *ansatz*-based method is widely used in modelling stellar disks, where analytical convenience and qualitative agreement with observations are prioritised over exact self-consistency. A common choice is to adopt Gaussian velocity distributions in the radial and azimuthal directions (as for example in case of the Hernquist model of the distribution function), with an asymmetric drift correction for the mean azimuthal velocity, and a vertical profile consistent with the observed scale height. While this method is straightforward to implement and computationally efficient, it inevitably introduces approximations. Since the DF is imposed rather than derived, the resulting system is not guaranteed to satisfy equation (1.66) exactly, and numerical N-body realizations of such a DF typically require a relaxation phase to reach equilibrium. Nevertheless, the flexibility of the *ansatz* approach makes it a valuable tool for exploring large parameter spaces and for generating initial conditions in dynamical simulations.

1.13 Initial conditions for N-body simulations

Once the expression of the distribution function is known the initial conditions (particles' positions and velocities) can be computed for each of the components of the simulated system (disk, halo and bulge). To this end, the rejection algorithm can be used to generate a number of particles with the required probabilty distribution in ordinary space as well as in the space of velocities. The theoretical interpretation of this method for the different systems is explained in the following paragraphs.

Spherical components

Starting from the definition of the distribution function (1.1) the number of bodies contained within an infinitesimal element of phase-space volume is given by

$$\Delta N(r,v) = f(r,v)\Delta^3 x \Delta^3 v = 16\pi^2 f(r,v) r^2 v^2 \Delta r \Delta v \tag{1.68}$$

where $r = |\vec{x}|$, $v = |\vec{v}|$. Hence the probability density in the reduced (ρ, v) space is

$$F(r,v) = \frac{\Delta N}{\Delta r \Delta v} = 16\pi^2 r^2 v^2 f(r,v). \tag{1.69}$$

This expression of the distribution function weighted by the phase-space volume element is employed in the rejection algorithm to distribute the bodies. Specifically, generating triplets of random values for $(r, v, \hat{F})$ within the allowed domain the algorithm retains only those such that $\hat{F} < F(r,v)$. This method works because $F(r,v)$ quantifies the relative likelihood of finding a body at a given radius r with a velocity magnitude v, hence the higher is this number, the more bodies we will have.

Galactic disk

The initial conditions for the bodies of the galactic disk are generated following a procedure as above for the spherical components. The number of bodies in each phase-space volume element is now given by

$$\Delta N(r, v_\rho, v_\varphi) = f(r, v_\rho, v_\varphi)\Delta^2 x \Delta^2 v = 2\pi r f(\rho, v_\rho, v_\varphi)\Delta r \Delta v_\rho \Delta v_\varphi \tag{1.70}$$

and this time the probabilty density is reduced in the ρ, v_ρ, v_φ space as

$$F(r, v_\rho, v_\varphi) = \frac{\Delta N}{\Delta r \Delta v_\rho \Delta v_\varphi} = 2\pi r f(r,v). \tag{1.71}$$

In the rejection algorithm we consider quadruplets of $(r, v_\rho, v_\varphi, \hat{F})$ and consider as initial conditions only those such that $\hat{F} < F(r, v_\rho, v_\varphi)$ as we did for the spherical component.

Chapter 2

New model for the DF

2.1 Model

In the present chapter, we propose a new model of steady-state distribution function that exactly reproduces the imposed profile of surface density $\Sigma_D(\rho)$ for a galactic disk. The method adopted to obtain this new expression of the DF is based on an iterative method.
We consider the Shu model of the distribution function (1.40). In order to garantuee self-consistency, we substitute $\Sigma(\rho)$ in Shu's formula with an unknown function $S(\rho)$

$$f(\varepsilon(\rho, v_\rho, v_\varphi), p_\varphi(\rho, v_\varphi)) = \begin{cases} \frac{S(\rho_c(p_\varphi))}{2\pi\sigma_\rho(\rho_c(p_\varphi))\sigma_\varphi(\rho_c(p_\varphi))} e^{-\frac{\varepsilon-\varepsilon_c(p_\varphi)}{\sigma_\rho^2(\rho_c(p_\varphi))}} & \text{if } p_\varphi > 0 \\ & \text{and } \varepsilon < \varepsilon_a(p_\varphi; \rho_{max}) \\ 0 & \text{otherwise} \end{cases} \tag{2.1}$$

where:

- $S(\rho_c)$ is an unknown function computed using numerical methods, which serves to exactly reproduce Σ_D when solving the integral equation (1.66).
- $\rho_c(p_\varphi)$ is the radius of the circular orbit with angualr velocity p_φ that is obtained by inverting (1.60).
- $\sigma_\rho(\rho_c)$ and $\sigma_\varphi(\rho_c)$ are pre-selected input functions for the dispersion of radial and angular velocities in the disk.

The limits on angular momentum and energy are imposed by the requirement that all the disk bodies move in the same direction (positive angular momentum) and along a bounded orbit within the maximum radius of the disk (ρ_{max}) (see Section 1.11). The response radial and azimuthal velocity dispersion profiles only approximately coincide with the input functions $\sigma_\rho(\rho), \sigma_\varphi(\rho)$, while as mentioned before, the response surface density matches the pre-selected imposed model $\Sigma_D(\rho)$ exactly.

2.2 Building S(ρ)

To obtain the expression of S(ρ) we reduce the self-consistency integral (1.66) to a linear system that can be solved with iterative methods.
Starting from the distribution function f (2.1) and considering the domain $\mathcal{D}_v$ defined in Section 1.11, the self-consistency equation (1.66) takes the form:

$$\Sigma_D(\rho) = \iint_{\mathcal{D}_v} dv_\rho dv_\varphi \frac{S(\rho_c(p_\varphi))}{2\pi\sigma_\rho(\rho_c(p_\varphi))\sigma_\varphi(\rho_c(p_\varphi))} \exp\left(-\frac{(\varepsilon - \varepsilon_c(p_\varphi))}{\sigma_\rho^2(\rho_c(p_\varphi))}\right). \tag{2.2}$$

Since most of the functions appearing in the integrand of (2.2) depend on ρ_c, it is convenient to change the variables of integration in order to simplify the calculations.
First we introduce the change of variable $v_\varphi \to p_\varphi = \rho v_\varphi$. Then, the integral and domain become:

$$\rho\Sigma_D(\rho) = \iint_{\mathcal{D}_p} dv_\rho dp_\varphi \frac{S(\rho_c(p_\varphi))}{2\pi\sigma_\rho(\rho_c(p_\varphi))\sigma_\varphi(\rho_c(p_\varphi))} \exp\left(-\frac{(\varepsilon - \varepsilon_c(p_\varphi))}{\sigma_\rho^2(\rho_c(p_\varphi))}\right) \tag{2.3}$$

$$\begin{aligned}\mathcal{D}_p \quad = \Bigg\{ \quad & 0 < p_\varphi \le p_\varphi(\rho, \rho_{max}), \\ & -\sqrt{2(\mathcal{E}_a(p_\varphi;\rho_{max}) - \frac{p_\varphi^2}{2\rho^2} - \Phi(\rho))} \le v_\rho \le \sqrt{2(\mathcal{E}_a(p_\varphi;\rho_{max}) - \frac{p_\varphi^2}{2\rho^2} - \Phi(\rho))} \Bigg\}.\end{aligned} \tag{2.4}$$

Next, we change the integration variable from p_φ to ρ_c. To this end we consider the inversion of equation (1.60) yielding

$$dp_\varphi = \frac{1}{2\sqrt{\rho_c^3 \frac{d\Phi_0}{d\rho}\Big|_{\rho_c}}} \left(3\rho_c^2 \frac{d\Phi_0}{d\rho}\Big|_{\rho_c} + \rho_c^3 \frac{d^2\Phi_0}{d\rho^2}\Big|_{\rho_c}\right) d\rho_c = \frac{\rho_c \kappa^2(\rho_c)}{2\Omega(\rho_c)} d\rho_c. \tag{2.5}$$

Using (2.5), the integral (2.3) transforms to:

$$\rho\Sigma_D(\rho) = \iint_{\mathcal{D}_c} d\rho_c dv_\rho \left(\frac{\kappa(\rho_c)\rho_c S(\rho_c)}{2\pi\sigma_\rho^2(\rho_c)}\right) \exp\left(-\frac{(\mathcal{E} - \mathcal{E}_c(\rho_c))}{\sigma_\rho^2(\rho_c)}\right) \tag{2.6}$$

with the domain

$$\begin{aligned}\mathcal{D}_c(\rho) \quad = \Bigg\{ \quad & 0 < \rho_c \le \rho_{c,max}(\rho, \rho_{max}), \\ & -\sqrt{2\left(\mathcal{E}_a(p_\varphi(\rho_c);\rho_{max}) - \frac{p_\varphi^2(\rho_c)}{2\rho^2} - \Phi(\rho)\right)} \le v_\rho \le \sqrt{2\left(\mathcal{E}_a(p_\varphi(\rho_c);\rho_{max}) - \frac{p_\varphi^2(\rho_c)}{2\rho^2} - \Phi(\rho)\right)} \Bigg\}.\end{aligned} \tag{2.7}$$

Now, recalling that $p_\varphi = v_c\rho_c = \Omega(\rho_c)\rho_c^2$, the energy difference in the exponential becomes

$$\varepsilon - \varepsilon_c = \frac{1}{2}v_\rho^2 + \frac{1}{2}\frac{\rho_c^4\Omega^2(\rho_c)}{\rho^2} + \Phi(\rho) - \frac{1}{2}\Omega^2(\rho_c)\rho_c^2 - \Phi(\rho_c). \tag{2.8}$$

Hence, the integral (2.6) can be rephrased as:

$$\rho\Sigma_D(\rho) = \iint_{\mathcal{D}_c} d\rho_c dv_\rho \left(\frac{\kappa(\rho_c)\rho_c S(\rho_c)}{2\pi\sigma_\rho^2(\rho_c)}\right) \exp\left(-\frac{\left(\frac{1}{2}v_\rho^2 + \frac{1}{2}\frac{\rho_c^4\Omega^2(\rho_c)}{\rho^2} + \Phi(\rho) - \frac{1}{2}\Omega^2(\rho_c)\rho_c^2 - \Phi(\rho_c)\right)}{\sigma_\rho^2(\rho_c)}\right). \tag{2.9}$$

Now we integrate over v_ρ: the only term involved in this calculation is $\frac{1}{\sqrt{2\pi}\sigma_\rho} e^{-\frac{v_\rho^2}{2\sigma_\rho^2}}$. Knowing that the solution of the integral of a Gaussian profile of this type is the error function

$$\mathrm{erf}(a,b) = \frac{1}{\sqrt{2\pi}b}\int_{-a}^{a} e^{-x^2/(2b^2)} dx \tag{2.10}$$

we get the final expression of the integral

$$\rho\Sigma_D(\rho) = \int_0^{\rho_{c,max}(\rho,\rho_{max})} d\rho_c A(\rho,\rho_c) X(\rho_c) \tag{2.11}$$

where

$$A(\rho,\rho_c) = \left(\frac{\kappa(\rho_c)}{\sqrt{2\pi}\sigma_\rho(\rho_c)}\right)\mathrm{erf}\left(\sqrt{2\left(\mathcal{E}_a(p_\varphi(\rho_c);\rho_{max})-\frac{p_\varphi^2(\rho_c)}{2\rho^2}-\Phi(\rho)\right)},\sigma_\rho(\rho_c)\right) \quad (2.12)$$
$$\times \exp\left(-\frac{\left(\frac{1}{2}\left(\frac{\rho_c^4\Omega^2(\rho_c)}{\rho^2}\right)+\Phi(\rho)-\Phi(\rho_c)-\frac{1}{2}\Omega^2(\rho_c)\rho_c^2\right)}{\sigma_\rho^2(\rho_c)}\right)$$

$$X(\rho_c)=\rho_c S(\rho_c). \quad (2.13)$$

A suitable way to solve the integral (2.11) is through discretization.

Consider the two-dimensional grid

$$G_{\rho,\rho_c}=\{\rho_i=i\delta\rho,\quad \rho_{c,j}=j\delta\rho,\quad i=1,\dots,N-1,\ j=1,\dots,N-1,\quad \delta\rho=\rho_{max}/N\}\,. \quad (2.14)$$

as well as the matrix $\mathcal{A}$ with elements

$$a_{ij}=\begin{cases}\delta\rho A(\rho_i,\rho_{c,j}) & \text{if } \rho_{c,j}\le\rho_{c,max}(\rho_i,\rho_{max})\\ 0 & \text{otherwise,}\end{cases} \quad (2.15)$$

$\mathcal{B}=(\rho_1\Sigma_D(\rho_1),...,\rho_{max},\Sigma_D(\rho_{max}))^T$, $\mathcal{X}=(X_1,\dots,X_N)^T$, with $X_j=\rho_{c,j}S(\rho_{c,j})$. A discretized form of the equation (2.11) then follows by replacing the integral by the sum:

$$\rho_i\Sigma_D(\rho_i)\simeq\delta\rho\sum_{j=1}^{N}A(\rho_i,\rho_{c,j})X(\rho_{c,j}) \quad (2.16)$$

or

$$\mathcal{B}=\mathcal{A}\mathcal{X}. \quad (2.17)$$

Implementing the GMRES method (see section 2.4) this linear system can be solved, hence we obtain the $\mathcal{X}$ vector. Setting also $X_0=X_{N+1}=0$, and dividing each element X_j by the corresponding radius $\rho_{c,j}$, we finally obtain a numerical solution for the values of $S(\rho_{c,j})$ at the grid points of (2.14).

2.3 Structure of the A matrix

As explained above the $\mathcal{A}$ matrix is a NxN matrix whose elements are a_{ij} given in (2.15). A key point to understand the structure of this matrix is computing its support. Its elements are non-zero only when $\rho_{c,j}\le\rho_{c,max}(\rho_i,\rho_{max})$.
We recall now the constraints on the domain with respect to the angular momentum, once the radius ρ_i is fixed and visualize them in Fig. 2.1. The detailed computations needed to derive this and the subsequent figures are given in Chapter 3.
The three lines shown in Fig. 2.1 are computed as follows, each orbiting body has:

- negative energy in order to have a bounded orbit $p_\varphi\le\rho\sqrt{-2\Phi(\rho)}$ (blue line)
- angular momentum lower than the one of the body whose orbit's pericenter is ρ_i and apocenter is ρ_{max} (1.64) (green line).
- angular momentum higher than the one of the circular orbit with radius ρ_i(1.60) (red line).

The allowed values of angular momentum for each ρ_i are limited by these constrains and higlighted in the plot with the yellow area. The condition for a_{ij} being non-zero can now be formulated as follows. For a fixed value of ρ_i we consider the circular radius $\rho_c(\rho_i,\rho_{max})$ of the orbit having the same angular momentum as the one with pericenter ρ_i and apocenter ρ_{max}. This corresponds to the limits imposed in the integral (2.11), (green line in Fig. 2.1). Selecting only the radii $\rho_{c,j}$ such that

$$(p_\varphi^2(\rho_i,\rho_{max})-p_c^2(\rho_j))(p_\varphi^2(\rho_i,\rho_{max})-p_c^2(\rho_{j+1}))\le 0 \quad (2.18)$$

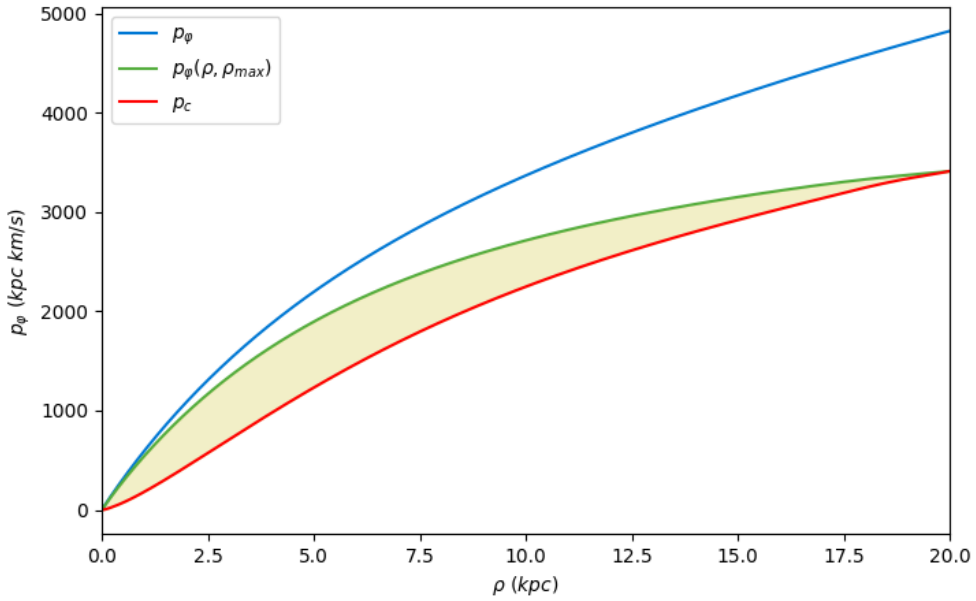

Figure 2.1: Limit on the angular momentum.

we evaluate the limit to allowed values of circular radii $\rho_c(\rho_i, \rho_{max})$ using the interpolation

$$\rho_c(\rho_i, \rho_{max}) = \rho_{c,j} + \frac{\rho_{c,j+1} - \rho_{c,j}}{p_\varphi^2(\rho_i, \rho_{max}) - p_c^2(\rho_{j+1})}(p_\varphi^2(\rho_i, \rho_{max}) - p_c^2(\rho_j)) \tag{2.19}$$

which yields the blue line in Fig. 2.2. The elements a_{ij} can now be calculated as in (2.15), with the

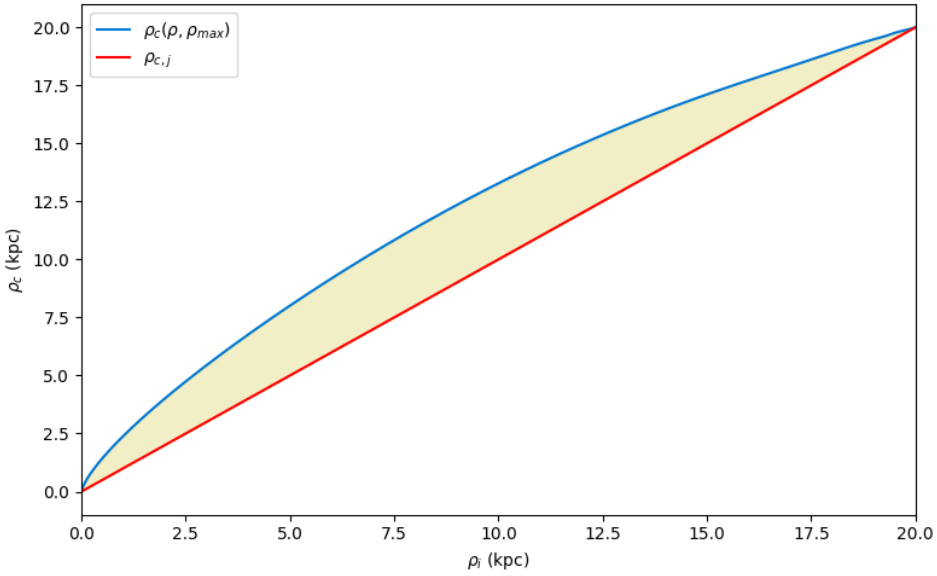

Figure 2.2: Domain of the integration for ρ_c: the yellow area is the area of the allowed values for the circular radius when we consider only bouded orbits inside ρ_{max}.

pairs of $(\rho_i, \rho_{c,j})$ where $\rho_{c,j}$ is lower than the limit imposed by equation (2.19). The elements' graph for different rows, hence different ρ_i, is shown in Fig. 2.3.

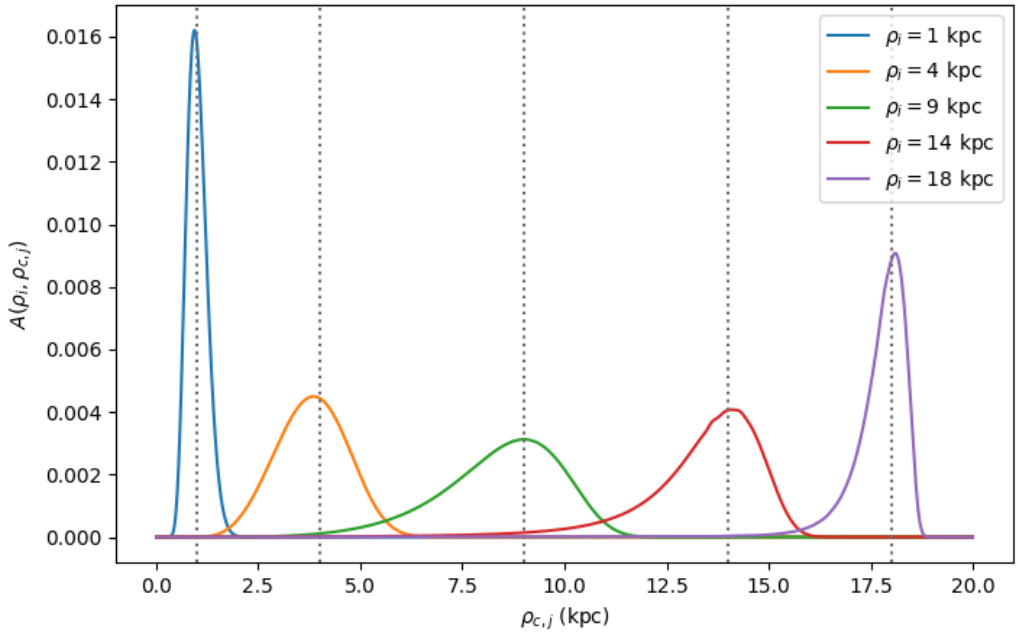

Figure 2.3: Distribution of the a_{ij} elemets for different values of ρ_i, the grey dotted lines are vertical lines with equation $\rho_{c,j} = \rho_i$.

2.3.1 Non-Gaussianity of $A(\rho, \rho_c)$

Figure 2.3 reveals a nearly Gaussian profile of the function $A(\rho, \rho_c)$, considered as a function of ρ_c for fixed ρ. The form of this profile can be understood using epicyclic and post-epicyclic theory.
Consider equation (2.12) for radii far from the disk edges and $\sigma_\rho(\rho_c) \ll v_c(\rho_c)$. The maximum value of the radial velocity domain (1.65) is much higher than the radial dispersion

$$v_{\rho,max}(\rho, \rho_c) = \sqrt{2\left(\mathcal{E}_a(p_\varphi(\rho_c); \rho_{max}) - \frac{p_\varphi^2(\rho_c)}{2\rho^2} - \Phi(\rho)\right)} >> \sigma_\rho(\rho_c) \tag{2.20}$$

therefore the error function goes to unity. Performing Taylor expansion of the argument of the exponential of the DF

$$\begin{aligned} \Phi(\rho) &\simeq \Phi(\rho_c) + \left.\frac{\partial\Phi}{\partial\rho}\right|_{\rho_c}(\rho - \rho_c) + \frac{1}{2}\left.\frac{\partial^2\Phi}{\partial\rho^2}\right|_{\rho_c}(\rho - \rho_c)^2 + \mathcal{O}((\rho - \rho_c)^3) \\ \frac{\rho_c^4\Omega^2(\rho_c)}{\rho^2} &\simeq \rho_c^4\Omega^2(\rho_c)\left[\frac{1}{\rho_c^2} - \frac{2}{\rho_c^3}(\rho - \rho_c) + \frac{3}{\rho_c^4}(\rho - \rho_c)^2 + \mathcal{O}((\rho - \rho_c)^3)\right] \end{aligned} \tag{2.21}$$

and simplifying it as

$$\begin{aligned} -\frac{1}{2\sigma_\rho^2(\rho_c)}\left[\frac{\rho_c^4\Omega^2(\rho_c)}{\rho^2} - \Omega^2(\rho_c)\rho_c^2 + 2(\Phi(\rho) - \Phi(\rho_c))\right] \simeq -\frac{1}{2\sigma_\rho^2(\rho_c)}[-2\Omega^2(\rho_c)\rho_c(\rho - \rho_c) + 3\Omega^2(\rho_c)(\rho - \rho_c)^2 + \\ +2\left.\frac{\partial\Phi}{\partial\rho}\right|_{\rho_c}(\rho - \rho_c) + \left.\frac{\partial^2\Phi}{\partial\rho^2}\right|_{\rho_c}(\rho - \rho_c)^2 + \mathcal{O}((\rho - \rho_c)^3)] \end{aligned} \tag{2.22}$$

leads to the "epicyclic" estimate for $A(\rho, \rho_c)$

$$A(\rho, \rho_c) \simeq \left(\frac{\kappa(\rho_c)}{\sqrt{2\pi}\sigma_\rho(\rho_c)}\right) e^{-\frac{\kappa(\rho_c)^2}{2\sigma_\rho^2(\rho_c)}(\rho - \rho_c)^2}. \tag{2.23}$$

Fixing the value of ρ, equation (2.23) can be interpreted as a Gaussian distribution of ρ_c centered in ρ with dispersion $\sigma_e(\rho_c) = \sigma_\rho(\rho_c)/\kappa(\rho_c)$. This result is coherent with the nearly Gaussian profiles shown in Fig. 2.3.

The fact that the resulting distributions are not exactly Gaussian can than be justified with two arguments:

- in equation (2.22) we have ignored the cubic and higher order corrections of post-epicyclic theory. Such corrections lead to asymmetries of the profile of $A(\rho, \rho_c)$ with respect to the Gaussian profile.
- the truncation of the disk combined with imposing self-consistency for all its extent causes variations in the kinematical properties of the disk, which contribute to the asymmetries in $A(\rho, \rho_c)$.

To better understand this last argument, consider the functions

$$\begin{aligned} \mathcal{N}(\rho_i) &= \int_0^{\rho_{c,max}(\rho_i;\rho_{max})} A(\rho_i;\rho_c)d\rho_c \simeq \sum_{j=1}^{N-1} a_{ij} \\ \overline{\rho}_c(\rho_i) &= \frac{1}{\mathcal{N}(\rho_i)} \int_0^{\rho_{c,max}(\rho;\rho_{max})} \rho_c A(\rho_i;\rho_c)d\rho \simeq \frac{1}{\mathcal{N}(\rho)_i} \sum_{j=1}^{N-1} \rho_{c,j} a_{ij} \end{aligned} \tag{2.24}$$

$$\sigma_{\rho_c}(\rho_i) = \frac{1}{\mathcal{N}(\rho)} \int_0^{\rho_{c,max}(\rho;\rho_{max})} (\rho_c - \overline{\rho}_c)^2 A(\rho_i;\rho_c)d\rho_c \simeq \frac{1}{\mathcal{N}(\rho)} \sum_{j=1}^{N-1} \rho_{c,j}^2 a_{ij} - \overline{\rho}_c^2(\rho_i). \tag{2.25}$$

Their corresponding profiles are shown in Fig. 2.4. The left panel demonstrates that the mean circular radius ($\overline{\rho_c}$) equals ρ in the inner regions of the disk where its distribution follows a Gaussian profile as expected from epicyclic approximation (this is clarified in the right panel where the two profiles have the same dispersion $\sigma_{\rho_c} = \sigma_e$). As we move outwards, from 10kpc to the end of the disk, the $\overline{\rho_c}$ values and their corresponding dispersion are higher than expected from epicyclic approximation. This behaviour of the bodies is consistent with the fact that since we are truncating the disk, bodies with higher dispersion are generated close to the edge of the disk to ensure self-consistency even in absence of particles beyond ρ_{max}.

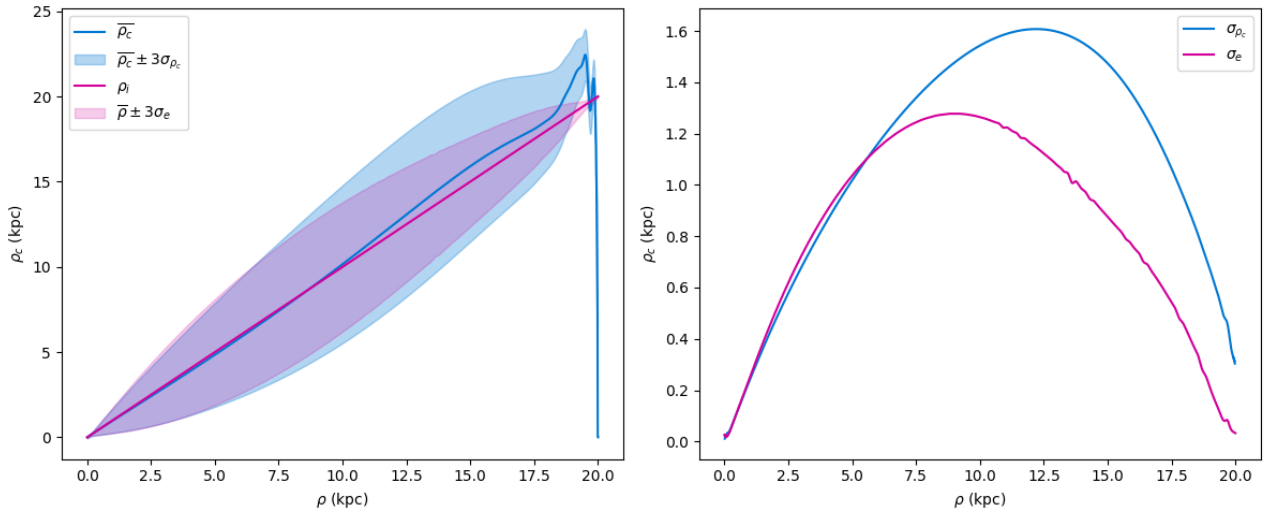

Figure 2.4: Left panel: comparison between the mean value of ρ_c expected from epicyclic approximation (pink line) and by integrating the DF (blue line), the highlighted area is the area within 3σ for the two profiles. Right pane: dispersion profile expected from epicyclic approximation (pink line) and by integrating the DF (blue line).

2.4 Solution of the linear system

As typical for inverse problems, the linear system (2.17) has a high condition number. Furthermore the $\mathcal{A}$ matrix's support is concentrated around its diagonal (Fig. 2.3). Tikhonov regularization allows to control the above conditioning problems (Golub, Hansen, and O'leary 2000). To implement Tikhonov regularization we rephrase the system as

$$(\mathcal{A}^T\mathcal{A} + \lambda I)\mathcal{X} = \mathcal{A}^T\mathcal{B} \tag{2.26}$$

where I is the identity matrix with dimension $N-1 \times N-1$ and λ is the regularization parameter that controls the trade-off between fidelity to the data and solution smoothness (we choose $\lambda = 10^{-6}$).

This linear system is solved using Generalized Minimal Residual (GMRES) method (see for example Saad and Schultz 1986). This procedure that is chosen because it performs well in systems where the inverse matrix can not be derived (as in the case of $(\mathcal{A}^T\mathcal{A} + \lambda I)$).
To simplify the explanation on how this method works we write the system as $Mx = K$ where $M = \mathcal{A}^T\mathcal{A} + \lambda I$, $x = \mathcal{X}$ and $K = \mathcal{A}^T\mathcal{B}$. Implementing a GMRES iterative method we look for a solution in the Krylov subspace

$$\mathcal{K}_n(M, r_0) = \text{span}\{r_0, Mr_0, M^2r_0, ..., M^{n-1}r_0\} \tag{2.27}$$

where $r_0 = K - Mx_0$ and x_0 is the initial guess. For each iteration a new orthonormal basis is built and is chosen the solution such that $||Mx_k - K||$ is minimized. The iterations continue until the residual is smaller than the imposed tolerance (10^{-6}).
The result of these computations is presented in Fig. 2.5. The left panel shows the curves $\Sigma_D(\rho)$ (blue line, Eq. 3.1) and $S(\rho)$ (red line) whose relative difference is shown with red dots on the right panel. The discrepancy between the two profiles is of the order of 10%. This is in agreement with the general level of discrepancy between the imposed and response profiles obtained in iterative methods similar to ours (see for example Dehnen 1999). In the central part of the disk, this effect is coherent with the results presented in Fig. 2.3: at the edges the a_{ij} values are less dispersed, therefore the matrix looks like the identity and $S(\rho)$ is closer to Σ_D, in the internal region the matrix' elements are more dispersed. Therefore $S(\rho)$ has lower values because the peak of the nearly Gaussian profile is smaller. The error in the integration is of the order of 10^{-6} (blue dots in the right panel), that is exactly the tolerance imposed for the GMRES method meaning that the solution is reliable and the self-consistency condition is respected.

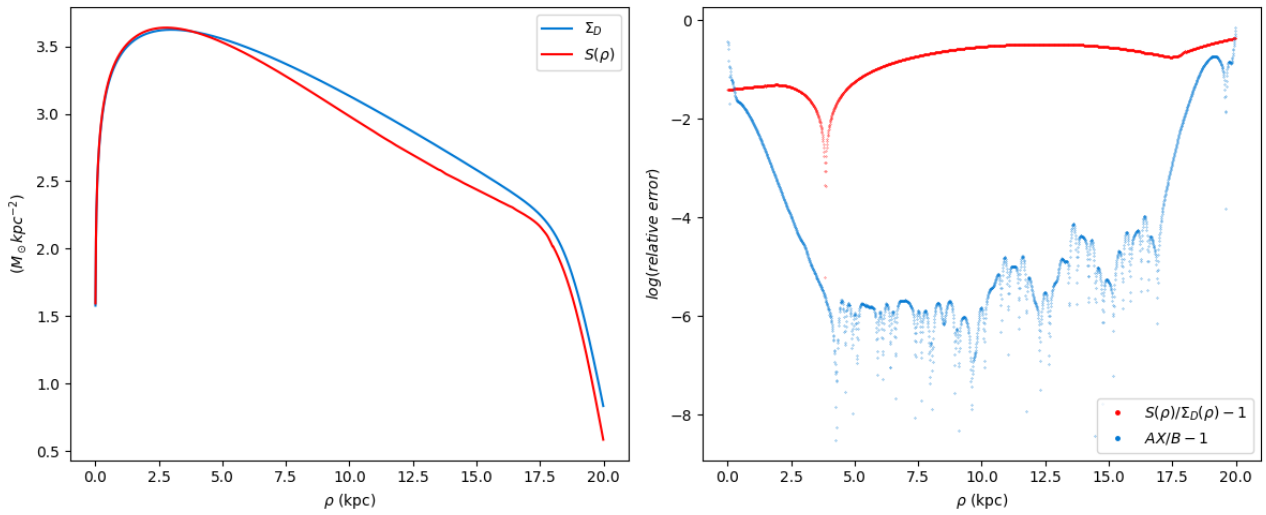

Figure 2.5: Left panel: input surface density profile for the disk (blue line) and $S(\rho)$ profile obtained solving the linear system. Right pannel: relative error on logaritmic scale for the $\Sigma_D(\rho)$ and $S(\rho)$ functions (red dots) and of the system (2.17) (blue dots).

2.5 Comparison with other models

In this section we compare our distribution function model with standard expressions from the literature: f_{Shu} (1.40), $f_{\text{Schwarzschild}}$ (1.43), $f_{\text{Hernquist}}$ (1.45), and the epicyclic DF (see the next paragraph).

For a consistent comparison, we examine the distribution of azimuthal velocity predicted by each model. For a fixed radius ρ, we integrate the DF over v_ρ within the velocity domain defined by equation (2.20), and normalize it

$$F(v_\varphi, \rho) = \frac{1}{\iint_{\mathcal{D}_v} f(\rho, v_\rho, v_\varphi)\,\mathrm{d}v_\rho \mathrm{d}v_\varphi} \int_{-v_{\rho,\max}(v_\varphi,\rho)}^{v_{\rho,\max}(v_\varphi,\rho)} f(\rho, v_\rho, v_\varphi)\,\mathrm{d}v_\rho. \tag{2.28}$$

The resulting distributions at $\rho = 3, 6, 9, 12, 15$, and 18 kpc are shown in Fig. 2.6, and a summary of the profile comparison is reported in Table 2.1.

Epicyclic model of the distribution function

Starting from the epicyclic approximation of the argument of the exponential given in (2.23) a new expression of the distribution function can be derived considering various post-epicyclic approximations.
We start from the expression of the DF

$$f(\rho, v_\rho, v_\varphi) = \frac{S(\rho - \delta\rho)}{2\pi\sigma_\rho(\rho - \delta\rho)\sigma_\varphi(\rho - \delta\rho)} e^{-\frac{1}{2\sigma_\rho^2(\rho-\delta\rho)}(v_\rho^2 + \kappa^2(\rho)\delta\rho^2)} \tag{2.29}$$

where $\rho = \rho_c + \delta\rho$. We rephrase the expression of the DF in order to make it directly dependent on δv_φ. We have that

$$\delta v_\varphi = v_\varphi - v_c(\rho) = \rho\Omega(\rho) - \frac{(\rho - \delta\rho)^2\Omega(\rho - \delta\rho)}{\rho} + \mathcal{O}(\delta\rho^2) = \frac{\kappa^2(\rho)}{2\Omega(\rho)}\delta\rho + \mathcal{O}(\delta\rho^2). \tag{2.30}$$

Using the taylor expansion

$$\begin{aligned}
&(\rho - \delta\rho)^2 = \rho^2 - 2\rho\delta\rho + \mathcal{O}(\delta\rho) \\
&\Omega(\rho - \delta\rho) \simeq \Omega(\rho) - \left.\frac{\partial\Omega}{\partial\rho}\right|_\rho \delta\rho + \mathcal{O}(\delta\rho) \\
&\frac{(\rho - \delta\rho)^2\Omega(\rho - \delta\rho)}{\rho} \simeq \rho\Omega(\rho) - \frac{3\Omega(\rho)}{2}\delta\rho - \frac{1}{2\Omega(\rho)}\left.\frac{\partial^2\Phi}{\partial\rho^2}\right|_\rho \delta\rho + \mathcal{O}(\delta\rho^2)
\end{aligned} \tag{2.31}$$

the new expression for the DF is derived substituting $\delta\rho$ with δv_φ and considering only the order of the expansions revelant for epicyclic theory. This results in the Gaussian profile of the DF (2.32).

$$f_{epicyclic}(\rho, v_\rho, v_\varphi) = \frac{S(\rho)}{2\pi\sigma_\rho(\rho)\sigma_\varphi(\rho)} e^{-\frac{v_\rho^2}{2\sigma_\rho^2(\rho)} - \frac{4\Omega^2(\rho)}{2\sigma_\rho^2(\rho)\kappa^2(\rho)}(\delta v_\varphi^2 + \mathcal{O}(\delta v_\varphi^3))} \simeq \frac{S(\rho)}{2\pi\sigma_\rho(\rho)\sigma_\varphi(\rho)} e^{-\frac{v_\rho^2}{2\sigma_\rho^2(\rho)} - \frac{\delta v_\varphi^2}{2\sigma_\varphi^2(\rho)}} \tag{2.32}$$

More accurate expressions of the DF could be derived using post-epicyclic theory. To consider higher order terms for $\delta\rho$ expansion we write δv_φ as

$$\delta v_\varphi = \frac{\kappa^2(\rho)}{2\Omega(\rho)}\delta\rho + \sum_{s=2}^{\infty} C_s(\rho)\delta\rho^s \tag{2.33}$$

where $C_s(\rho)$ are the coefficients of the terms of s-th order in $\delta\rho$ in (2.33). Inverting then leads to

$$\delta\rho = \frac{2\Omega(\rho)}{\kappa^2(\rho)}\delta v_\varphi + \sum_{s=2}^{\infty} D_s(\rho)\delta v_\varphi^s \tag{2.34}$$

and substituting this quantity in the expression of the DF (2.32) we can rephrase it as

$$f_{post-epicyclic}(\rho, v_\rho, v_\varphi) = \frac{S(\rho)}{2\pi\sigma_\rho(\rho)\sigma_\varphi(\rho)} e^{-\frac{v_\rho^2}{2\sigma_\rho^2(\rho)} - \frac{\delta v_\varphi^2}{2\sigma_\varphi^2(\rho)}(1+f^{(1)}(\rho,v_\varphi)+f^{(2)}(\rho,v_\varphi)+...)} \tag{2.35}$$

where the functions $f^{(k)}(\rho, v_\varphi)$ are the post-epicyclic corrections. The explicit evaluation of these higher order terms requires lengthy derivations that go beyond the aims of this thesis.

Model of DF	Comparison with the modified Shu DF model adopted in this work
Shu	The velocity distribution predicted by the original Shu DF is remarkably similar to that obtained with the modified Shu model implemented in this thesis. The Shu DF accurately reproduces the kinematic properties of the disk, in particular the shape and asymmetry of the v_φ distribution. However recall that it does not exactly reproduce the imposed surface density profile, since integrating the distribution function this result is not garantueed.
Schwarzschild	The Schwarzschild DF retains some degree of asymmetry in the velocity distribution, even if it is less precise than the Shu model. Specifically for higher radii the discrepancies from Shu model increases because we are neglecting cubic and higher order corrections of post-epicyclic theory whose relevance increases in the outer regions of the disk. Therefore this model well reproduces the distribution function in the internal part of the disk, but fails when moving outwards.
Epicyclic	The epicyclc distribution function takes the form of a Gaussian-shaped curve, therefore this models fails to reproduce the intrinsic asymmetries of the DF. This is because the asymmetries are related to post-epicyclic corrections of third and higher orders that are neglected for this DF. However in the inner regions of the disk this DF is a good approximation for the velocity distribution. In the external disk post-epicyclic corrections become more relevant hence the models is not able to reproduce the Shu model of the DF. The comparison between this DF and Schwarzschild model reveals their similarity that is related to the fact that these expressions of the DF take into account the same order of epicyclic corrections.
Hernquist	Among the models considered, the Hernquist DF provides the poorest match to the modified Shu DF. Not only does it fail to reproduce the velocity distribution asymmetries due to its Gaussian form, but it also incorrectly centres the Gaussian peak at a value of v_φ that is inconsistent with the expected mean rotational velocity of the disk.

Table 2.1: Qualitative comparison between different DF models from the literature and the modified Shu DF adopted in this thesis, in terms of their ability to reproduce the v_φ distribution.

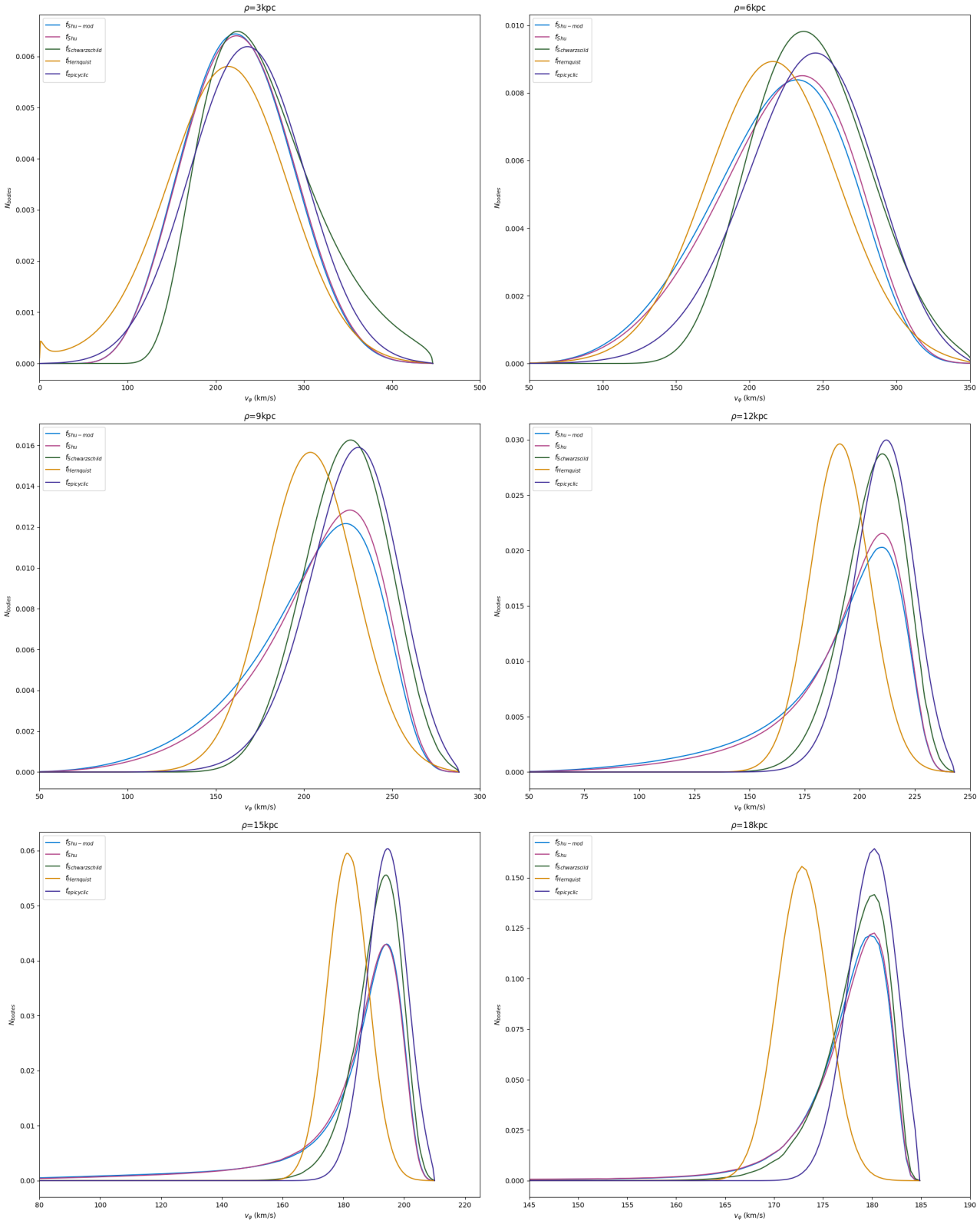

Figure 2.6: Comparison of the v_φ distribution depending on the chosen model of the DF for different radii: bule line for the modified Df of the Shu model, the pink line for the Shu DF, the green line for the Schwarzschild DF and the orange line for the Hernquist DF.

Chapter 3

Example of a galactic model

In this chapter we use our new model of the distribution function, developed in Section 1, in order to generate initial conditions of an N-body realisation of a galactic disk. The equilibrium of the component is checked via N-body simulations, in which the disk is assumed to interact with a dark matter halo and a bulge.
For each component we prescribe input profiles intended to reflect realistic systems; nevertheless, the algorithm is deliberately general and, for any admissible choice of initial particles, yields a disk that is self-consistent and in dynamical equilibrium.

3.1 Disk's initial conditions

The first input function for the disk is the exponential profile of surface density

$$\Sigma_D(\rho) = W_D(\rho)\Sigma_0 e^{-\rho/\rho_D} \tag{3.1}$$

The window function $W(\rho)$ is introduced in order to avoid abrupt truncations at the edge of the system. We adopt the window function model

$$W_D(\rho) = \frac{1}{2}\left(1 + \tanh\left(-\frac{\rho - \rho_2}{d_2}\right)\right) \tag{3.2}$$

that smooths the function at high radii. The parameters used for the disk are reported in Table 3.1 and the central value Σ_0 is calculated numerically knowing that the total mass of the disk equals the integral of surface density over the area element as

$$M_D = \int_0^\infty 2\pi W_T(\rho)\Sigma_0 e^{-\rho/\rho_D}\rho d\rho \tag{3.3}$$

$$\Sigma_0 = \frac{M_D}{\int_0^\infty 2\pi W_T(\rho)e^{-\rho/\rho_D}\rho d\rho}. \tag{3.4}$$

M_D	ρ_D	$\rho_{min,disk}$	$\rho_{max,disk}$	ρ_2	d_2
$5 \cdot 10^{10} M_\odot$	3 kpc	0 kpc	20 kpc	18.7kpc	1 kpc

Table 3.1: Disk's input parameters

The resulting surface density profile is shown in Fig. 3.1.

Once the surface density profile is known the potential exerted by the disk can be derived solving the integral

$$\Phi_D(\rho) = -G\int_0^{M(\rho)} \frac{\mathrm{dm}}{\|\vec{r_i} - \vec{r}\|} = -G\int_0^{\rho_{max}}\int_0^{2\pi} \frac{\Sigma(\rho')\rho' d\rho' d\varphi}{\sqrt{\rho^2 + \rho'^2 - 2\rho\rho'\cos(\varphi)}} \tag{3.5}$$

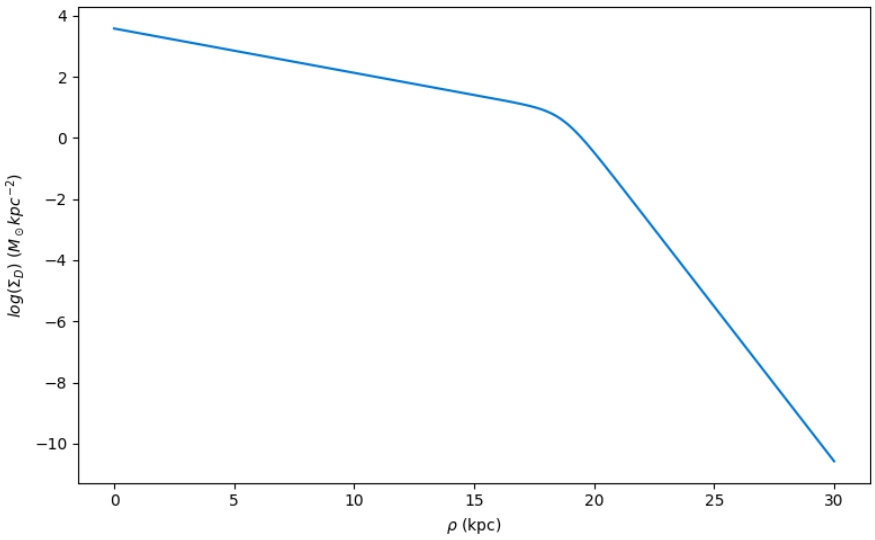

Figure 3.1: Surface density profile of the disk.

(see Fig. 3.2). The two-dimensional integral was evaluated with `nquad` function from the `scipy.integrate` module in Python that allows the integration over multiple variables, for our computations we imposed relative tolerance of tol=10^{-6}. In the following calculations the total potential of the system is taken into account, therefore the disk (3.5), halo and bulge (3.26) contributions to the total potential $\Phi(\rho)$ are summed as in (1.59). As a second input function, we prescribe the profile of Toomre's parame-

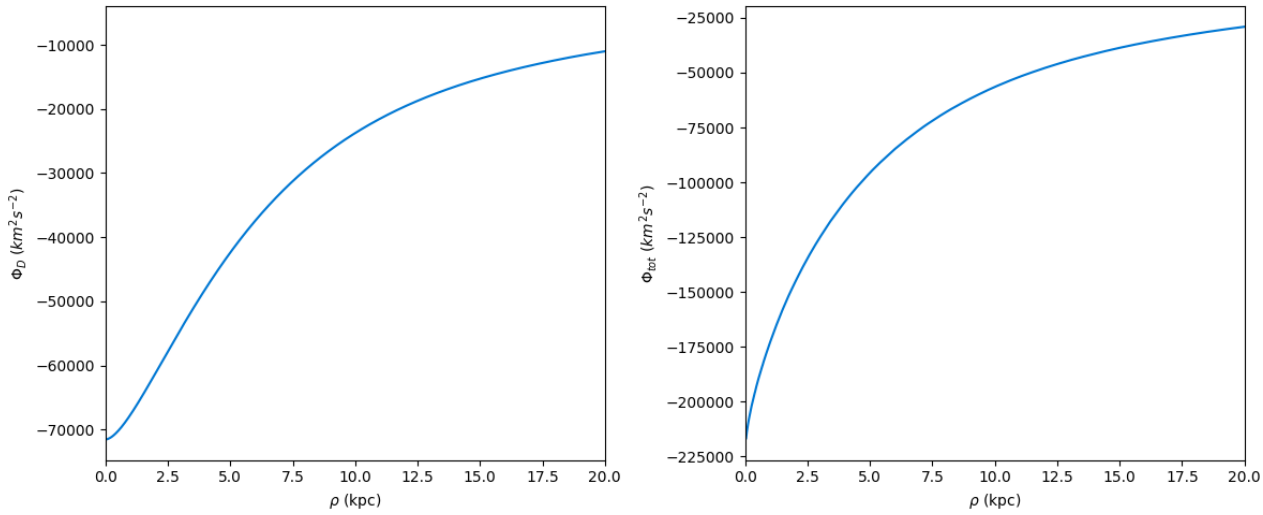

Figure 3.2: Left panel: potential exerted by the disk. Right panel: total potential on the disk plane when considering the contribution of the spherical components.

ter $Q(\rho)$. According to Toomre's criterion, this parameter controls local axisymmetric stability, with $Q(\rho) > 1$ indicating stable conditiions (Toomre 1964).
A simple model could be chosen for this profile is

$$Q(\rho) = Q_\infty + (Q_0 - Q_\infty)e^{-\rho/\rho_D} \tag{3.6}$$

with $Q_0 = 2.5$ and $Q_\infty = 2$. For our disk we modify the exponential law introducing a new function

$$Q(r) = \left(Q_0 + (Q_1 - Q_0)e^{-r/0.01}\right) w_q(\rho) + Q_\infty + (Q_0 - Q_\infty)e^{-r/r_q}\left(1 - w_q(\rho)\right) \tag{3.7}$$
$$w_q(\rho) = \frac{1}{2}\left(1 + \tanh\left(-\frac{\rho - 0.05}{0.01}\right)\right)$$

with $Q_1 = 5.0$. This correction increases the Q value in the inner regions (as seen in Fig. 3.3) increasing their stability. The reason behind this choice will be better understood in Section 3.3 .

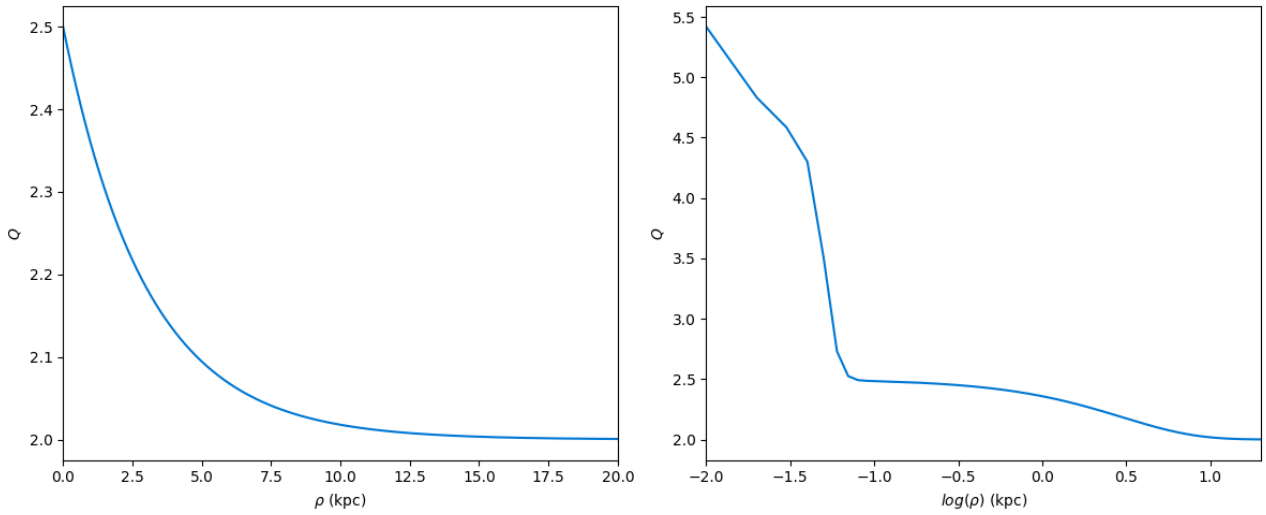

Figure 3.3: Left pannel: simple model of $Q(\rho)$ (3.6). Right pannel: modified profile (3.7) with radial logarithmic scale.

Once we have imposed the Toomre profile we are able to derive the kinematical properties of the disk. The angular and epicyclic frequencies can be calculated using equations (1.61) and (1.62), their profiles are shown on the left panel in Fig. 3.4. Furthermore $\Omega(\rho) \pm \kappa(\rho)/2$, for a perturbation with pattern speed Ω_p, the intersections with $\Omega - \kappa/2$, Ω, and $\Omega + \kappa/2$ mark, respectively, the inner Lindblad resonance (ILR), corotation (CR), and the outer Lindblad resonance (OLR); these resonances delineate the regions where bars and spiral density waves can be maintained (Binney and Tremaine 2008). On the right panel of Fig. 3.4 is illustrated the velocity dispersion profile in radial (red line) and azimuthal (green line) directions: σ_ρ is given by

$$\sigma_\rho(r) = \frac{3.36 G \Sigma_D(r) Q(r)}{\kappa(r)} \tag{3.8}$$

and σ_φ is

$$\sigma_\varphi(\rho) = \frac{\kappa(\rho)\sigma_\rho(\rho)}{2\Omega(\rho)}. \tag{3.9}$$

Once we have obtained these initial profiles we are able to determine all the A matrix elements and the B vector, therefore we can solve the linar system to obtain $S(\rho)$ as explained is Section 2, therefore finally we have the expression of the self-cosistent DF.

3.1.1 The rejection algorithm

Once the expression of the distribution function is known we can implement the rejection algorithm to generate the initial positions and velocities of the bodies (as explained in Section 1.13).
Firstly an estimate of the higher limit of F is needed: considering the three-dimensional grid

$$\begin{gathered} \rho_i = i\delta\rho \text{ where } i = 0, ..., N \text{ and } \delta\rho = \rho_{max}/N \\ v_{\rho,j} = j\delta v_\rho \text{ where } j = -N/2, ..., N/2 \text{ and } \delta v_\rho = 2\sqrt{-2\Phi(\rho=0)}/N \\ v_{\varphi,k} = j\delta v_\varphi \text{ where } k = 0, ..., N \text{ and } \delta v_\rho = \sqrt{-2\Phi(\rho=0)}/N \end{gathered} \tag{3.10}$$

with N=1000, we evaluate F for each possible combination of varialbes using the expression (1.71) and considering as limit for F the value $F_{max} = 2\max(F(\rho_i, v_{\rho,j}, v_{\varphi,k}))$. Now we implement the rejection

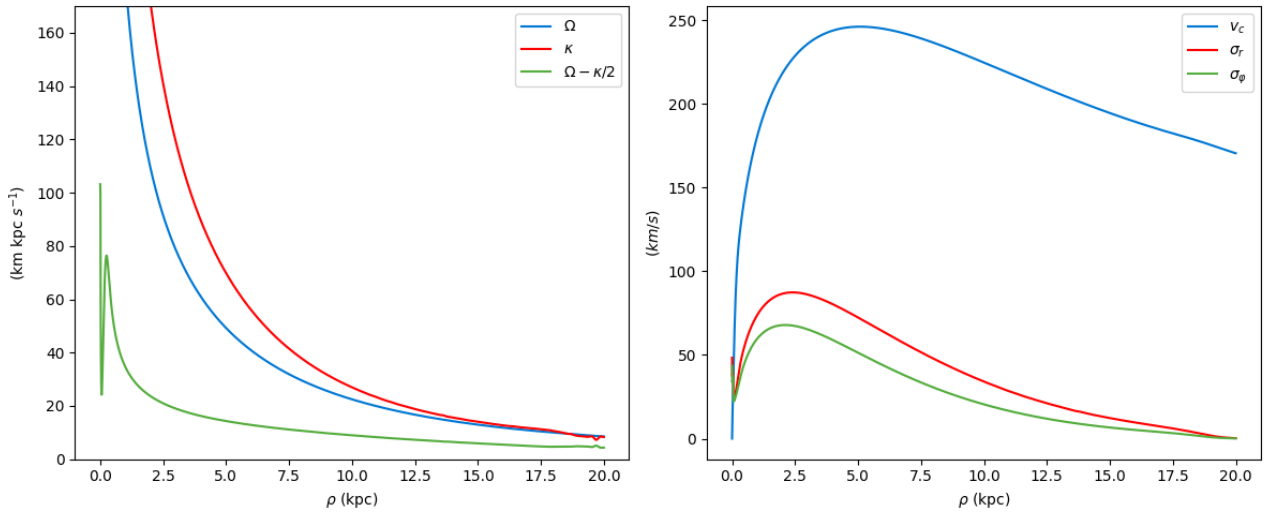

Figure 3.4: Left panel: angular (blue line) and epicyclic (green line) frequencies. Right panel: circular velocity profile (blue line) compared with radial (red line) and angular (green line) velocity dispersions.

algorithm to generate the initial positions and velocities in polar coordinates for $N_D = 10^6$ bodies: start considering quadruplets of random values $(\rho, v_\rho, v_\varphi, \hat{F})$ limiting them as

$$\begin{gathered} 0 \leq \rho \leq \rho_{max} \\ -\sqrt{-2\Phi(\rho=0)} \leq v_\rho \leq \sqrt{-2\Phi(\rho=0)} \\ 0 \leq v_\varphi \leq -\sqrt{2\Phi(\rho=0)} \\ 0 \leq \hat{F} \leq F_{max} \end{gathered} \tag{3.11}$$

if $\hat{F} \leq F(\rho, v_\rho, v_\varphi)$ we store them as coordinates of the body. Since the system is axisymmetric we can assign to each particle a radom value of polar angle $0 \leq \theta \leq 2\pi$ and generate its cartesian coordinates with

$$\begin{aligned} x &= \rho\cos\theta \\ y &= \rho\sin\theta \\ v_x &= v_\rho\cos\theta - v_\varphi\sin\theta \\ v_y &= v_\rho\sin\theta + v_\varphi\cos\theta \end{aligned} \tag{3.12}$$

A final quantity needed to follow the system's evolution is the mass assigned to each body. Because the disk is truncated at $\rho_{\max}$, the mass enclosed within this radius is smaller than the nominal disk mass M_D set by the input profile. The mass of the truncated disk is the integral of the surface density over the area element

$$M_{trunc,disk} = 2\pi \int_{\rho_{min,disk}}^{\rho_{max,disk}} \Sigma_D(\rho')\rho'^2 d\rho'. \tag{3.13}$$

Dividing this number by N_D we can calculate the mass of each body.

3.1.2 Thickness of the disk

Up to this point, the disk has been treated as razor-thin, with $z = 0$ and $v_z = 0$ for all particles. To introduce a finite thickness, we adopt the vertical distribution function (1.50) and assume a constant ratio $\sigma_z/k_z \equiv d_z$, so the distribution function in the z-dimension can be written as:

$$f_z(z, v_z) = \frac{1}{2\pi\sigma_z d_z} e^{-\frac{v_z^2}{2\sigma_z^2} - \frac{z^2}{2d_z^2}}. \tag{3.14}$$

We notice that d_z can be interpreted as the scaling height parameter along the z direction. Imposing $d_z = 0.2$kpc we assign the z coordinate to each body distributing them on a Gaussian profile centered in $z = 0$ with dispersion d_z.

As for the velocities the dispersion of the Gaussian profile $\sigma_z(\rho) = k_z(\rho)d_z$ depends on the radius. First we determine the frequency of the oscillation on the z axis by calculating the second derivative of the potential with respect to z on the $z = 0$ plane for different values of ρ

$$\kappa_z(\rho, z) = \sqrt{\frac{\partial^2 \Phi(\rho, z)}{\partial z^2}\bigg|_{z=0}}. \tag{3.15}$$

Since the value of the derivative is needed only in the plane we compute it using the numerical expression

$$\Phi''(\rho, 0) \approx \frac{\Phi(\rho, h) - 2\Phi(\rho, 0) + \Phi(\rho, -h)}{h^2} \tag{3.16}$$

imposing $h = 0.6$kpc. The z profile of the potential is calculated using equation

$$\Phi(\rho, \theta, h) = \sum_i^N - \frac{Gm_i}{\sqrt{(x_i - \rho\cos\theta)^2 + (y_i - \rho\sin\theta)^2 + (z_i - h)^2}} \tag{3.17}$$

where is considered the gravitational influence of each body of the galaxy (therefore bulge and halo's bodies are considered in this computation). The profile of the potential for $z = 0$kpc, $z = 0.6$kpc and $z = -0.6$kpc is illustrated on the left panel in Fig. 3.5. The algorithm implemented to generate

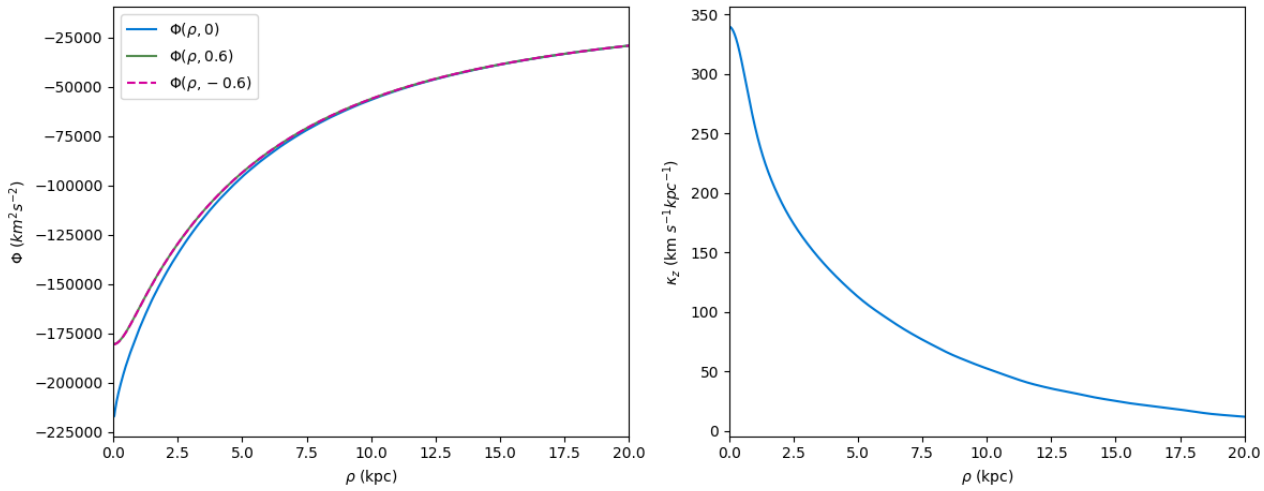

Figure 3.5: Left panel: profile of the total potential on the disk plane ($z = 0$, blue line) and on the two planes used to evaluate the second derivative: $z = 0.6$kpc (green line) and z = -0.6kpc (pink dotted line). Right panel: profile of frequency of vertical oscillations κ_z.

the vertical velocity component of each body is built as follows: first the angular momentum of each particle is evaluated $l_z = xv_y - yv_x$ then inverting equation (1.60) is determined its corresponding circular radius, the v_z coordinate associated to each particle is chosen as a random value subtended by the Gaussian centered in $v_z = 0$ with dispersion $\sigma_z(\rho_c) = \kappa_z(\rho_c)d_z$.
The final results are plotted in Fig. 3.6 where the Gaussian profiles of positions and velocity are well reproduced, focusing on the velocity distribution we can notice that dispersion decreases with radius in agreement with the behaviour of κ_z (Fig. 3.5) as we expected.

3.1.3 Checking the solutions

In this section we test the results obtained above in order to verify if the generated particles behave as imposed by the input profiles.
Two different approaches are adopted for tesing the result:

1. Binning method: dividing the disk in rings of width $\delta\rho = 0.05$kpc we measure for each anulus the mean angular velocity $\overline{v_\varphi}$ and the velocity dispersion profiles for σ_ρ and σ_φ. For these

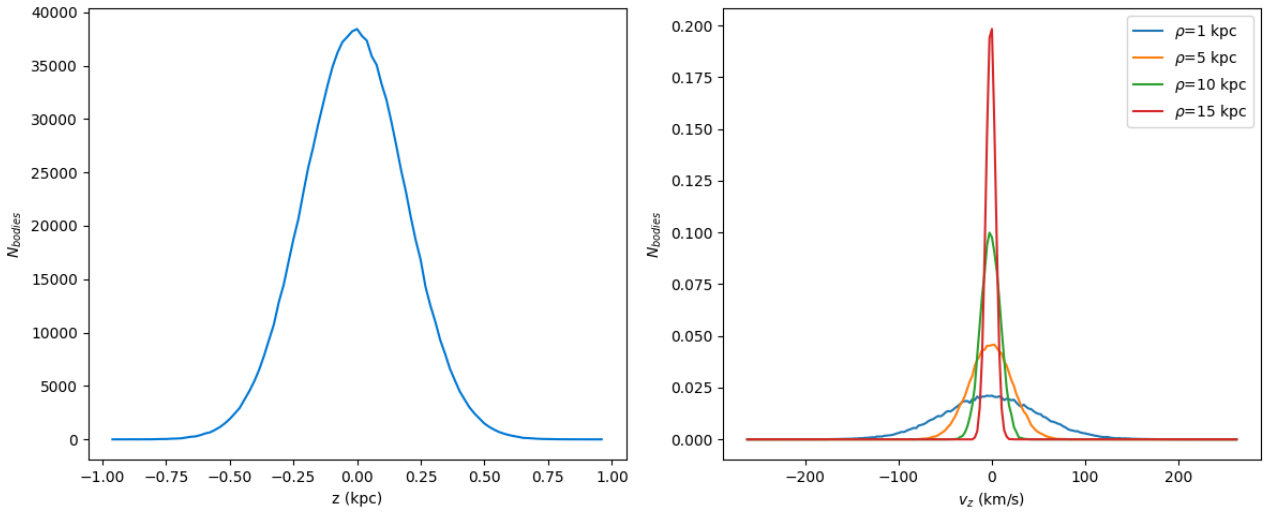

Figure 3.6: Left panel: Gaussian distribution of the z coordinate with dispersion d_z. Right panel: normalized Gaussian distribution of v_z at different radii.

computations we need to transform the cartesian coordinates (resulting from the algorithm) to polar coordinates. For this purpose we consider the equations

$$\begin{aligned} v_\rho &= v_x \frac{x}{\rho} + v_y \frac{y}{\rho} \\ v_\varphi &= v_x \frac{y}{\rho} - v_y \frac{x}{\rho}. \end{aligned} \tag{3.18}$$

Furthermore, counting the number of bodies in each ring can be tested the profile of surface denisty, with equation

$$\tilde{\Sigma}_D(\rho) = \frac{m \cdot n_{bodies}}{2\pi\rho\delta\rho} \tag{3.19}$$

where m is the mass the single body and n_{bodies} is the number of bodies inside each ring.

2. Integration method: considering the distribution function we can evaluate the profiles of the disk solving the integral equations

$$\Sigma_D^{(f)}(\rho) = \int_{\mathcal{D}_v} f(\rho, v_\rho, v_\varphi)\, dv_\rho\, dv_\varphi \tag{3.20}$$

$$\mu^{(f)}(\rho) = \frac{1}{\Sigma_D(\rho)} \int_{\mathcal{D}_v(\rho)} dv_\rho\, dv_\varphi\, v_\varphi\, f(\rho, v_\rho, v_\varphi) \tag{3.21}$$

$$\overline{v_\varphi^2}(\rho) = \frac{1}{\Sigma_D(\rho)} \int_{\mathcal{D}_v(\rho)} dv_\rho\, dv_\varphi\, v_\varphi^2\, f(\rho, v_\rho, v_\varphi) \tag{3.22}$$

$$\overline{v_\rho^2}(\rho) = \frac{1}{\Sigma_D(\rho)} \int_{\mathcal{D}_v(\rho)} dv_\rho\, dv_\varphi\, v_\rho^2\, f(\rho_i, v_\rho, v_\varphi). \tag{3.23}$$

The results of these tests are plotted in Fig. 3.7. The only input profile that is exactly reproduced is the surface density, in agreement with the fact that the system is self consistent and equation (1.66) is perfectly satisfied. As for the other profiles there is a discrepancy between the input and the response profiles. This is due to the fact that for the kinematical properties of the disk we did not impose the exact solutions of the integrations (3.21), (3.22) and (3.23). Specifically if we analyze the Q and velocity dispersion profiles they reveal that the disk's particles are hotter than expected, this phenomenon is related to the requirement of having self consistency for the entire disk combined with the truncation at ρ_{max}. Since bodies close to ρ_{max} do not interact with any particle with bigger radii they need an additional gravitational support by the inner ones to mantain self-consistency, this supply is given increasing the epicyclic frequencies of inner bodies, hence their velocity dispersions and Q profile. However we can notice that the red dotted lines and the blue lines overlap: hence the procedure implemented for generating the initial conditions is coherent with the chosen model of the distribution function even though it does not perfectly represent the initial input profiles.

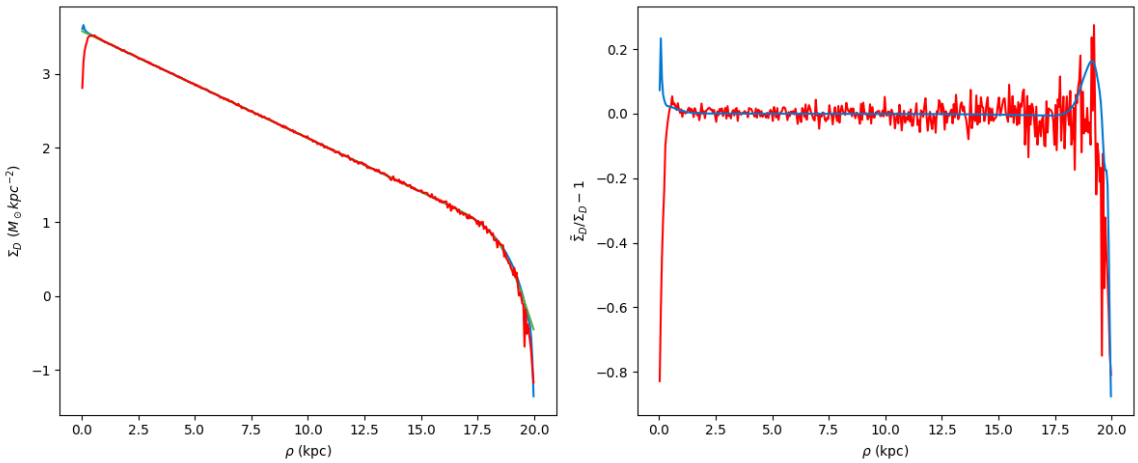

(a) Left panel: surface density profile. Right panel: relative error of the computed profile.

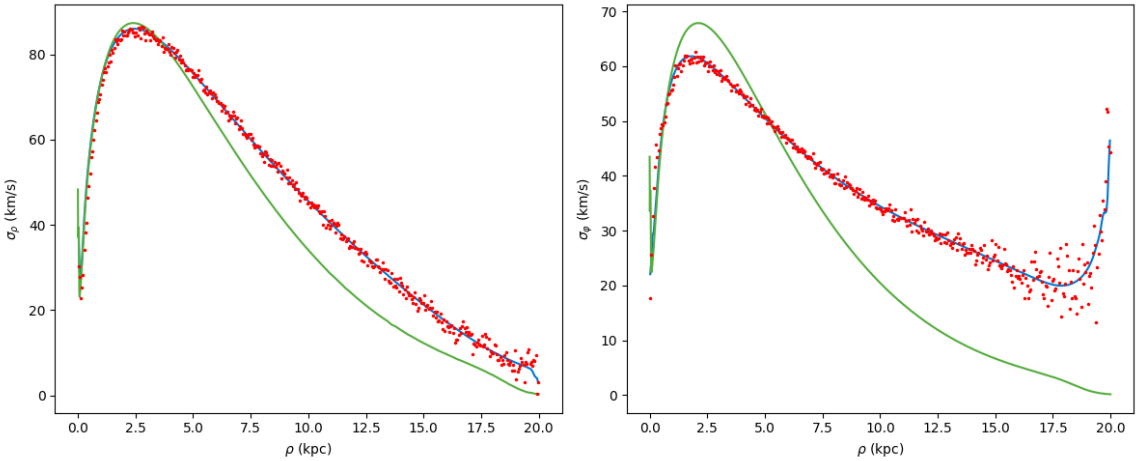

(b) Velocity dispersion profiles in radial (left panel) and angular (right panel) directions.

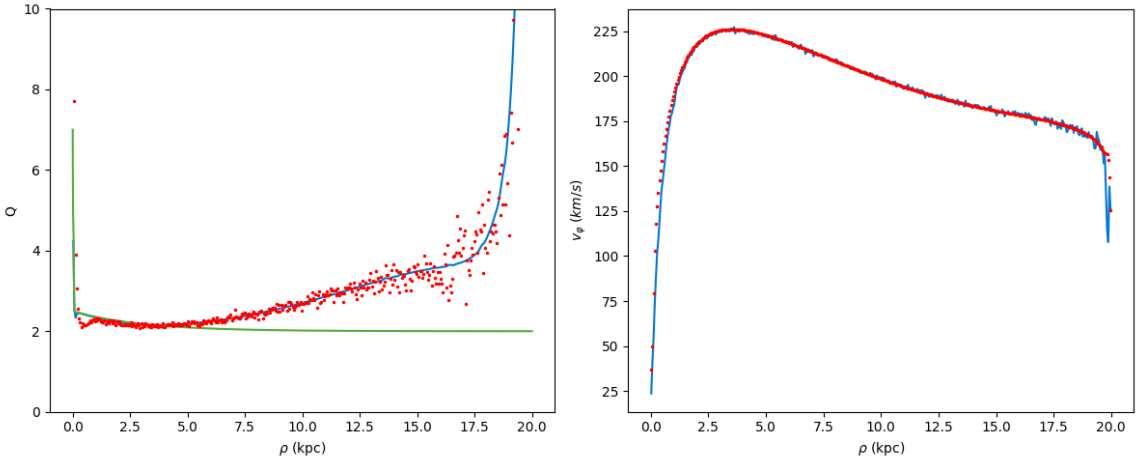

(c) Left panel: Toomre parameter profile. Right panel: mean angular velocity profile.

Figure 3.7: Comparison between input profiles (green lines), those derived from distribution function integration (method 2, blue lines), and those computed binning the disk into equally spaced annuli (method 1, red dots).

3.1.4 Asymmetric drift

Another useful tool to study the dynamics of the disk is the asymmetric dirift (1.38) that will tell us if the system obeys to Jeans equations. Figure 3.8 compares the mean angular velocity measured with the binning method (red dotted line) with the $\overline{v_\varphi}$ obtained using the asymmetric drift formula. Specifically

in the asymmetric drift formula we use the velocity dispersion profiles and circular velocity given by the integration of the distribution function (3.22), (3.20)-blue line and by initial input functions (3.8), (3.9)-green line.
The figure reveals that there is an excellent agreement beween the profile of $\overline{v}_\varphi$ predicted by the integration of the DF and the galaxy's mean angular velocity (as expected from the resusts of the prvious section) hence the DF model obeys to Jeans' equations. When we use the input function to determine the asymmetric drift profile there is not perfect superposition of the curves, this difference arises even in 3.7b where the input velocity dispersion profiles differ from the computed ones, and the same behaviour works for the Q (Fig. 3.7c left panel). This discrepancy is another expression of the differences indicated in the previous paragraph beween the input and ouput kinematical profiles.

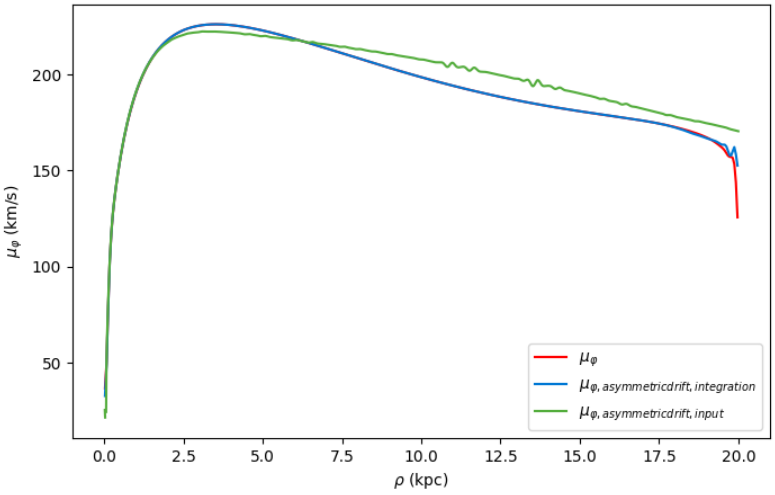

Figure 3.8: Mean angular velocity calculated with the aymmetric drift equation.

3.2 Spherical components

In this section we describe the algorithm implemented to generate the initial conditions of the spherical components: the dark matter halo and the bulge. These two entities are necessary to simulate a disk that behaves as in real galaxies and are chatacterized by two main properties: being isotropic and spherically symmetric.

3.2.1 Dark matter halo

Direct observations are not able to detect the presence of the dark matter halo since it does not emit light, nevertheless the flattening of the rotation curve observed in the galactic system is explained by the presence of this component. Different models for the density of the halo can be adopted, their expressions were derived by fitting the observed data of the velocity profiles with the ones obtained with models. The desity law assumed for our halo is the model proposed by Dehnen (Dehnen 1993)

$$\tilde{\rho}_h(\rho) = \frac{(3-\gamma)GM_{halo}}{4\pi}\frac{a}{\rho^\gamma\,(\rho+a)^{4-\gamma}}W_h(\rho) \tag{3.24}$$

multiplied by the window function

$$W_h(\rho) = \frac{1}{2}\left(1+\tanh\left(-\frac{\rho-\rho_{2,halo}}{d_{2,halo}}\right)\right). \tag{3.25}$$

The parameters imposed in these laws are reported in Table 3.2 and the resulting profile is plotted in Fig. 3.9.

M_{halo}	a	γ	$\rho_{min,halo}$	$\rho_{max,halo}$	$\rho_{2,halo}$	$d_{2,halo}$
$10^{11}M_{\odot}$	3 kpc	0.8 kpc	0kpc	30kpc	$0.85(\rho_{max,halo}+2kpc)$	0.8kpc

Table 3.2: Table of the parameters for the halo.

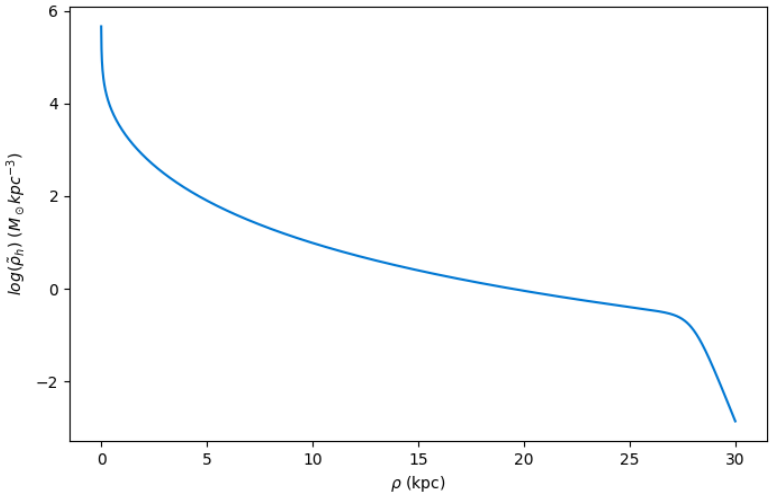

Figure 3.9: Modified NFW density profile assumed for the halo.

Knowing the distribution of bodies their contribution to the total potential can be evaluated through the equation

$$\Phi_h(\rho) = -\frac{G}{\rho}\int_0^{\rho} 4\pi\rho'^2\tilde{\rho}(\rho')\mathrm{d}\rho' - G\int_{\rho}^{\infty} 4\pi\rho'\tilde{\rho}(\rho')\mathrm{d}\rho' \tag{3.26}$$

where the two integrals measure the potential exerted by bodies inside and outside ρ respectively. The resulting profile is shown in Fig. 3.10. On the left panel is illustrated the halo contribution to the total potential (shown on the right panel). It is clear that in the outer regions the presence of the halo becomes more relevant, according to what we expect from the fact that the rotation curves of galactic disk are flattened in the outer regions. Once these profiles are known we can solve Eddington's

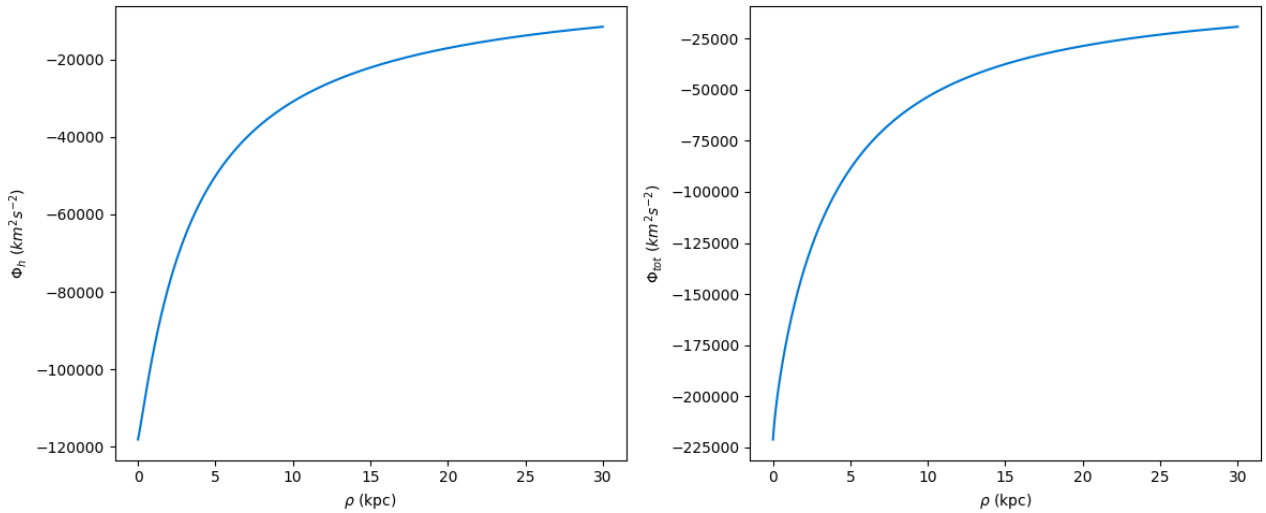

Figure 3.10: Left panel: potential profile of the halo. Right panel: profile of the total potential (halo, bulge and disk).

formula (1.56) to derive the distribution function of the spherical component. The integral of (1.56)

is computed numerically using the `quad` function from the `scipy.integrate` module in Python. The resulting profile of the distribution function is presented in Fig. 3.11.

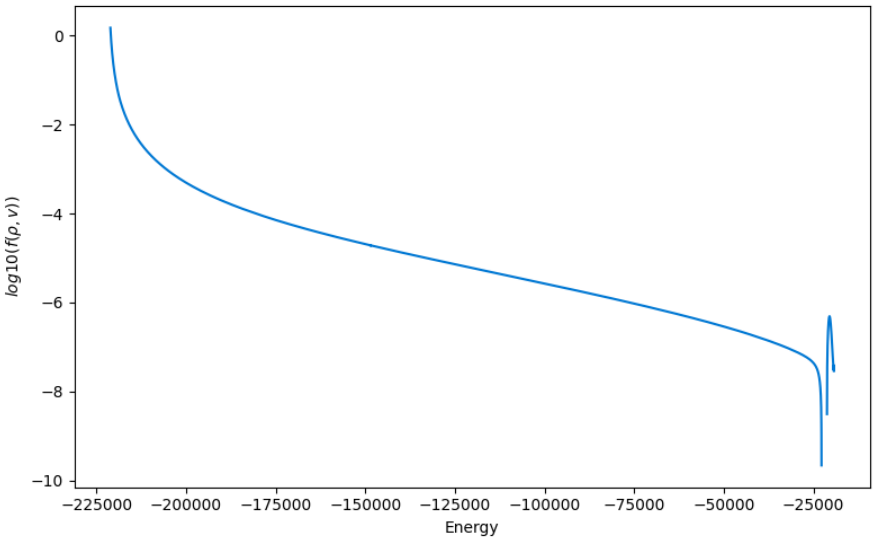

Figure 3.11: Distribution function of the halo.

In order to generate the initial conditions of the halo we implement the rejection algorithm for the spherical components described in Section 1.13, evaluating F weighted by the phase-space volume element (1.69) since the system is spherically symmetric and isotropic. First we need to determine the maximum possible value for F, therefore we consider the two-dimensional grid

$$\begin{aligned} \rho_i &= i\delta\rho \text{ where } i = 0, ..., N \text{ and } \delta\rho = \rho_{max,halo}/N \\ v_j &= j\delta v \text{ where } j = -0, ..., N \text{ and } \delta v = \sqrt{-2\Phi(\rho_{min,halo})}/N \end{aligned} \tag{3.27}$$

where $N = 500$. For each pair of ρ_i, v_j we obtain the corresponding $F(\rho_i, v_j)$ and choose F_{max} as maximum of those doubled. The rejection is implemented generating triplets of $(\rho, v, \hat{F})$ and considering only those such that $\hat{F} < F(\rho, v)$ as initial conditions for the halo. The spherical coordinates of the initial conditions are obtained assigning to each particle random values of polar (θ) and azimuthal angle (ϕ) according to their limitis

$$\begin{gathered} \rho_{min,halo} \leq \rho \leq \rho_{max,halo} \\ 0 \leq v \leq \sqrt{-2\Phi(\rho_{min,halo})} \\ 0 \leq \tilde{F} \leq F_{max} \end{gathered} \tag{3.28}$$

$$\begin{gathered} 0 \leq \theta \leq \pi \\ 0 \leq \phi \leq 2\pi. \end{gathered} \tag{3.29}$$

Finally the cartesian initial coordinates of the halo are calculated using

$$\begin{aligned} x &= r\sin\theta\cos\phi \\ y &= r\sin\theta\sin\phi \\ z &= r\cos\theta \\ v_x &= v\sin\theta\cos\phi \\ v_y &= v\sin\theta\sin\phi \\ v_z &= v\cos\theta. \end{aligned} \tag{3.30}$$

These procedure is repeated until $N_{halo} = 10^6$ bodies are obtained. When studying the evolution of the galactic system is necessary to eavaluate the mass of each particle which is not simply $m_{body} = M_{halo}/N_{bodies}$ because the halo has been truncated at ρ_{max}. To determine the exact maass of the

truncated halo we integrate its density law (3.24) over the volume and divide this quantity by the total number of bodies to derive their corresponding mass m_{body}.

$$M_{trunc,halo} = 4\pi \int_{\rho_{min,halo}}^{\rho_{max,halo}} \rho^2 \tilde{\rho}_h(\rho) d\rho \tag{3.31}$$

3.2.2 Bulge

For the bulge we considered the input profile of the surface denisty

$$\Sigma_{bulge}(r) = \Sigma_{0,bulge} e^{-(2n_b - 0.324)\left(\left(\frac{r}{r_b}\right)^{1/n_b} - 1\right)} \tag{3.32}$$

which is a Sèrsic law providing a flexible and observationally motivated description of spheroidal stellar systems (Graham and Driver 2005). The density law corresponding to this input can be derived through the integral

$$\tilde{\rho}_{bulge}(r) = -\frac{1}{\pi} \int_r^\infty \frac{d\Sigma_{bulge}}{dR} \frac{1}{\sqrt{R^2 - r^2}} dR \tag{3.33}$$

plotted in Fig. 3.12. These profiles present the tipical feature of bulges: most of the mass is concentrated in the inner region. The input parameters used for the bulge are reported in Table 3.3. Similarly as for the halo, we determine the profile of the potential using equation (3.26). The resulting profile is illustrated in Fig. 3.13. It is clear that the contribution of the bulge to the total potential is concentrated in the inner regions where most of its mass is placed (see Fig. 3.13).

M_{bulge}	r_b	n_b	$\rho_{min,bulge}$	$\rho_{max,bulge}$
$5 \cdot 10^9 M_\odot$	1.5kpc	3.5kpc	0.01kpc	30kpc

Table 3.3: Input parameters for the bulge component.

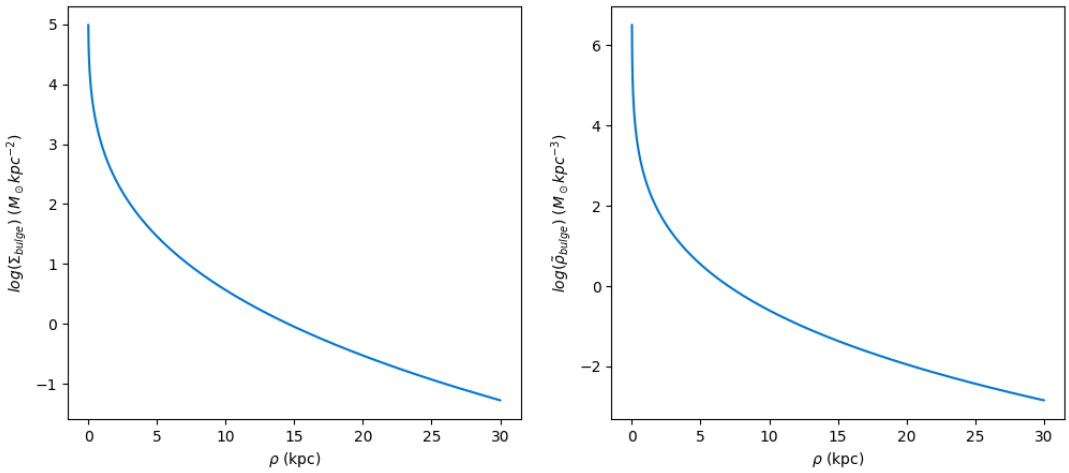

Figure 3.12: Left panel: surface density profile according to Sérsic law. Right panel: mass density profile.

The distribution function of the galactic component is derived solving Eddington's formula (1.56) and its profile is plotted in Fig. 3.14.

The initial conditions of the bulge are generated as we did for the halo, implementing the rejection algorithm until when we have $N_{bulge} = 5000$ bodies. To determine their mass we integrate the density profile as in (3.31) and divide the total mass by the number of bodies.

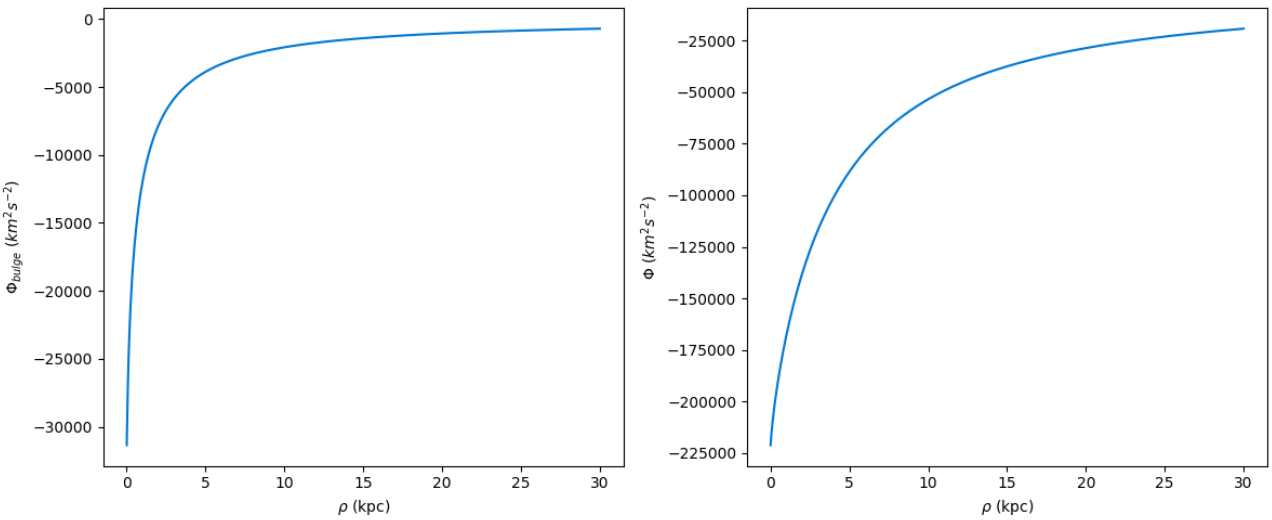

Figure 3.13: Left panel: potential profile of the bulge. Right panel: profile of the total potential (halo, bulge and disk).

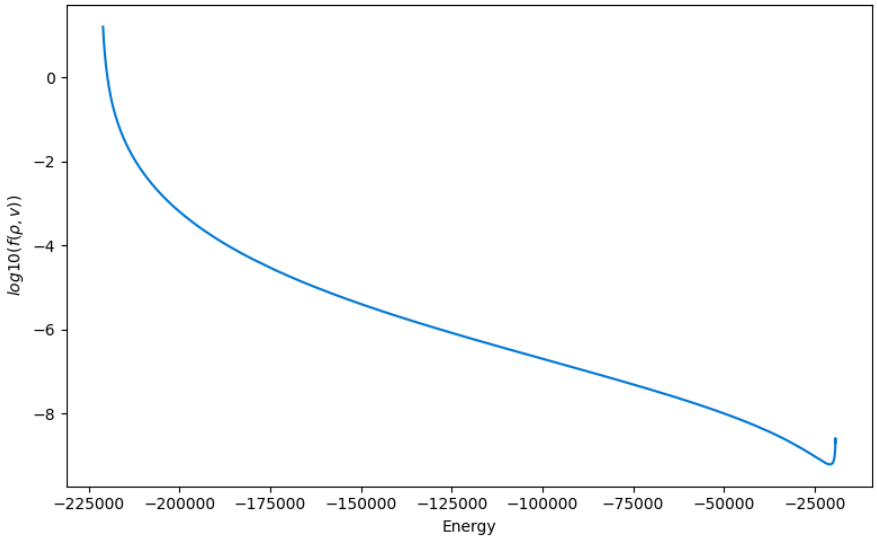

Figure 3.14: Distribution function of the bulge.

3.2.3 Test of the algorithm

To verify if the generated bodies reproduce the imposed densty initial profiles we divide each spherical component in shells of width $\Delta\rho$, for each of them count how many particles are there ($N_{shell\ bodies}$) and then derive the density profile with equation

$$\tilde{\rho}(\rho) = \frac{m_{body} \cdot N_{shell\ bodies}}{4\pi\rho^2\Delta\rho} \tag{3.34}$$

The resulting distributions are illustrated in Fig. 3.15 for the halo and in Fig. 3.16 for the bulge, the outlines are coherent with the imposed laws, hence the adopted method succesfully reproduces the initially imposed functions.

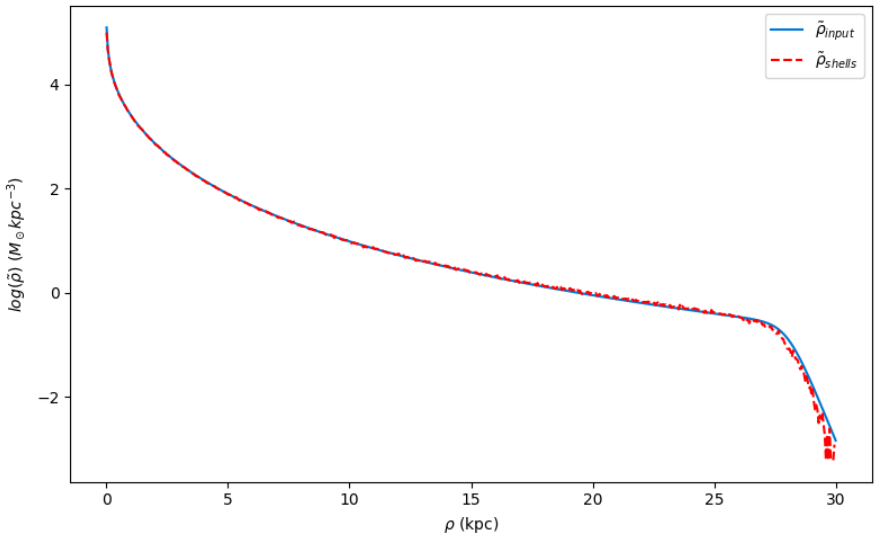

Figure 3.15: Comparison of the input density profile of the halo with the distribution of the initial conditions generated with the rejection algorithm.

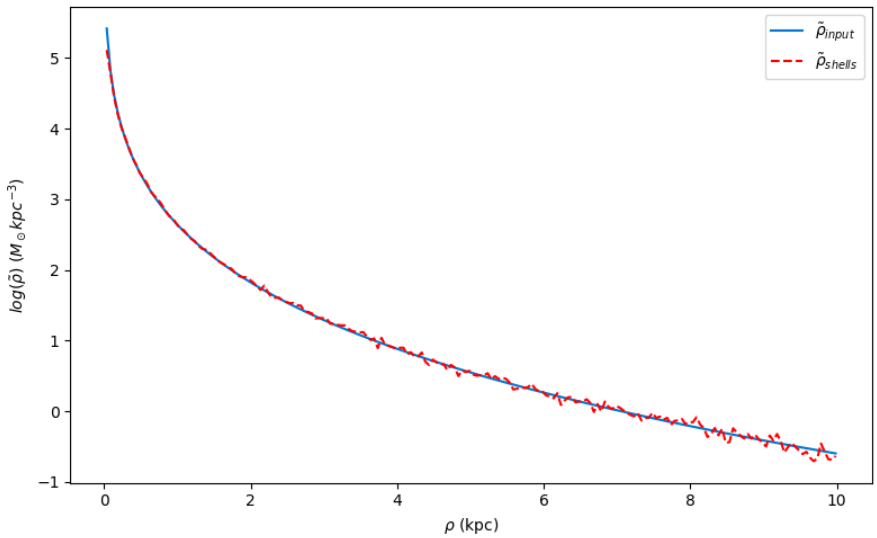

Figure 3.16: Comparison of the input density profile of the bulge with the distribution of the initial conditions generated with the rejection algorithm.

3.3 N-body simulations

The equilibrium of the disk is verified simulating its time evolution with N-body methods. Three main techniques are commonly adopted for studying the behaviour of galactic systems:

- *Tree code techniques*: the system is hierarchically divided into cells. To calculate the force exerted on a body by distant particles, the latter are approximated as a single mass using a multipole expansion of the potential. This approach reduces the computational complexity to $O(N \log N)$, where N is the total number of bodies (Barnes and Hut 1986, Aarseth n.d.).
- *Fast multipole methods*: are similar to tree code techniques, but improve the multipole expansions to increase the accuracy of the force calculations. In favourable conditions, the computational complexity can be reduced further to $O(N)$ (Greengard and Rokhlin 1987, Dehnen 2000).
- *Mesh type methods*: in this approach, the particle distribution is projected onto a spatial grid (either fixed or adaptive), and Poisson's equation is solved numerically, often using the Fast Fourier Transform (FFT), to obtain the potential (Hockney and Eastwood 1988). The computational cost ranges from $O(N)$ to $O(N \log N)$, where N is the number of grid points, depending on the solution scheme adopted.

In this thesis we adopt the N-body simulation used in Kyziropoulos et al. 2016. This algorithm places the galaxy in a box of 70kpc with an adaptive mesh consisting of two grids: one that covers all the box and one in the central region where most of the bodies are concentrated (hence where the system has to be with higher resolution to have accurate computations). This mesh enables us to derive potential of the grid using Poisson's equations and the bodies' acceleration approximating the derivative of the potential using central differences (for more details see Kyziropoulos et al. 2016 and Efthymiopoulos, Gravvanis, and Patsis 2016).
The simulation requires to input the timestep for the integration, we fixed $\Delta t = 10^{-4} Gyr$ because in the inner region bodies orbit very fast, hence to properly study their motion a small timestep is needed. The simulation runs for $0.4 Gyr$, this time interval is sufficient to check equilibrium and self-consistency because particles will orbit for tens or hundreds of times around the galactic centre during this period.
Before running the final simulation and check the disk's self-consistency we relax the different components, first we freeze halo and bulge and let the disk adapt to their presence, this simulation runs only for $0.1 Gyr$ since is only a preliminar step and we do not aim to study the galactic evolution. Once the disk is relaxed we let the system evolve of other $0.1 Gyr$ and then relax the spherical components for $0.1 Gyr$ freexing the disk. Now, once we have recomputed initial conditions of this disk with the potential derived from the relaxed halo and bulge, we finally run the final simulation. To simplify the computations during the relaxation we consider the disk to be completely flat and introduce the thickness only when recomputing the bodies before the final simulation. This is possible since the motion of stars along z can be decoupled from the planar orbits (as mentioned in Section 1.9) and hence it is not relevant in the relaxation.
We report the results of these steps in the following paragraphs.

3.3.1 Relaxation

Relaxing the component is a key step to obtain equilibrium initial conditions for the disk. We adopt this approach becuse the disk component has to adapt itself to the presence of the spherical components and viceversa, this can be done running a simulation where one at a time is frozen.
This process has been developed for previous studies to construct equilibrium N-body models of given mass distribution and given kinematic properties, parameters or constrains (see Rodionov, Athanassoula, and Sotnikova 2009, Rodionov and Athanassoula 2011). The general scheme of this method is presented in Fig. 3.17. It consists in a constrained evolution leading to a galactic model that is in equilibrium and obeys to the imposed conditions. What happens is that the system evolves for a short time interval. Then we modify it so that it has an imposed parameter keeping all the other properties unchanged in order to retain memory of the evolution. This procedure is iterated until all

the conditions have been imposed. The cited studies start from non-equlibrium systems and adopting this technique reach near equilibrium initial conditions of the system thanks to the fact that any non equilibrium system tends to stable equilibrium. In our situation the relaxation is just needed to allow the galactic components to adapt to the gravitational influence of the others.
The time duration of the relaxation should not be too short since the galaxy has to evolve enough, however it can not be too long either because instabilities that change drastically the system should not develop. For our simulations we chose $0.1Gyr$ as timescale for the relaxation, this time period was chosen since it is smaller than the dynamical timesscale used to check the self consistency but in the meanwhile it is enough to relax the perturbations generated by the interaction of the components.

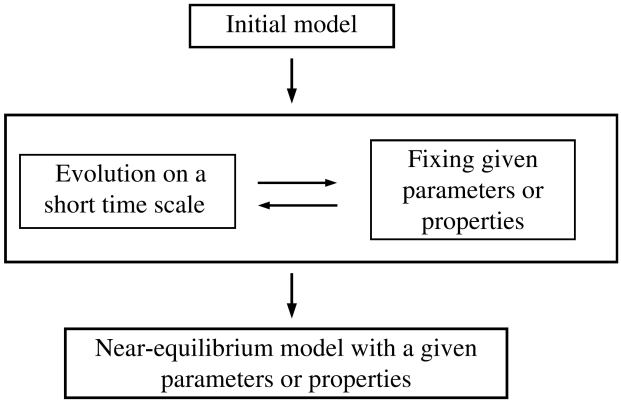

Figure 3.17: Scheme of the relaxation technique (taken from Rodionov and Athanassoula 2011).

Disk relaxation-relaxation 1

First we relax the disk for $0.1Gyr$ freezing halo and bulge, the evolution of the system during this process is showed in Fig. 3.18. Considering the snapshots and the error of the surface density profile (Fig. 3.19) we notice that some pulses are initially generated in the internal region, this is probably related to some noise introduced by the simulation or discrepancies between the potential evaluated on the mesh and the one imposed to derive the distribution function (see Sellwood and Debattista 2009 and Sellwood 2014). These features disappear over the relaxation coherently with the fact that are transient and not related to unstable initial conditions. As for the kinematical profiles illustrated in Fig. 3.20 they do not change significantly during the relaxation.

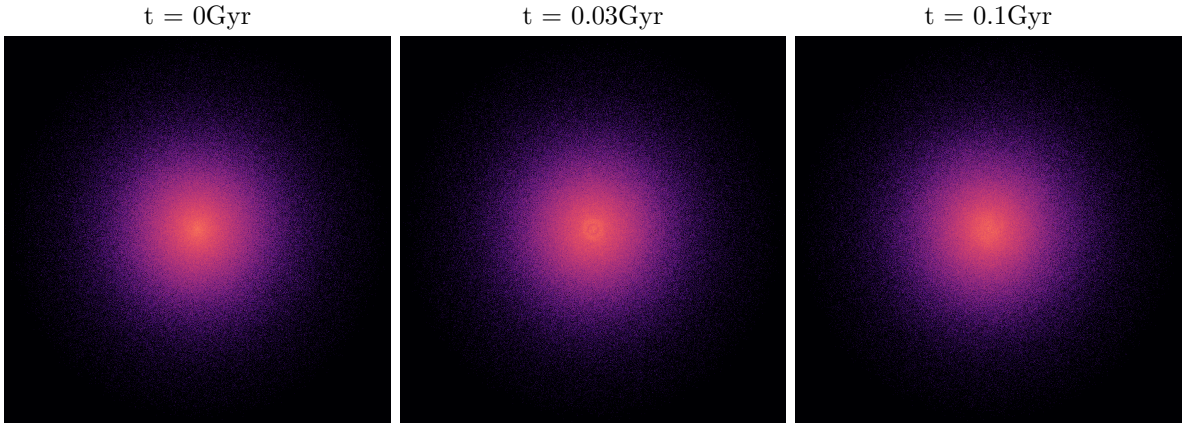

Figure 3.18: Face-on evolution of the disk during relaxation 1.

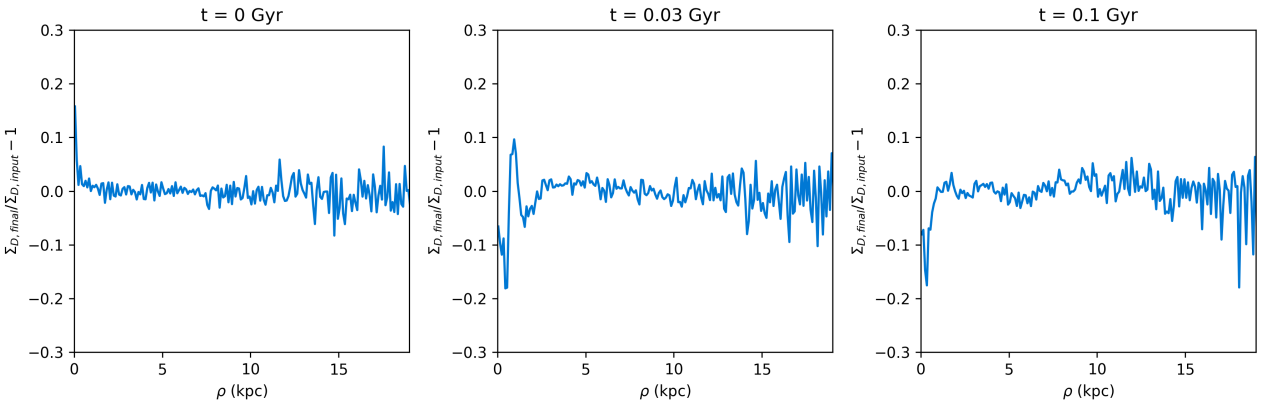

Figure 3.19: Error of the surface density of the disk during relaxation 1

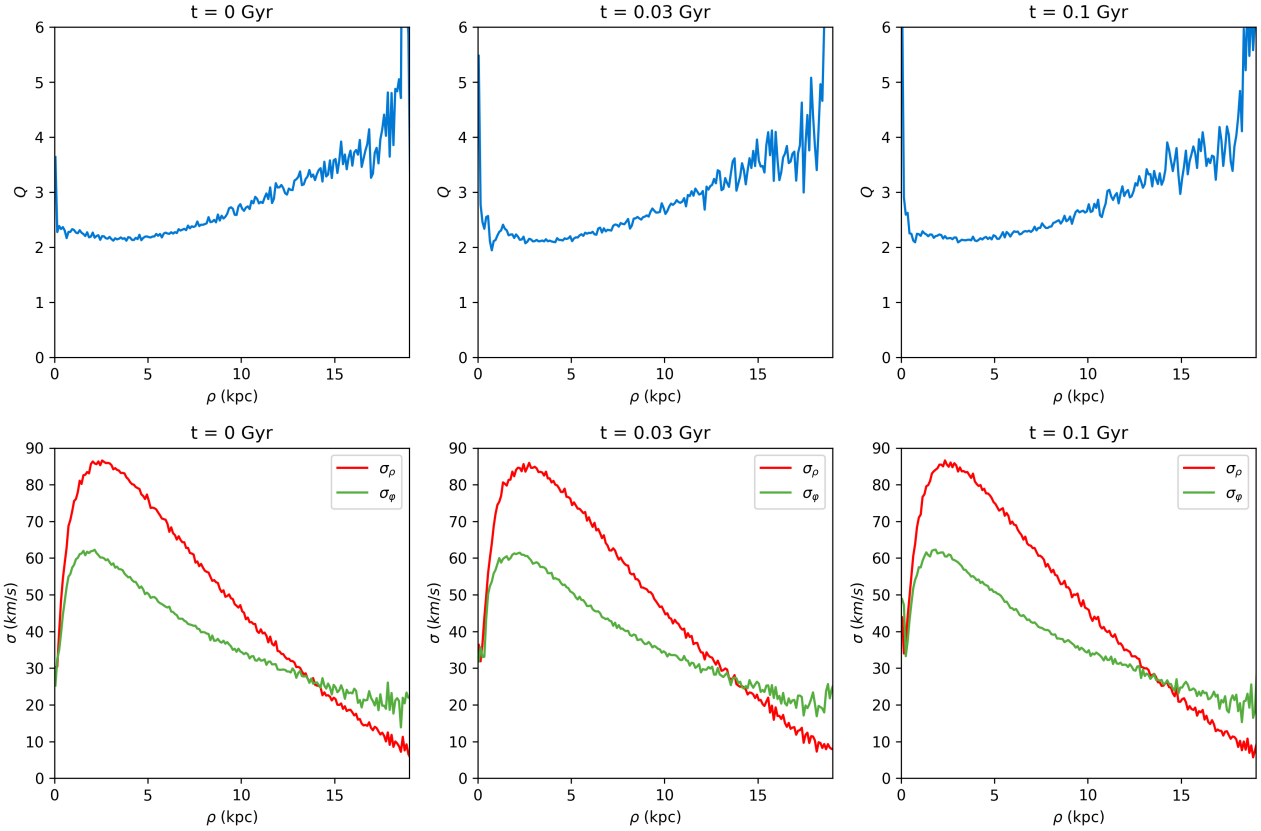

Figure 3.20: Kinematical profiles of the disk during relaxation 1.

Evolution over a short time scale-relaxation 2

After the disk's relaxation we let the system evolve for $0.1Gyr$ without freezing any component as follows from the technique explained in Section 3.3.1. The snapshots obtained from this simulation are illustrated in Fig. 3.21 and the corresponding error of the surface denisty in Fig. 3.22. In this simulation some pulses are still generated at the beginning and even in this case they disappear before the chosen timescale. The profiles of the velocity dispersions and Q presented in Fig. 3.23 reveal that the kinematics of the disk does not change during the phase ofrelaxation.

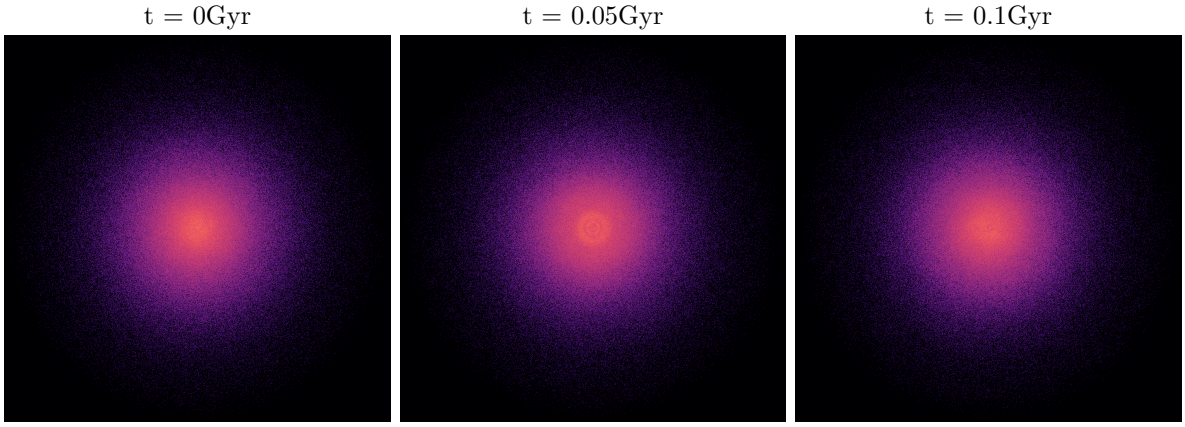

Figure 3.21: Face-on evolution of the disk during relaxation 2

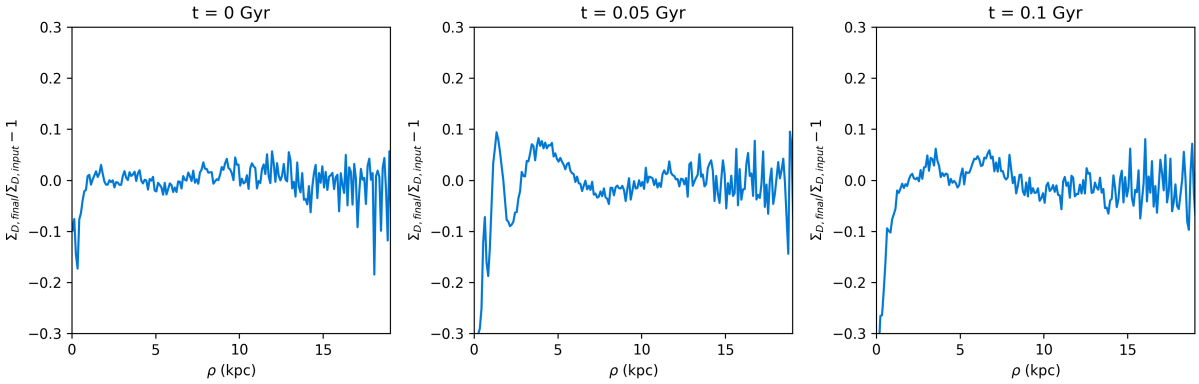

Figure 3.22: Error of the surface density of the disk during relaxation 2.

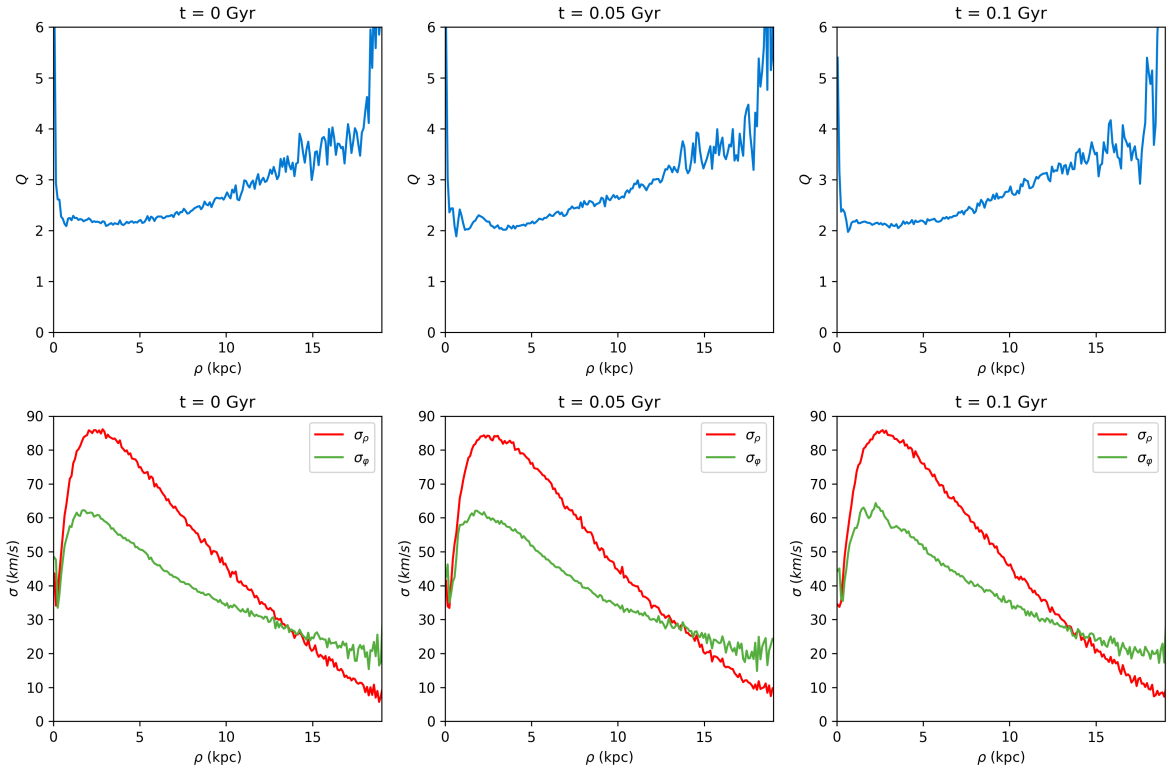

Figure 3.23: Kinematical profiles of the disk during relaxation 2.

Relaxation of the spherical components-relaxation 3

After letting the system evolve with all the components alive we relax the spherical halo and bulge, freezing the disk obtained with relaxation 2 and recomputing the spherical components. The results of this relaxation are presented in Fig. 3.24 for the bulge and 3.26 for the halo. The error of the density profiles at different times of the relaxation are illustrated in Fig. 3.25 and 3.27 respectively. The outlines do not show any significant change, hence this step could be skipped. This is because the spherical components, expecially the halo are not much influenced by the presence of the disk therefore the derivation of the distribution function through Eddington's equation is already enough to have the initial conditions of the spherical components.

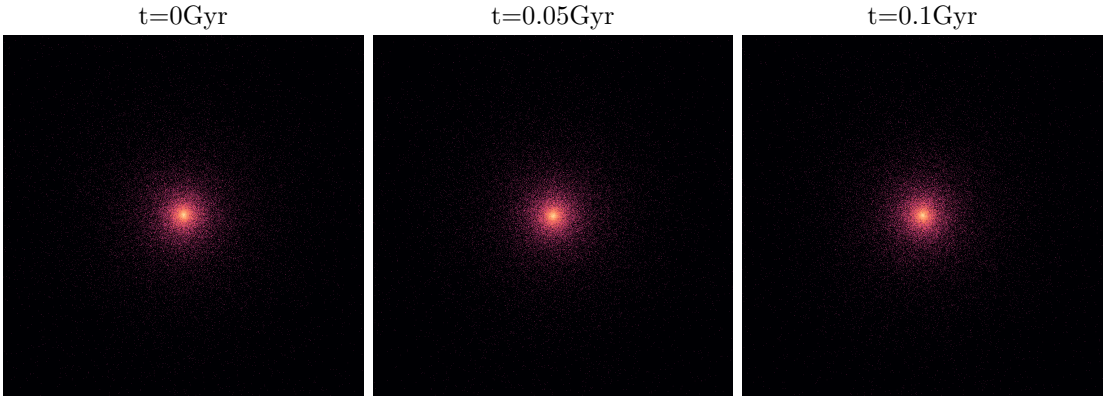

Figure 3.24: Evolution of the bulge during relaxation 3

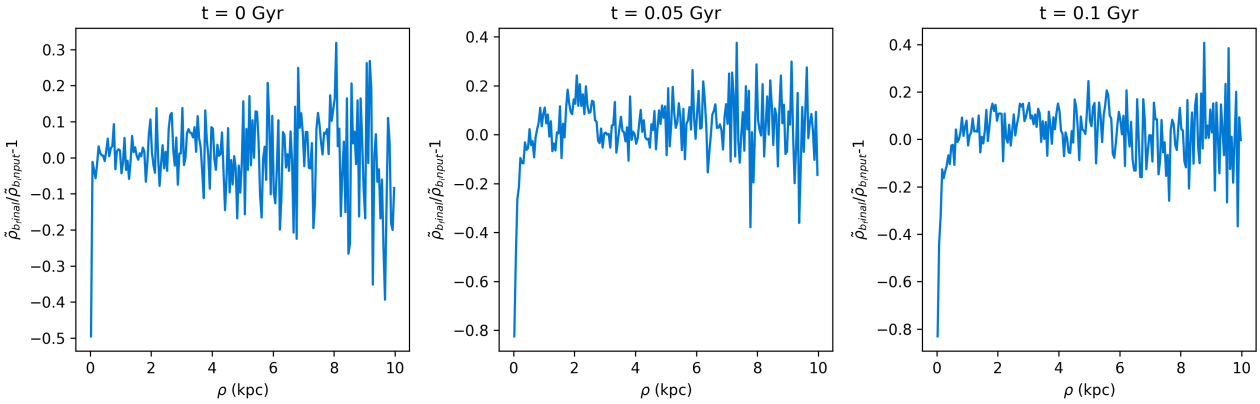

Figure 3.25: Relative error of bulge density during relaxation 3.

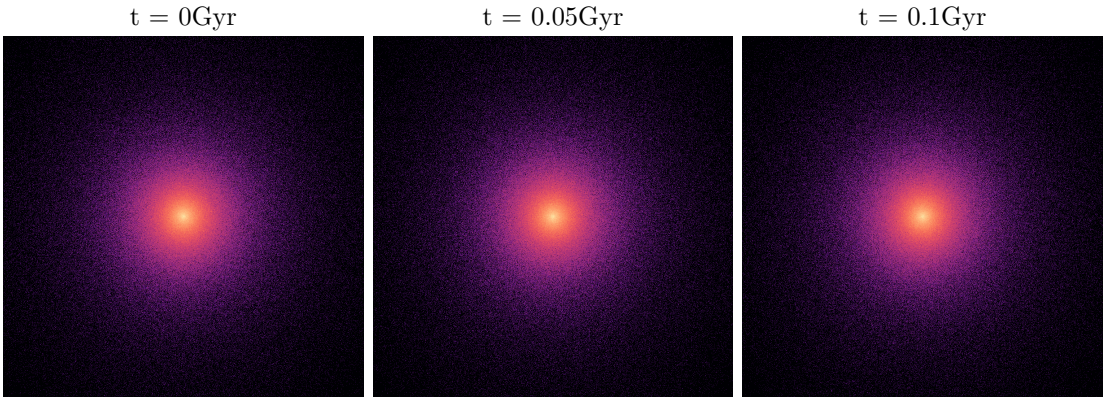

Figure 3.26: Evolution of the halo during relaxation 3

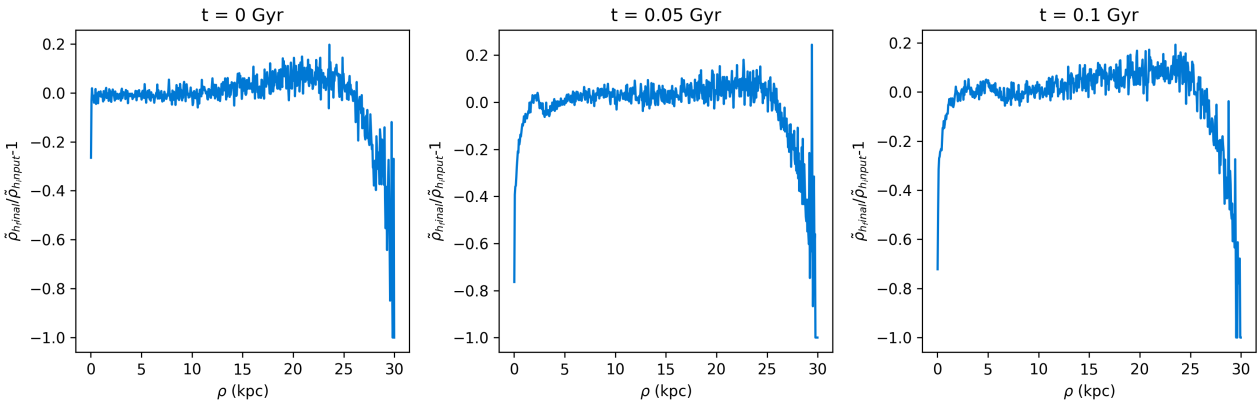

Figure 3.27: Relative error of halo density during relaxation 3.

Recomputation of the disk's DF

Now that the spherical components have been relaxed we recompute the inital conditions of the disk whose self-consistency will be checked with the final simulation. Specifically this new disk is generated starting from the total potential directly given by the code in the last step of simulation 3.
We do not report all the profiles again since most of them do not change significantly. In Fig. 3.28 is illustrated the total profile calculated with this new disk: there is a shift towards higher values in the inner regions, this is due to the corrections occuring during the relaxation. The kinematical profiles are presented in Fig. 3.29 where is clear that these new profiles look like the old ones but with some oscillations probably related to numerical errors. To fix this problem we applied a multidimensional Gaussian filter `scipy.ndimage.gaussian_filter` to the curves. This operation smooths the data by convolving them with a Gaussian kernel, the degree of smoothing is controlled by the parameter sigma, which specifies the standard deviation of the Gaussian function and in our computations is determined manually in order to obtain smooth curves. In Fig. 3.30 we sum the key profile of the computed disk. Recall that at this point we introduce the thickness of the disk implementing the algorithm explained in Section 1.9.

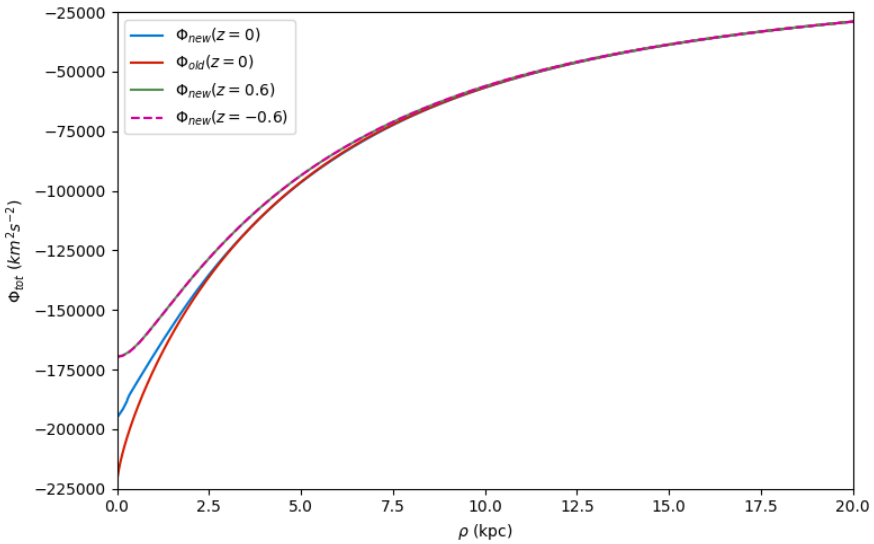

Figure 3.28: Potential profile of the recomputed disk

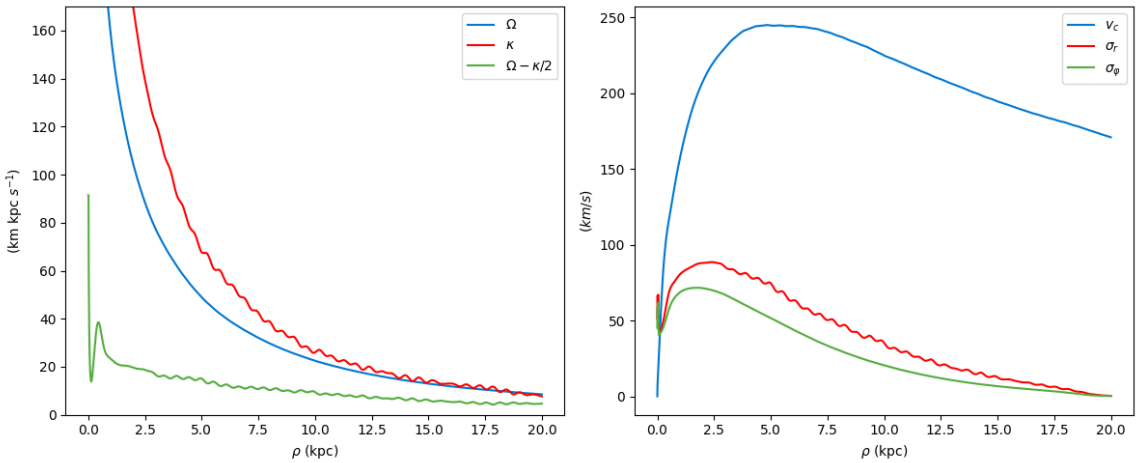

Figure 3.29: Left panel: angular (blue line) and epicyclic (red line) frequencies of the recomputed disk. Right panel: circular velocity (blue line) compared with radial (red line) and angular (green line) dispersions.

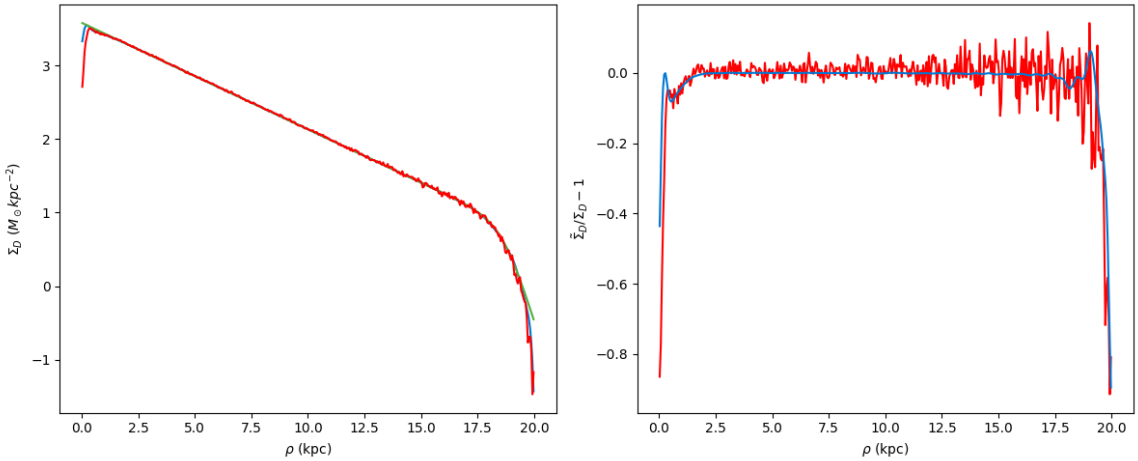

(a) Left panel: surface denisty profile. Right panel: relative error of the computed profile

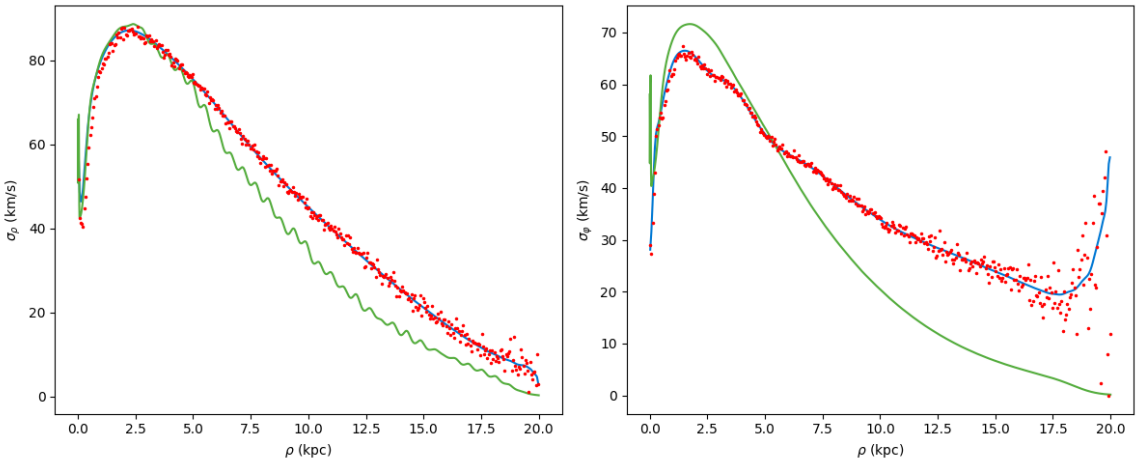

(b) Velocity dispersion profiles in radial (left panel) and angular (right panel) directions.

Figure 3.30: Comparison between the recomputed disk's input profiles (green lines), those derived from distribution function integration (method 2, blue lines), and those computed via binning the disk into equally spaced annuli (method 1, red dots).

3.4 Equilibrium of the disk

Once we have relaxed all the structures, the equilibrium can now be checked running a new simulation with all the components alive. The resulting snapshots are shown in Fig. 3.31 for the face-on disk and in Fig. 3.32 for the edge-on disk. The relative error of the surface density profile of the component is presented in Fig. 3.33 where no significant changes are revealed, therefore the aim of our computations is reached, the galaxy is in equilibrium and self-consistend with the imposed surface density profile. Additional investigations suggest the equilibrium of the disk: the kinematical properties of the system depending on the Toomre profile (3.34) and the velocity dispersion (3.35) are constant over the simulation, hence the system is stable and preserves the constrained input profiles. Also in this simulation we introduce the thickness of the disk. Figure 3.36 shows the distribution function f_z for different cylindrical radii ρ. This analysis was done considering different rings of the disk and counting how many bodies are collocated in different z-bins whose width is 0.07. These plots show an small change in the distribution after $0.1 Gyr$. Then the profile keeps the same trend for all the simulation meaning that it has reached a stable equilibrium. The small initial variation is probably related to the fact that we did not relax the components considering the thikness of the disk.

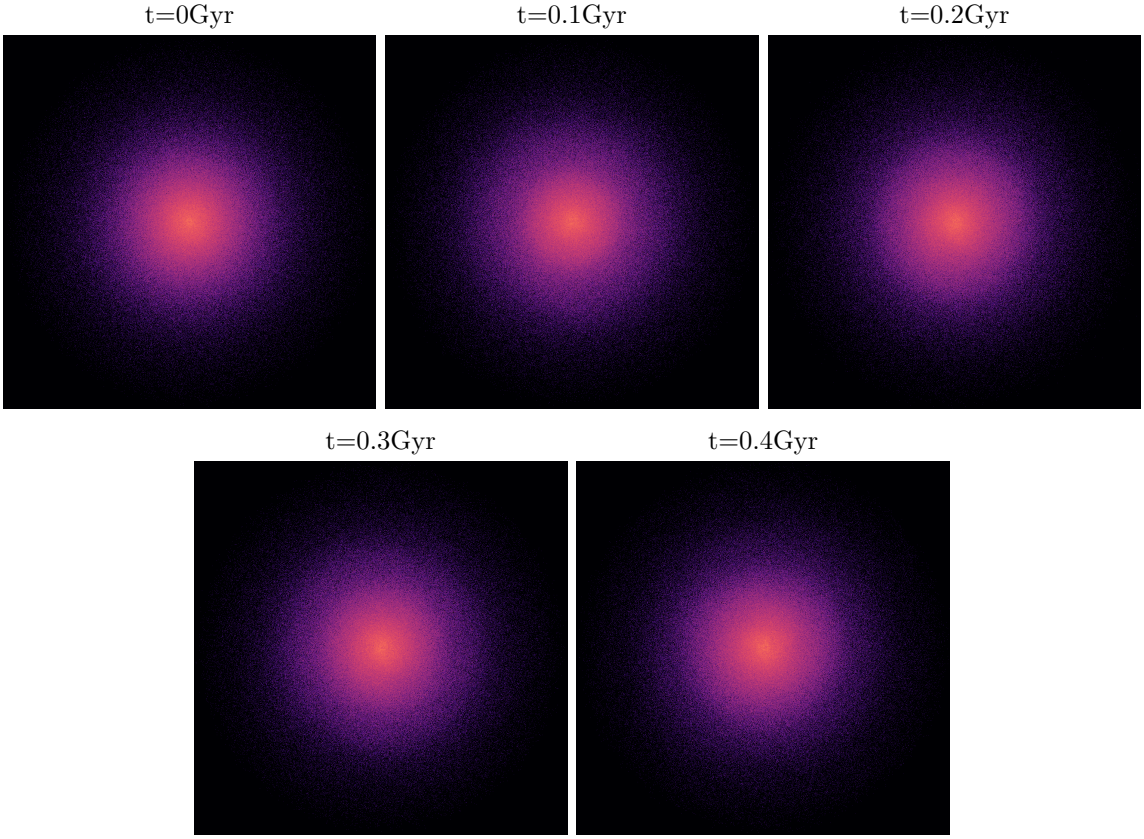

Figure 3.31: Face-on evolution of the disk computed with our model of the DF.

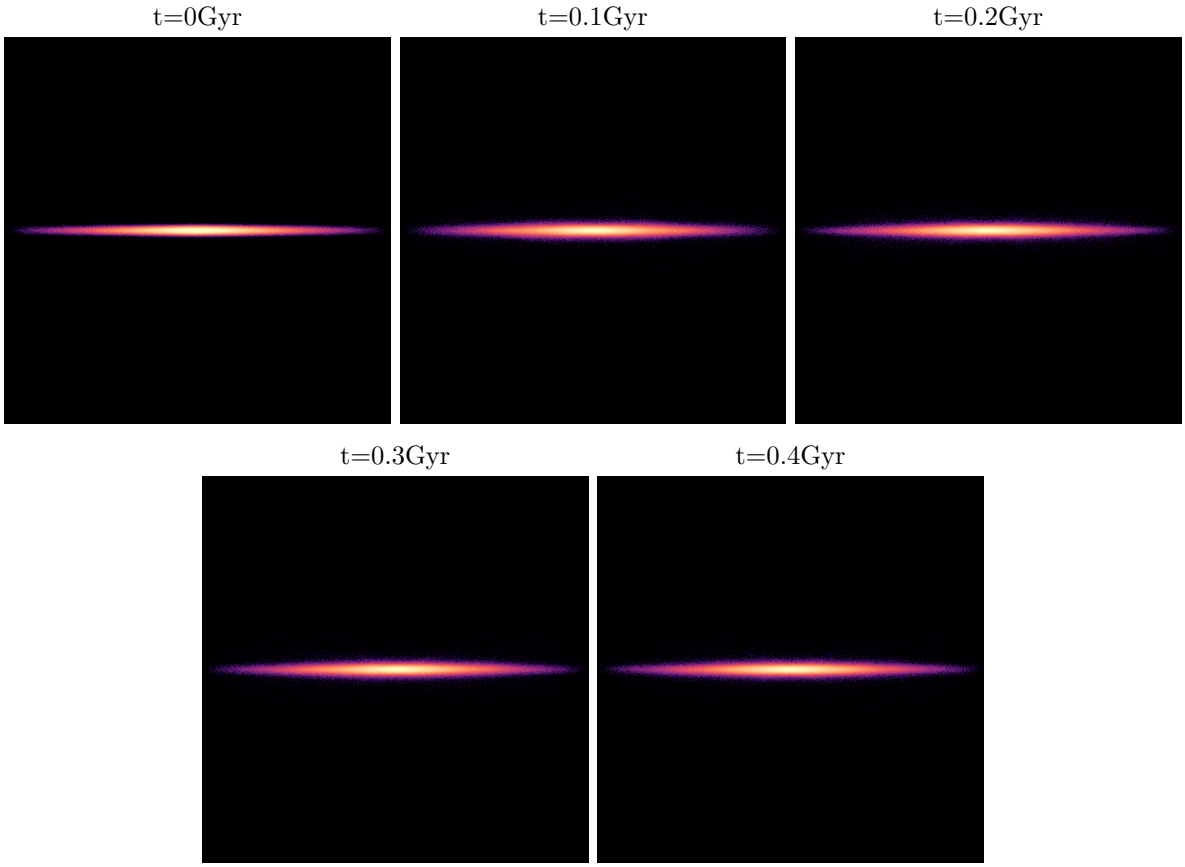

Figure 3.32: Edge-on evolution of the disk computed with our model of the DF.

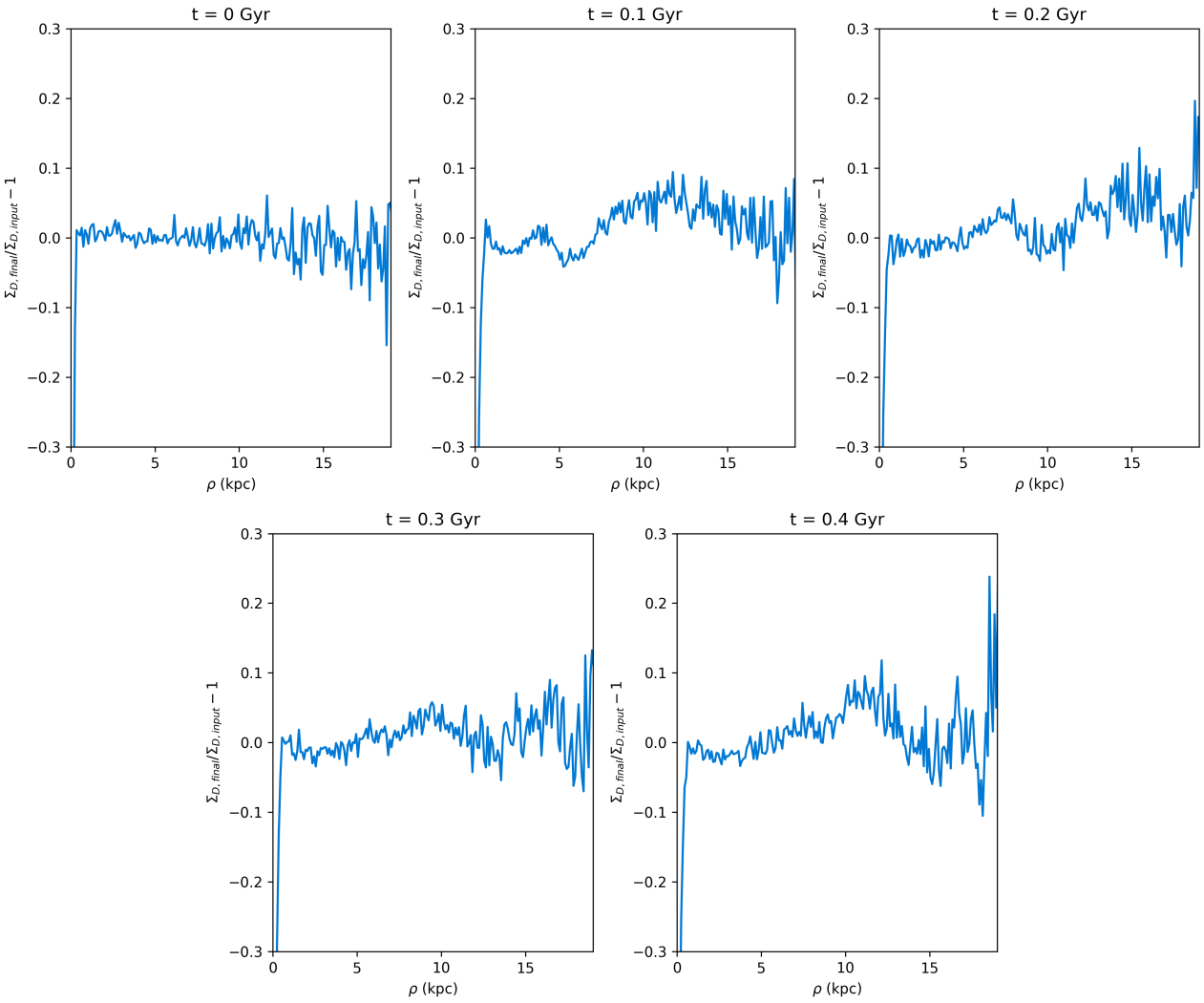

Figure 3.33: Error of the surface denisty of the disk computed with our model of the DF.

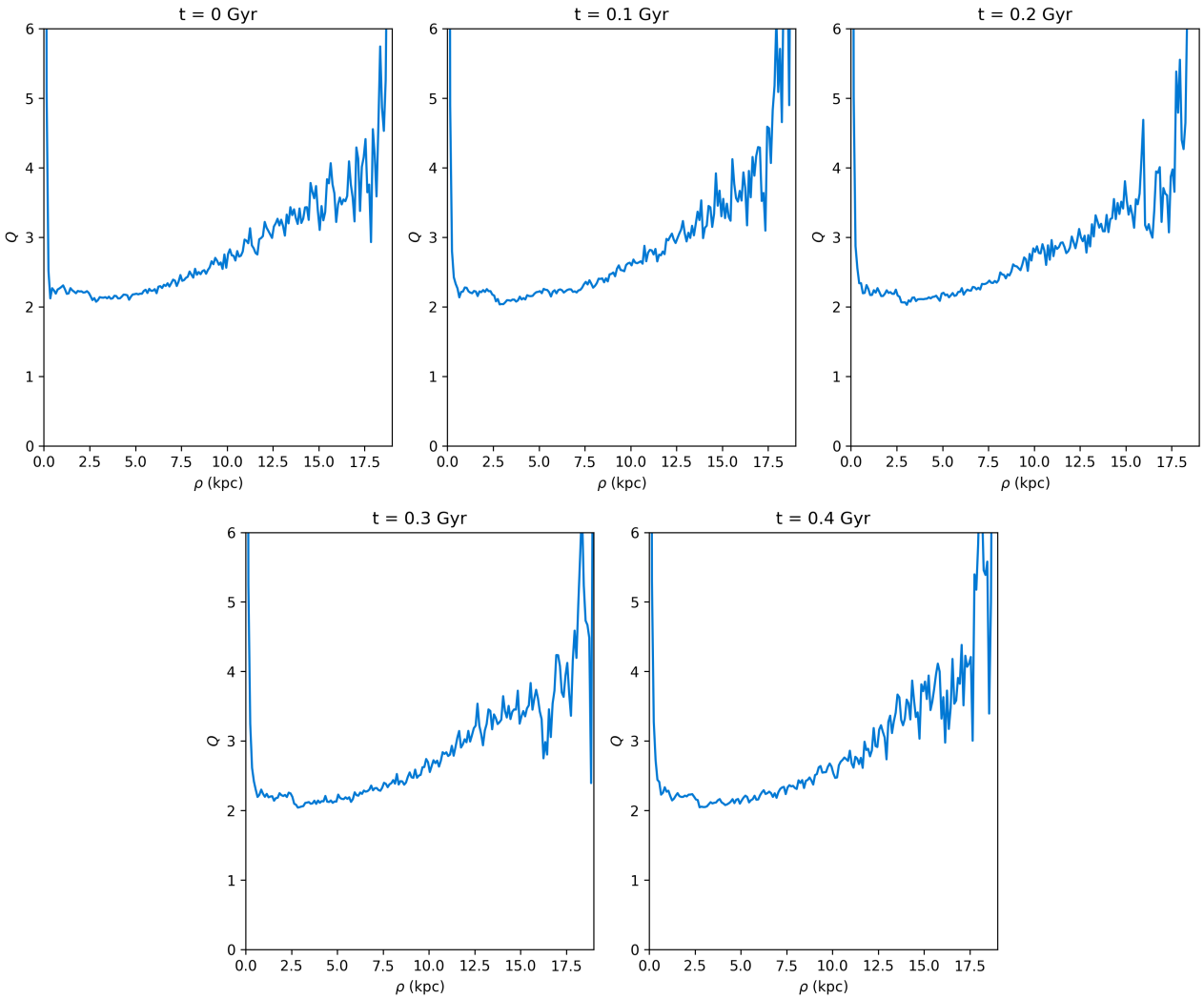

Figure 3.34: Q profile of the disk computed with our model of the DF.

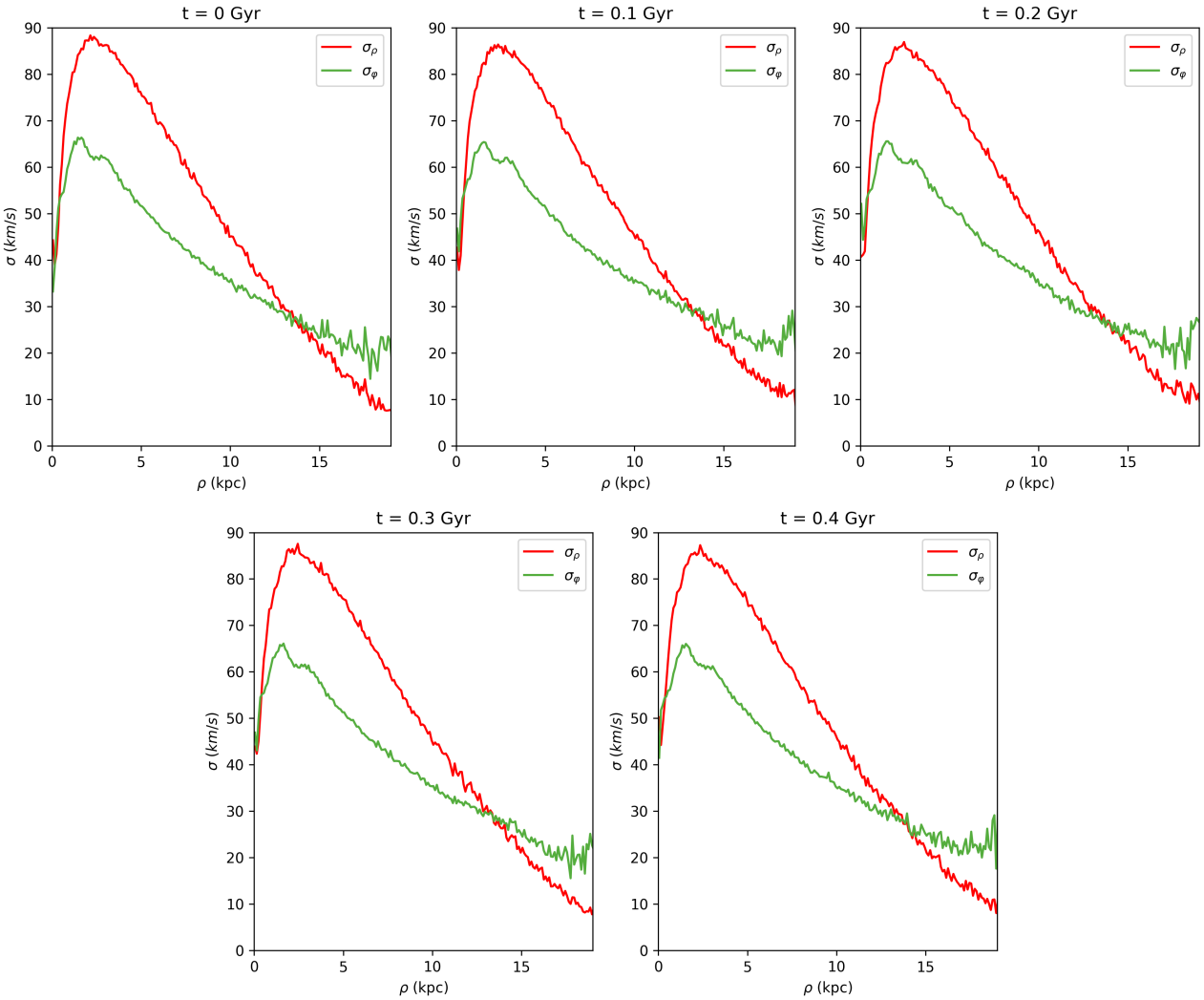

Figure 3.35: Profiles of radial and azimuthal dispersions of the disk computed with our model of the DF.

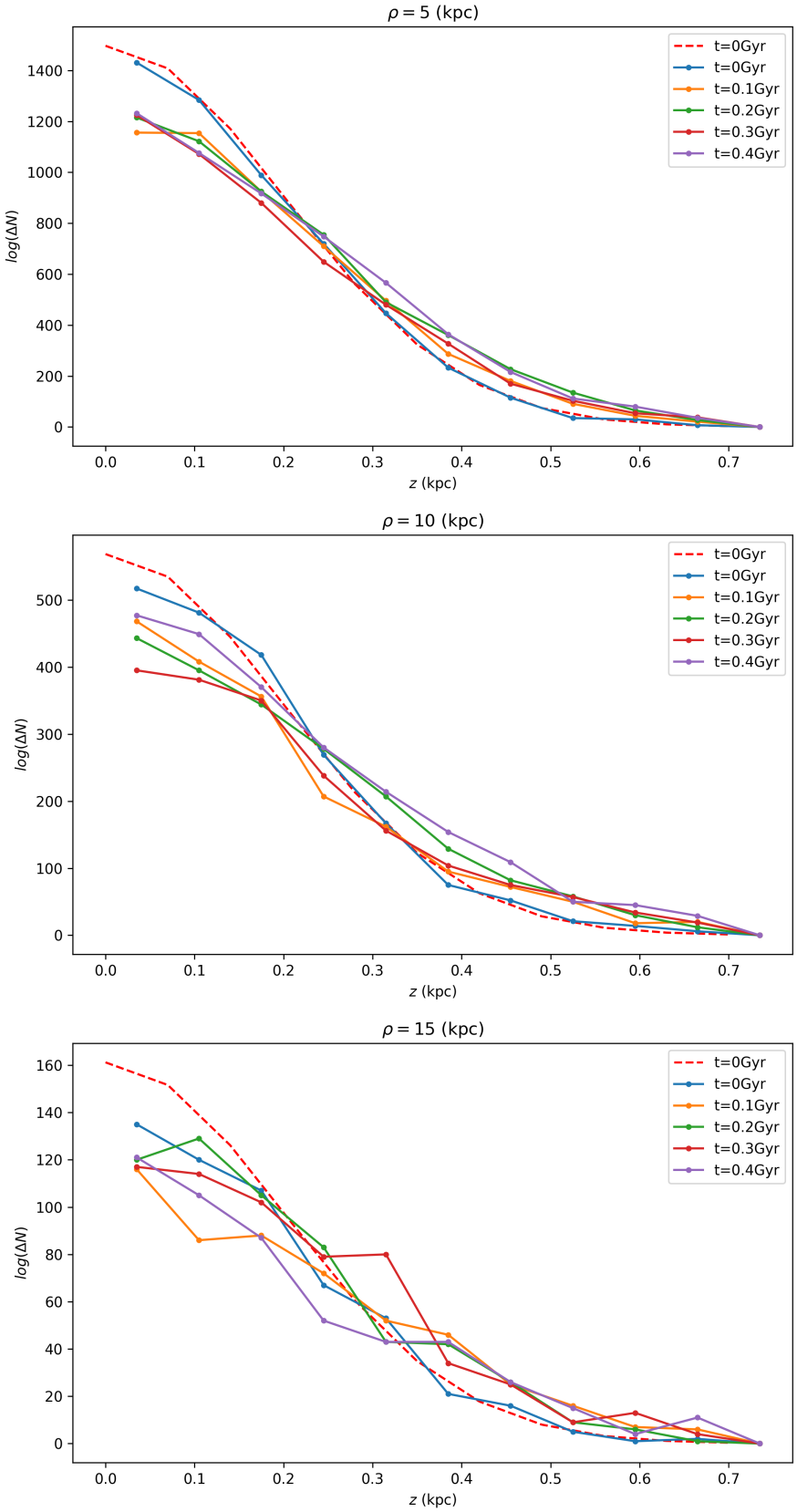

Figure 3.36: Distribution of bodies on the z plane at different radii during the simulation.

3.5 Simulations with other DFs

To highlight the importance of computing the distribution function numerically rather then adopting the knwon models, we implemented the same algorithm with Shu and Hernquist models of the distribution function.

Shu distribution function

Considering Shu distribution function (1.40) the galactic disk evolves as in Fig. 3.37 and the relative error of Σ_D il plotted in Fig. 3.38. These figures reveal that the self-consistency of the system is violated already at the beginning of the simulation, this causes axisymmetric density waves pulses that propagate over the disk. As for the kinematical properties of the disk, presented in Fig. 3.39, we see that the velocity profiles are well reproduced by this DF coherently with the observations made in paragraph (3.5). The change of these profiles suggests the non-exactness of the self-consostency of this system.

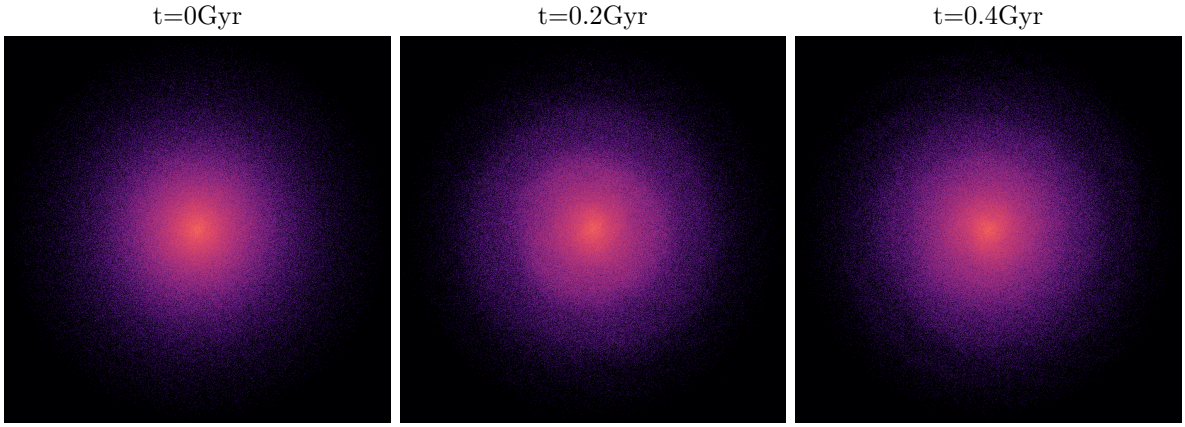

Figure 3.37: Face-on evolution of the disk generated with Shu DF.

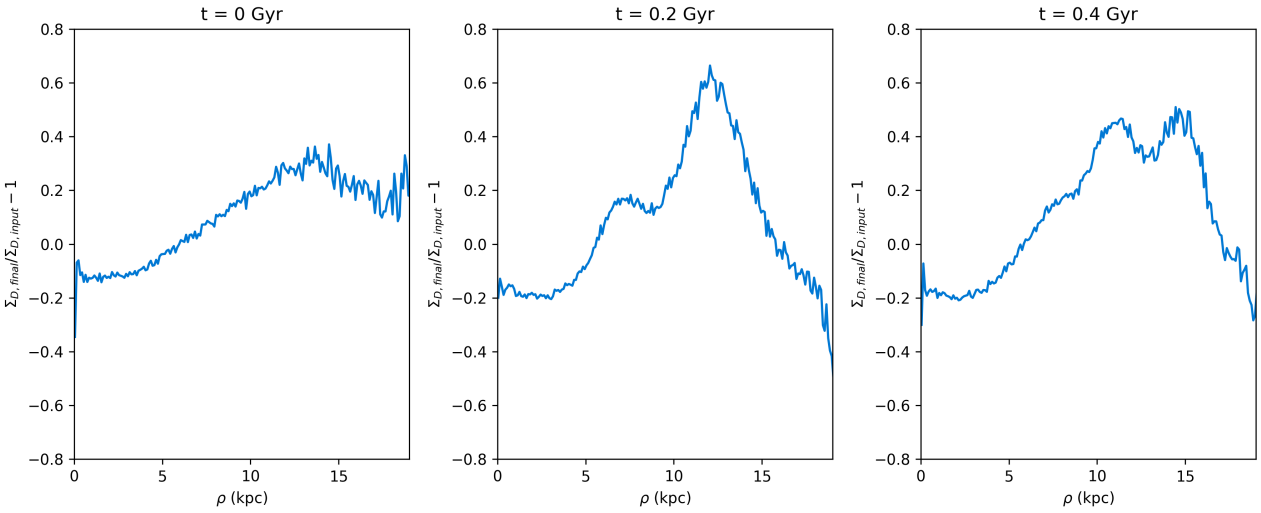

Figure 3.38: Relative error of the surface density when considering the Shu model for the distribution function.

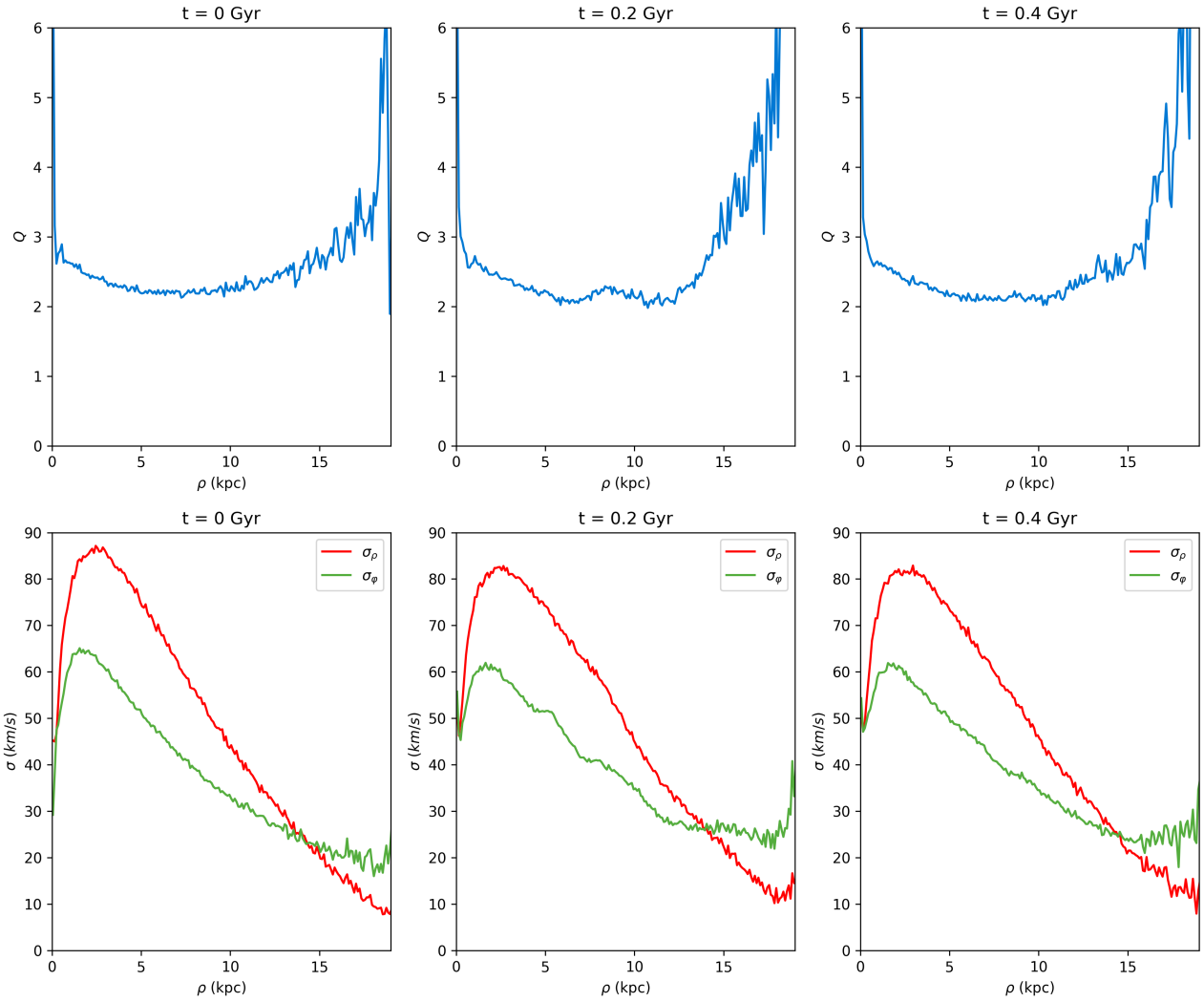

Figure 3.39: Q profile (top panel) and velocity dispersions (bottom panel) of the disk generated with a Shu model distribution function.

Hernquist distribution function

Using the Hernquist model for the distribution function the system is not in equilibrium as revealed by inspecting the various snapshots of Fig. 3.40, and the relative error illustrated in Fig. 3.41. Even in this case axisymmetric density waves pulses develop in the disk. By construction the system is initially self-consistent, but due to its instability this property is not mantained. The amplitude of the pulses tends to decrease over time, hence we expect the disk to reach a asymptotically stable configuration.

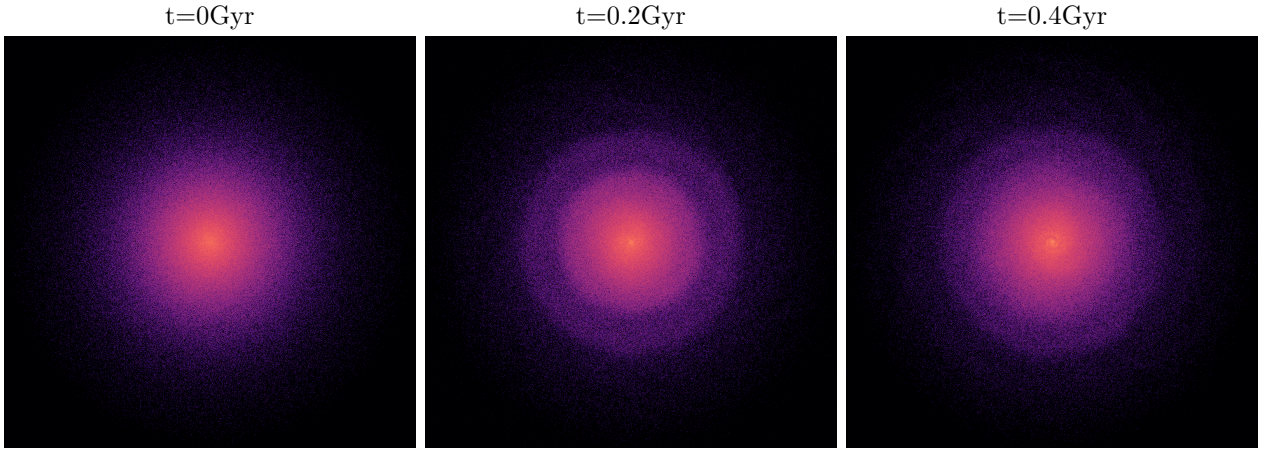

Figure 3.40: Face-on evolution of the disk generated with Hernquist DF.

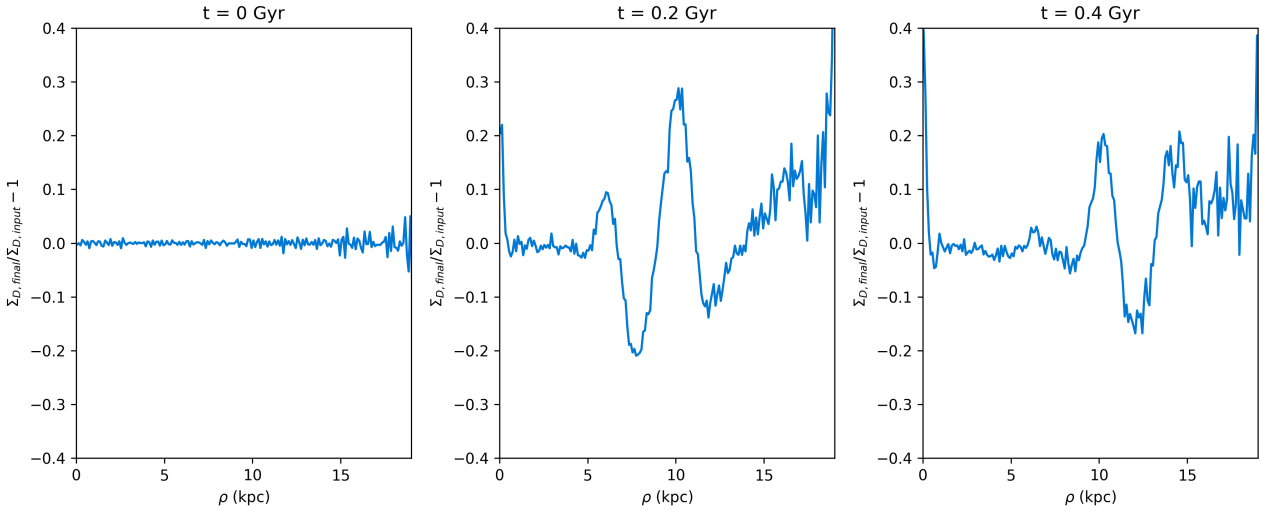

Figure 3.41: Relative error of the surface denisty when considering the Hernquist model for the distribution function.

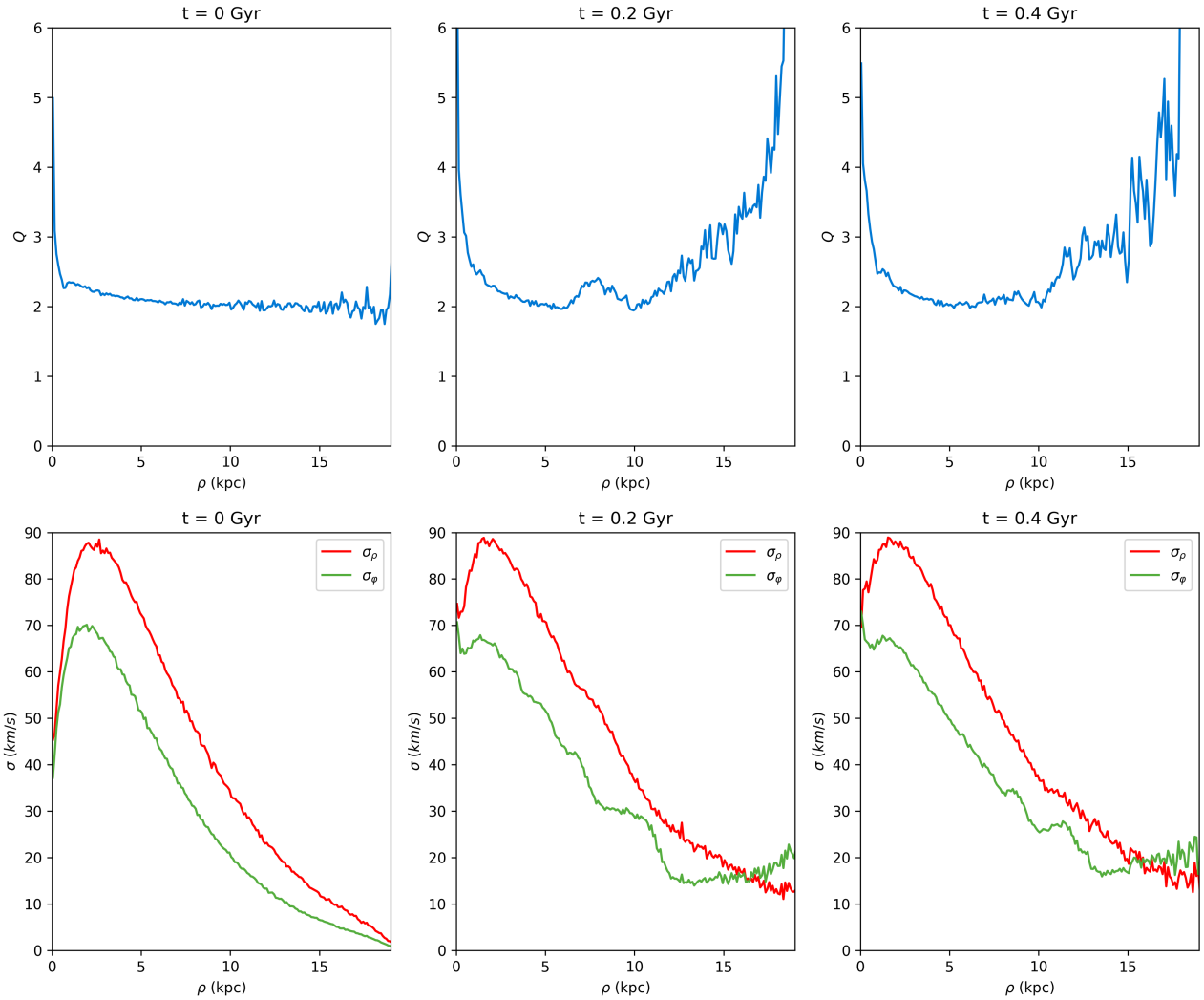

Figure 3.42: Q profile (top panel) and velocity dispersions (bottom panel) of the disk generated with a Hernquist model distribution function.

Chapter 4

Conclusion

4.1 Final discussion

The aim of this thesis was to investigate the evolution of galactic systems with N-body simulations, specifically analyzing the behavior of self-consistent galactic disks embedded in spherical components. To generate the initial conditions of the components, we considered models of the distribution functions that satisfy both the collisionless Boltzmann equation and Poisson's equation; ensuring that density and potential are mutually consistent, we constructed self-consistent galactic components.

Given as input an exponential profile of surface density the simulation conducted in this thesis reveals the self-consistency of the disk. Specifically, the initial profile is exactly reproduced in the initial conditions of the galaxy according to a modified model of the Shu distribution function built to satisfy the self-consistency of the system. This condition is mantained during the whole simulation.

As for the kinematical properties of the disk some discrepancies between the input laws and the profiles generated with the DF are present. These deviations are a consequence of the truncation of the component combined with the requirement of self-consistency for the whole disk. The requirement that no particle exists beyond the chosen maximum radius causes a lack of gravitational support for particles close to the edge of the disk. To compensate for this lack of support and still mantain the self-consistency the internal bodies are forced to increase their gravitational strength with higher velocity dispersion. This mechanism causes a change of the velocity corresponding profiles that increase their values in the outer regions. However the final kinematical profiles keep their trend for all the simulation, hence the equilibrium of the system reamains.

A further aspect of this work concerned the comparison between disk models generated with different distribution functions. Although the initial conditions obtained with different expressions of the DF reveal laws coherent with the inputs some variations in the surface density and velocity dispersion profiles are generated during the simulation. Considering the Shu model of the DF the self-consistency of the model is already violated at the beginning of the simulation and is neither constant over time. Nevertheless the kinematical profiles are well reproduced during the evolution.
When considering the Hernquist profile for the DF although the initial profile exactly reproduces the initial surface density law this property is not maintained during the simulation where pulses are generated in the inner regions. These differences highlight the importance of developing numerical constructions of DFs: analytic approximations, while elegant, may conceal instabilities or hidden inconsistencies that only become apparent in dynamical evolution.

4.2 Further perspectives

This thesis has several limitations, which in turn provide useful indications for potential improvements in future research.
A primary limitation of this work is that the galaxies were modelled under simplified assumptions,

most notably the axisymmetry of the disk or the perfect spherical shape and isotropy of the spherical components. In real scenarios galaxies are more complex, as for the disk axisymmetric features such as spiral arms and bars are typically observed. Spiral structures, in particular, are not transient irregularities but rather dynamical features that can be interpreted within the framework of density wave theory, which explains their persistence as the manifestation of quasi-stationary waves rotating with a characteristic pattern speed around the galactic center. Incorporating such features into future models would not only provide a more realistic representation of galactic systems but also allow the role of spiral patterns in shaping stellar kinematics to be explicitly tested. As for the assumption of spherical shape we could model halos and bugles as flattened or triaxial systems, furthermore isotropy could be introduced. These extensions would allow the models to approximate observed galactic systems more closely and provide a better test of their equilibrium properties.

Another area for improvement concerns the numerical implementation of the simulations. The simulations implemented in this thesis could become more precise considering for example larger particle numbers or longer integration times. Moreover, testing a broader set of input profiles for the components, such as varying scale lengths, central concentrations, or truncation radii would enable a more systematic exploration of parameter space and highlight the sensitivity of self-consistency to initial assumptions.

Using N-body simulations implies neglecting the presence of gases and dissipative processes. Without assuming these two we do not take into account phenomena such as star formation, feedback and transport of angular momentum that are crucial in understanding the dynamics of galactic systems. Hence adoping hydrodynamical simulations we could reach results more compatible to what is observed in real galaxies. In this context we could even model the emission spectrum of the galaxy considering star formation and spectral synthesis. This enables to directly compare emission spectra of observations with our model.

The comparison between models and observations represents a powerful tool that can be extensively employed in future investigations. Constructig galactic models with different input parameters we can compare the resultig spectra with the observed one and constrain some properties of the galaxy. This idea could be applied, for example, for the determination of pattern speed (Ω_P) of spiral arms. Considering a spiral galaxy we could give an estimate of the pattern speed of its arms looking for a model that matches its velocity field.

Moreover we could study the interactions and mergers of different galaxies. Encounters between two galactic systems, direct collisions or close passages, offer an opportunity to investigate tidal features and the redistribution of angular momentum.

Bibliography

Aarseth, S.J. (n.d.). *Gravitational N-Body Simulations: Tools and Algorithms*. Cambridge Monographs on Mathematical Physics.

Barnes, Josh and Piet Hut (Dec. 1986). "A hierarchical O(N log N) force-calculation algorithm". In: *Nature* 324.6096, pp. 446–449.

Bienayme, O. and N. Sechaud (July 1997). "Stellar kinematics in the solar neighbourhood and the disc scale lengths of the Galaxy." In: *Astronomy & Astrophysics* 323, pp. 781–788.

Binney, James and Scott Tremaine (2008). *Galactic Dynamics: Second Edition*.

Bovy, Jo (2026). *Dynamics and Astrophysics of Galaxies*. Princeton, NJ: Princeton University Press. in press.

Contopoulos, George (1960). "A third integral of motion in a galaxy". In: *Zeitschrift für Astrophysik* 49, pp. 273–291.

Dehnen (Nov. 1993). "A Family of Potential-Density Pairs for Spherical Galaxies and Bulges". In: *Monthly Notices of the Royal Astronomical Society* 265, p. 250.

— (1999). "Simple Distribution Functions for Stellar Disks". In: *The Astronomical Journal* 118.3, pp. 1201–1215.

— (June 2000). "A Very Fast and Momentum-conserving Tree Code". In: *The Astrophysical Journal Letters* 536.1, pp. L39–L42.

Efthymiopoulos, C., George Gravvanis, and P. Patsis (Nov. 2016). "Structures induced by companions in galactic discs". In: *Monthly Notices of the Royal Astronomical Society*.

Golub, G.H., Per Christian Hansen, and Dianne O'leary (Jan. 2000). "Tikhonov regularization and total least squares". In: *SIAM J. Matrix Anal. Appl.* 2, pp. 413–429.

Graham, Alister W. and Simon P. Driver (Jan. 2005). "A Concise Reference to (Projected) Sérsic $R^{1/n}$ Quantities, Including Concentration, Profile Slopes, Petrosian Indices, and Kron Magnitudes". In: *Publications of the Astronomical Society of Australia* 22.2, pp. 118–127.

Greengard, L. and V. Rokhlin (Dec. 1987). "A Fast Algorithm for Particle Simulations". In: *Journal of Computational Physics* 73.2, pp. 325–348.

Hänninen, J. and Chris Flynn (July 2004). "Numerical simulations of radial heating in the Galaxy". In: *Astronomy & Astrophysics* 421, pp. 1001–1010.

Hernquist, Lars (June 1990). "An Analytical Model for Spherical Galaxies and Bulges". In: *The Astrophysical Journal* 356, p. 359.

Hockney, R. W. and J. W. Eastwood (1988). *Computer simulation using particles*.

Kuijken, K. and M. R. Merrifield (Oct. 1993). "A new method for obtaining stellar velocity distribution from absorption-line spectra : unresolved Gaussian decomposition." In: *Monthly Notices of the Royal Astronomical Society* 264, pp. 712–720.

Kyziropoulos, P. E. et al. (Dec. 2016). "Structures induced by companions in galactic discs". In: *Monthly Notices of the Royal Astronomical Society* 463.2, pp. 2210–2228.

Pichon, C. and D. Lynden-Bell (Oct. 1996). "Equilibria of flat and round galactic discs". In: *Monthly Notices of the Royal Astronomical Society* 282.4, pp. 1143–1158.

Pichon, C. and E. Thiebaut (Dec. 1998). "Non-parametric reconstruction of distribution functions from observed galactic discs". In: *Monthly Notices of the Royal Astronomical Society* 301.2, pp. 419–434.

Rodionov, S. A. and E. Athanassoula (May 2011). "Extensions and applications of the iterative method". In: *Astronomy & Astrophysics* 529, A98, A98.

Rodionov, S. A., E. Athanassoula, and N. Ya. Sotnikova (Jan. 2009). "An iterative method for constructing equilibrium phase models of stellar systems". In: *Monthly Notices of the Royal Astronomical Society* 392.2, pp. 904–916.

Saad, Youcef and Martin H. Schultz (1986). "GMRES: A Generalized Minimal Residual Algorithm for Solving Nonsymmetric Linear Systems". In: *SIAM Journal on Scientific and Statistical Computing* 7.3, pp. 856–869.

Sellwood, J. A. (Jan. 2014). "Secular evolution in disk galaxies". In: *Rev. Mod. Phys.* 86 (1), pp. 1–46.

Sellwood, J. A. and Victor P. Debattista (Sept. 2009). "Stochasticity in N-body simulations of disc galaxies". In: *Monthly Notices of the Royal Astronomical Society* 398.3, pp. 1279–1297.

Sharma, Sanjib and Joss Bland-Hawthorn (Aug. 2013). "An empirical formula for the distribution function of a thin exponential disc". In: *The Astrophysical Journal* 773.2, p. 183.

Shu, Frank H. (Nov. 1969). "Models of Partially Relaxed Stellar Disks". In: *The Astrophysical Journal* 158, p. 505.

Toomre, A. (May 1964). "On the gravitational stability of a disk of stars." In: *The Astrophysical Journal* 139, pp. 1217–1238.